The VLA Nascent Disk and Multiplicity Survey of Perseus Protostars (VANDAM). II. Multiplicity of Protostars in the Perseus Molecular Cloud

John J. Tobin[1,10], Leslie W. Looney[2], Zhi-Yun Li[3], Claire J. Chandler[4], Michael M. Dunham[5], Dominique Segura-Cox[2], Sarah I. Sadavoy[6], Carl Melis[7], Robert J. Harris[1], Kaitlin Kratter[8], Laura Perez[4]

ABSTRACT

We present a multiplicity study of all known protostars (94) in the Perseus molecular cloud from a Karl G. Jansky Very Large Array (VLA) survey at Ka-band (8 mm and 1 cm) and C-band (4 cm and 6.6 cm). The observed sample has a bolometric luminosity range between 0.1 $L_\odot$ and $\sim$33 $L_\odot$, with a median of 0.7 $L_\odot$. This multiplicity study is based on the Ka-band data, having a best resolution of $\sim 0\farcs065$ (15 AU) and separations out to $\sim 43''$ (10000 AU) can be probed. The overall multiplicity fraction (MF) is found to be of 0.40$\pm$0.06 and the companion star fraction (CSF) is 0.71$\pm$0.06. The MF and CSF of the Class 0 protostars are 0.57$\pm$0.09 and 1.2$\pm$0.2, and the MF and CSF of Class I protostars are both 0.23$\pm$0.08. The distribution of companion separations appears bimodal, with a peak at $\sim$75 AU and another peak at $\sim$3000 AU. Turbulent fragmentation is likely the dominant mechanism on >1000 AU scales and disk fragmentation is likely to be the dominant mechanism on <200 AU scales. Toward three Class 0 sources we find companions separated by <30 AU. These systems have the smallest separations of currently known Class 0 protostellar binary systems. Moreover, these close systems are embedded within larger (50 AU to 400 AU) structures and may be candidates for ongoing disk fragmentation.

Subject headings: planetary systems: proto-planetary disks — stars: formation

[1]Leiden Observatory, Leiden University, P.O. Box 9513, 2300-RA Leiden, The Netherlands; tobin@strw.leidenuniv.nl

[2]Department of Astronomy, University of Illinois, Urbana, IL 61801

[3]Department of Astronomy, University of Virginia, Charlottesville, VA 22903

[4]National Radio Astronomy Observatory, P.O. Box O, Socorro, NM 87801

[5]Harvard-Smithsonian Center for Astrophysics, 60 Garden St, MS 78, Cambridge, MA 02138

[6]Max-Planck-Institut für Astronomie, D-69117 Heidelberg, Germany

[7]Center for Astrophysics and Space Sciences, University of California, San Diego, CA 92093

[8]University of Arizona, Steward Observatory, Tucson, AZ 85721

[10]Veni Fellow

1. Introduction

A significant fraction of stars are found in multiple systems. The frequency of multiplicity is a strong function of spectral type (or stellar mass): most O and B stars are multiples (e.g., Sana & Evans 2011), as are about half of all solar-type (G) stars (Raghavan et al. 2010), around one third of M stars (Lada 2006), and 20 - 25% of brown dwarfs or very low mass stars (Allen et al. 2007), also see the review by Duchêne & Kraus (2013). Thus, multiple stellar systems are a common outcome of the star formation process and our physical understanding of star formation must account for the formation of multiple systems (e.g., Mathieu 1994; Tohline 2002; Reipurth et al. 2014).

Multiple systems are expected to form early in the star formation process when there is a large mass reservoir available. Multiple systems may form through several possible processes (and combinations thereof): 1) turbulent fragmentation of the molecular cloud (e.g., Padoan & Nordlund 2002; Offner et al. 2010; Bate 2012), 2) the thermal fragmentation of strongly perturbed, rotating, and infalling core (e.g., Inutsuka & Miyama 1992; Burkert & Bodenheimer 1993; Boss & Keiser 2013, 2014), and/or 3) the fragmentation of a gravitationally unstable circumstellar disk (e.g., Adams et al. 1989; Bonnell & Bate 1994a,b; Machida et al. 2008; Stamatellos & Whitworth 2009). Fragmentation due to scenarios 1) and 2) will lead to multiple systems that are initially separated by several hundred to 1000s of AU; direct observational evidence for this process taking place may have been observed in Pineda et al. (2015). On the other hand, scenario 3) will form companions with initial separations of 100s of AU or less and there are several examples for which this process may have taken place (e.g., Rodríguez et al. 1998; Takakuwa et al. 2012; Tobin et al. 2013). Furthermore, dynamical interactions in an initially close triple system (presumably formed by one of the route mentioned above) can eject one member into a wide orbit, providing an alternate mechanism for the production of wide systems (Reipurth et al. 2010; Reipurth & Mikkola 2012).

The distribution of companion separations in multiple systems can reflect their likely formation mechanism. The characteristic separation for solar-type multiples is 45 AU (Raghavan et al. 2010), but 5.3 AU for low-mass (0.5 $M_{\odot}$ to 0.1 $M_{\odot}$) stars (Fischer & Marcy 1992). However, the main-sequence field multiple systems have been shaped by dynamical evolution (Marks & Kroupa 2012, e.g., three-body interactions, interactions with cluster members). Therefore the present distribution of separations in field multiples is likely substantially different from their initial separation distribution. This makes it difficult to infer the likely formation routes of multiple systems from the observations of field stars alone, and to gain a better understanding of multiple star formation, characterizing the multiplicity properties of young, forming stars is crucial.

Young stars are typically divided into four observational classes, Class 0, I, II, and III (e.g., Dunham et al. 2014). Class 0 protostars are considered the youngest and most deeply embedded within dense envelopes of gas and dust (André et al. 1993), Class I protostars are still surrounded by envelopes but are less embedded than Class 0s, Class II sources have no (or very tenuous) envelopes and are comprised of a dusty disk around a pre-main sequence star, and Class III sources are pre-main sequence stars without substantial disk emission, but may have debris disks. Note that the

Class 0 definition is not independent of Class I because Class 0 is based on submillimeter luminosity and the Class I, II, and III definitions are based on the near to mid-infrared spectral slope (Lada 1987). Alternatively, bolometric temperature (T_{bol}) is also used and has boundaries defined for all Classes (Myers & Ladd 1993); however, the observational classification may not necessarily reflect the true evolutionary state of the YSO due to extinction and inclination effects (Launhardt et al. 2013; Dunham et al. 2014). The expected lifetime in the Class 0 phase is expected to be ∼160 kyr and the combined Class 0 and Class I phase is expected to last ∼ 500 kyr (Dunham et al. 2014), assuming a 2 Myr lifetime of the Class II phase.

Multiplicity is becoming well-characterized for pre-main sequence stars (Class II and III sources) with radial velocity and high-contrast imaging techniques (e.g., Kraus et al. 2011, 2008; Reipurth et al. 2007; Kraus & Hillenbrand 2012). The typical statistics derived from multiplicity studies are the multiplicity fraction (MF) and companion star fraction (CSF). These measures can be thought of as the probability of a given system having companions and the average number of companions per system, respectively. The MF is defined by

$$MF = \frac{B + T + Q + ...}{S + B + T + Q + ...} \tag{1}$$

and the CSF is defined by

$$CSF = \frac{B + 2T + 3Q + ...}{S + B + T + Q + ...} \tag{2}$$

where S, B, T, and Q stand for the number of single, binary, triple, and quadruple systems respectively. The overall CSF of Class II and Class III objects in Taurus is ∼0.7 (Kraus et al. 2011) with the fractions of single systems only being about 0.25 to 0.33. In contrast to the more distributed population in Taurus, the Orion Nebula Cluster only has a CSF of ∼0.08 between 67.5 AU to 675 AU, about 2.5× lower than Taurus for the same range of separations (Reipurth et al. 2007). This reduction in companions is thought to result from dynamical interactions in the dense cluster environment that strip wider companions.

The multiplicity of Class I protostars, on the other hand, has not been as well-characterized due to their embedded nature. Connelley et al. (2008) conducted a near-infrared survey of Class I sources in several star forming regions, finding companions toward 27 of 136 targets with separations between 200 AU and 2000 AU. At separations between 50 AU and 200 AU, Connelley et al. (2009) and Duchêne et al. (2007) found 15 companions out of 88 targets. Thus, Class I protostars have CSF of ∼0.36 from between 50 and 2000 AU and the distribution of separations is rather flat between 100 AU and 2000 AU, with an increase at ∼3000 AU (Connelley et al. 2008). Thus, multiplicity is commonly observed toward Class I and II sources, but the distribution of separations does not appear universal for all star forming regions.

The Class 0 sources remain poorly characterized in terms of multiplicity. This is because these sources are even more deeply embedded than Class I protostars, and their multiplicity can typically only be examined at wavelengths $\gtrsim$10 μm. Since the protostar is obscured by a thick envelope, emission at $\lambda < 10$ μm is typically from scattered light and/or shock-heated material in the outflow

(e.g., Tobin et al. 2007; Seale & Looney 2008; Tobin et al. 2010); Thus, the multiplicity of Class 0 sources has been characterized principally with interferometers at millimeter and centimeter wavelengths due to limited resolution in the mid and far-infrared. Looney et al. (2000) conducted a 2.7 mm survey of 11 nearby Class 0 protostars, finding that all the protostellar sources were in multiple systems with separations between 140 AU and 8000 AU. Most, however, were found with separations > 400 AU (corrected for the updated distance to Perseus, d $\sim$ 230 pc Hirota et al. 2008, 2011). Maury et al. (2010) observed 5 systems at high angular resolution ($\sim 0\farcs4$), only finding single sources. They then claimed that there was no evidence for multiplicity in Class 0 sources on scales between 150 AU and 400 AU (also corrected for the updated distance to Perseus), based on their non-detections combined with the results from Looney et al. (2000).

More recently, Chen et al. (2013) used archival millimeter/submillimeter data taken toward Class 0 protostars to characterize multiplicity toward 33 systems. On scales between 50 AU and 5000 AU, Chen et al. (2013) found an MF of 0.64 and a CSF of 0.91, with most companions being separated by more than 1000 AU. The main limitation of that study was that it was not conducted in a uniform manner in terms of sensitivity or resolution. This is because the data were drawn from archival observations toward various star forming clouds at various distances. The survey had spatial resolutions that ranged between 30 AU and 1800 AU with a median of 600 AU. However, they found 3 multiple Class 0 systems with separations between 150 AU and 430 AU, with a total of 5 sources between 50 AU and 430 AU). This survey was a large step forward in the characterization of wide companions toward Class 0 protostars, but was limited in addressing close multiplicity.

Nonetheless there has been some progress in characterizing multiplicity on scales < 400 AU. Tobin et al. (2013) found two Class 0/I sources (out of a sample of 3) with companions separated by 100 AU. Moreover, Tobin et al. (2015b) found a companion toward the Class 0 system NGC 1333 IRAS2A separated by 142 AU, perhaps the driving source of a secondary east-west outflow observed in this system. Also, Tobin et al. (2015a) found a companion toward L1448 IRS3B separated by $\sim$210 AU. Thus, statistics have been building up for Class 0 sources at smaller separations, but in a slow, piecemeal fashion.

To make a large stride in the characterization of protostellar multiplicity in the Class 0 and I phases, a survey with uniformly high sensitivity and high-resolution (< 50 AU) is necessary. This is one of the driving goals of the VLA Nascent Disk and Multiplicity (VANDAM) survey, undertaken with the Karl G. Jansky Very Large Array (VLA). The VANDAM survey was conducted at Ka-band (8 mm and 1 cm), where the observations are sensitive to emission from both thermal dust and free-free jets. Furthermore, complementary observations were taken in C-band (4 cm and 6.4 cm) to characterize the spectral slope of the free-free emission. In this survey, we have observed all known protostars in the Perseus molecular cloud (82 Class 0 and I sources plus 12 Class II sources) in order to characterize the multiplicity of Class 0 and Class I protostars with as little sample bias as possible.

This paper is focused on the multiplicity results of the VANDAM survey derived from the Ka-

band data only. Several following papers will focus on the resolved disk candidates, polarization results, C-band radio spectra, and full survey results. The sample is described in Section 2, the observations, instrument setup, and data reduction are described in Section 3, the multiplicity results are described in Section 4, the results are discussed in Section 5, and the summary and conclusions are given in Section 6.

2. The Sample

The VANDAM sample leverages the large body of work that has already been done to identify and characterize the protostellar content within Perseus. The sample of sources we observed and the pointing centers are given in Table 1. Our sample is primarily based on the catalog published by Enoch et al. (2009), which considered all the available *Spitzer Space Telescope* (Werner et al. 2004) photometry and Bolocam[1] data taken toward Perseus. Enoch et al. (2009) lists 66 protostars within Perseus, 27 of which they classify as Class 0 and 39 are Class I based on T_{bol}. However, rather than a stringent transition from Class 0 to Class I, we refer to sources with 60 K $\leq T_{bol} \leq$ 90 K as Class 0/I objects because the measured T_{bol} has a dependence on viewing angle that can make Class 0 sources appear as Class I and vice-versa (Launhardt et al. 2013; Dunham et al. 2014). In addition, Per-emb-44 (SVS13) is also denoted a Class 0/I because its continuum and outflow properties are more consistent with Class 0 objects (Looney et al. 2000; Plunkett et al. 2013). We have also updated the L_{bol} and T_{bol} for the sources published in Sadavoy et al. (2014) that include *Herschel* photometry. Thus, from the sources listed in Enoch et al. (2009), we classify 27 as Class 0 sources, 8 Class 0/I sources, and 31 Class I sources in our sample.

While the Enoch et al. (2009) survey still represents the best near to far-infrared characterization published thus far, there have recently been candidate first hydrostatic cores (FHSCs) and Very Low Luminosity Objects (VeLLOs) identified by millimeter interferometry (Hirano et al. 1999; Enoch et al. 2010; Chen et al. 2010; Schnee et al. 2012; Pineda et al. 2011) that were not detected in the infrared. Moreover, some of the Enoch et al. (2009) sources that were listed as one source were known to comprise multiple millimeter continuum sources (e.g., Looney et al. 2000) and the low-resolution of *Spitzer* at 24 μm and 70 μm prohibited these sources from being identified as discrete objects by Enoch et al. (2009); all these sources, 11 in total, were added to the sample. Many of these Class 0 sources known from millimeter observations, but not detected clearly by *Spitzer*, were resolved in the far-infrared by *Herschel* (Pezzuto et al. 2012; Sadavoy et al. 2014). Many of these sources are highly obscured at 24 μm and may be analogous to the PACS Bright Red Sources (PBRS) discovered in Orion by Stutz et al. (2013). We note that the 70 μm emission from the source Per-emb-37 has a $\sim 6''$ position shift relative to the 24 μm position. This is due to the source being faint at 24 μm and a nearby Class II source being much brighter at 24 μm and shorter wavelengths. Per-emb-37 was also identified by Sadavoy et al. (2014) as a Class 0, while

[1] 1.3 mm continuum instrument on the Caltech Submillimeter Observatory

Enoch et al. (2009) classified it as Class I due to the mis-association of 70 μm emission with the shorter wavelength emission.

We also examined the *Herschel* 70 μm, 100 μm, and 250 μm maps of the Perseus region in an attempt to identify additional sources that may have been missed by the *Spitzer* survey. We found 17 sources that were bright at 70 μm and 100 μm and these were added to the sample; however, these sources are classified as either Class II or flat spectrum sources (borderline between Class I and Class II) (Evans et al. 2009). In total, our sample is comprised of the Enoch et al. (2009) sample plus 28 sources additional sources.

Thus, our sample contains all currently known/published Class 0/I protostars in the Perseus region and flat spectrum/Class II sources that are bright in the far-infrared. It is possible that there are some undiscovered protostars in Perseus, given that classifications for the entire cloud using *Herschel* photometry remain unpublished. However, our efforts to identify bright sources in the *Herschel* data did not turn up a significant number of new Class 0 or Class I sources. Therefore, the sample presented in Table 1 is as complete as possible, given the current knowledge of the protostar population in Perseus. The sample includes a total of 94 targeted sources, 37 of which are Class 0 protostars (FHSCs and VeLLOs included), 8 are Class 0/I protostars, 37 are Class I protostars (flat spectrum included), and 12 are Class II sources, see Table 1. The sources included in Enoch et al. (2009) are denoted by Per-emb-XX and the additional young stellar objects that did not have more common names are denoted EDJ2009-XXX (Evans et al. 2009), where X refers to a number. The sources not included in either of those catalogs are referred to by their most common name.

The range of luminosities sampled is between $\sim$0.1 L$\odot$ and $\sim$33 L$\odot$, with a median luminosity of 0.7 L$\odot$. The median luminosities of the Class 0 and Class I sources are 0.9 L$\odot$ and 0.7 L$\odot$, respectively. This range of luminosities is consistent with the typical distribution of protostellar luminosities observed in Orion and the Gould Belt Clouds (Dunham et al. 2014, 2015). Therefore, our sample is comprised of a reasonably representative sample of protostellar objects.

3. Observations and Analysis

3.1. Observational Setup and Procedure

We conducted observations with the VLA in B-configuration between 2013 September 28 to 2013 November 20 and in A-configuration during 2014 February 24 to 2014 May 31 and 2015 June 19 to 2015 September 21. The B-configuration (also referred to as B-array) has a maximum baseline (antenna separation) of 11.1 km and at 8 mm provides a resolution of $\sim$0.″2 (46 AU). The A-configuration (A-array) has a maximum baseline of 36.4 km, providing a resolution of $\sim$0.″065 (15 AU).

For each source in Table 1 we observed a single pointing toward the coordinates listed. However,

the sources Per-emb-21, Per-emb-42, IRAS4B′, and SVS13C were located less than 15″ from another source and one pointing was sufficient. Then the sources, EDJ2009-233, SVS3, EDJ2009-173, and EDJ2009-235 were serendipitously detected within the primary beams of adjacent target sources and we report their detections as well. Observations have been obtained for the entire sample in B-configuration (except for EDJ2009-268), and observations in A-configuration have been conducted for all sources detected in B-configuration.

The Ka-band observations were conducted in 8 GHz continuum mode using 3-bit samplers with one 4 GHz baseband centered at 36.9 GHz and another centered at 28.5 GHz. The full 8 GHz of bandwidth was divided into 128 MHz spectral windows, each having 64 channels that were 2 MHz wide, and we recorded full polarization products. The B-configuration scheduling blocks (SB) were 3.5 hours in length, observing three sources per SB. Each SB started with observations of the absolute flux density calibrator (3C48), followed by observations of the bandpass and polarization leakage calibrator (3C84). The observations were conducted with fast-switching, observing the complex gain calibrator (J0336+3218) for ∼25 seconds and then the source for ∼75 seconds. The pointing solutions were updated every 50 minutes and each source received ∼30 minutes of on-source integration in each scheduling block. Each scheduling block ended with an observation of 3C138 to calibrate the linear polarization angle; thus, the VANDAM dataset in B-configuration has all the necessary calibrations taken to examine the polarization toward these protostars at 8 mm and 1 cm. See Cox et al. (2015) for details on the polarization calibration and results toward NGC 1333 IRAS 4A.

The A configuration Ka-band data were observed with the same spectral setup, but with scheduling blocks that were 1.5 hr, 2.5 hr, or 2.75 hr in length. The shorter scheduling blocks were necessary due to the limited windows for observing Perseus during the A-configuration. The 1.5 hr scheduling blocks observed only 1 source and 2 sources were observed in the 2.5 hr and 2.75 hr blocks. Each A-array SB started in the same manner as the B-array SBs and we also achieved a similar on-source time. The difference was that we did not observe 3C138 at the end of the SBs and rely instead on 3C48 for polarization angle calibration.

3.2. Data Reduction

The VANDAM survey data were all reduced using the Common Astronomy Software Applications (CASA[2]) package (McMullin et al. 2007). The data taken in 2013 and 2014 were reduced using version 1.2.2 of the VLA pipeline in CASA version 4.1.0 and the data taken in 2015 were reduced using version 1.3.1 of the pipeline in CASA version 4.2.2. The two versions of the pipeline are found to produce consistent results for our data. The VLA pipeline applies flags generated by the online system, as well as at the edge-channels of the spectral windows where sensitivity is reduced. The

[2]http://casa.nrao.edu

pipeline then applies standard calibration procedures for the delays, bandpass calibration, absolute flux calibration, and the time-dependent gain and phase calibration. We inspected the resulting calibration tables to ensure proper calibration and that bad/uncalibrated data are not included in the final data products. We first verified the absolute flux density calibration accuracy by editing the gain table used as input to the *fluxscale* task. We flagged the calibrator solutions that were at significantly different elevations and those with substantial time variation. We then re-ran *fluxscale* with the edited calibration table and compared the flux densities calculated for the gain calibrator and bandpass calibration with those applied during the pipeline script. If the values agreed within 10% we accepted the flux density scale as-is, when they did not agree (only one SB), we flagged the known bad antennas and reran the pipeline. The overall uncertainty in the flux density scale is estimated to be $\sim$10%.

Following the flux density calibration check, we inspected the final gain versus time table and flagged gain solutions that were discrepant from the general trends versus time. We also inspected the gain versus frequency tables to ensure that specific spectral windows did not have abnormally large scatter. Lastly we inspected the phase versus time tables to identify periods of unusually large phase scatter or phase jumps. Following the gain table flagging, we ran the *applycal* task with the *mode=flagonly* option enabled, which flags the on-source data with no corresponding calibration data, based on the flagged gain tables.

We note that our reduction method only applies flagging *a posteriori* and the gain solutions are computed with some bad data. However, there is a large amount of redundancy in the computation of the closure phase and gain solutions because the VLA has 27 antennas. To determine the effect of *a posteriori* flagging versus *a priori* flagging, we imaged a dataset in which flagging was applied after pipeline calibration and then applied the same flags to a raw measurement set before running the pipeline. The source structure and root-mean-squared (rms) noise in the resultant maps were statistically indistinguishable. Therefore, we have used the *a posteriori* flagging method exclusively. The good agreement between these two methods is attributable to the redundancy in the data with so many antennas. Following the application of gain table flags, we split out each source into an individual measurement set, averaging all 64 channels in each spectral window to 1 channel for the Ka-band data.

With the measurement sets for each source, we generated naturally-weighted dirty maps of the full Ka-band (9 mm effective wavelength) and each 4 GHz baseband individually (8.1 mm and 1.05 cm effective wavelengths, respectively); multi-frequency synthesis imaging mode was used in all cases. We defined regions to deconvolve using the *clean* algorithm by drawing CASA regions around the peak source emission in each dirty map and then performed non-interactive cleaning down to $\sim$3$\times$ the rms noise using natural weighting. We then examined the cleaned images for additional source emission that was apparent after cleaning the strong sources. If additional source emission was detected, we repeated the above steps with additional clean masks. We also imaged the data using Briggs weighting with robust parameters of 0.5, 0.25, and 0; the robust parameter adjusts the relative weighting of the short and long baselines in the deconvolution process.

A robust parameter of 2 is comparable to natural weighting and typically produces an image with the lowest noise, but also lower resolution; a robust parameter of -2 is comparable to uniform weighting and has the best resolution but with a higher noise level because there are fewer data at the longer baselines relative to short baselines. Intermediate values of the robust parameter enable the image resolution and sensitivity to be adjusted to find an optimal balance. This methodology was applied to both the A and B configuration data. For the data with both A and B configuration observations, we produced a merged measurement set using the *concat* task and performed the same imaging steps as noted above. The largest angular scales that can be recovered in A and B-configurations are $\sim 0\farcs8$ (180 AU) and $\sim 2\farcs6$ (600 AU), respectively; these numbers apply to natural weighted maps, and the maps made using Briggs weighting (with robust between 0 and 0.5) will have smaller largest angular scales[3].

3.3. Data Analysis

To find companion sources, we visually inspected the images from each Ka-band baseband (8 mm and 1 cm) and the full bandwidth (9 mm) for multiple sources. We define a multiple system as the detection of multiple discrete continuum sources, detected at 8 mm with a S/N $\gtrsim$6 or at 9 mm with S/N $\gtrsim$ 5; however, if there is a previous detection in the near-IR, we allowed sources to have S/N of 4. We also examined images from each robustness level given that some companions only became apparent with robust levels <0.5; this is because the sources may be blended with natural weighting and only resolved at the higher resolution provided by images with a lower robust parameter. The flux densities of the sources (multiple and single) were measured using the CASA task *imfit*, and the peak flux densities are measured directly from the images. Most sources are within the inner $20''$ of the primary beam, so the correction is <15%. The integrated and peak flux densities reported for all sources have the primary beam correction applied.

For single sources, the flux densities were measured from the B-configuration image generated with natural weighting, given that those data would be most sensitive to the largest scale of emission. The flux densities of the multiples separated by <500 AU were measured from the A+B configuration images generated with natural weighting; the multiples separated by <50 AU have their flux densities measured from the A-configuration data alone. The spectral indices of the integrated and peak intensities were calculated from the 8 mm and 1 cm flux density measurements and the spectral index error results from the standard error propagation (Chiang et al. 2012). All the detected sources and companions have detections at both 8 mm and 1 cm.

The separations of multiple systems are determined by simultaneously fitting multiple Gaussian components and calculating the distance between Gaussian central positions. The measured flux densities of the single and multiple sources are given in Table 2. The separations of apparent

[3]https://science.nrao.edu/facilities/vla/docs/manuals/oss2016A/performance/resolution

companion sources are given in Tables 3, 4, and 5 and are further discussed in the following sections.

4. Results

The VANDAM survey data provide an unprecedented characterization of protostellar multiplicity in terms of sample size, angular/linear resolution, and sensitivity. The current results probe previously uncharted regions of protostellar companion separations, with a complete sample probing scales down to ∼15 AU. We identify multiple sources out to separations of 43″ (∼10000 AU; ∼0.05 pc). This upper limit to multiple system separation is not physically motivated, but this scale is at the half-power point of the VLA primary beam at 8 mm. However, this scale is also comparable to the typical radius of protostellar envelopes (0.05 pc; Benson & Myers 1989) and the break point at 0.04 pc between clustering (on larger scales) and multiplicity (on smaller scales) in the Taurus molecular cloud (Larson 1995). Moreover, on scales $\gtrsim$20″ multiplicity in Perseus has been characterized in the infrared and (sub)millimeter (e.g., Looney et al. 2000; Chen et al. 2013). Thus, the main discovery space opened by our survey is on scales less than 1000 AU. The nature of the multiple continuum sources we detect is discussed further in Section 5.

In total, we have found 26 multiple systems in the Perseus molecular cloud with our VLA data, assuming that sources out to 10000 AU constitute a single system; this number changes depending on the range of separations considered. Of these 26 multiple systems, 16 are new detections or reflect the discovery of a new component to an existing multiple system. The newly discovered multiple systems are described in Section 4.1. The continuum properties for all detected sources are given in Table 2, and the multiple systems broken down into classes are given in Tables 3, 4, and 5.

4.1. Close Multiples

4.1.1. Multiple Systems Separated by < 500 AU

The VANDAM data dramatically improve our knowledge of protostellar multiplicity on scales < 500 AU. Toward the Class 0 sources, in particular, there have only been a few studies with small samples having spatial resolution < 500 AU (e.g., Looney et al. 2000; Maury et al. 2010; Chen et al. 2013). Scales < 500 AU are important because this is the size of largest disks observe toward Class II sources (e.g., Simon et al. 2000), and at smaller scales companion sources may form within gravitationally unstable disks (Adams et al. 1989).

We identified 13 new companion sources separated by 30 AU to 500 AU out of the 18 total close multiple systems shown in Figure 1. Of these new companions, 5 are in Class 0 systems, 6 are in Class I systems, and 2 are in Class II systems. Prior to the VANDAM survey, only two Class

0 sources had been known to have companions on < 500 AU, NGC 1333 IRAS 4A and SVS13A (Looney et al. 2000; Rodríguez et al. 1999; Anglada et al. 2004). The companion toward NGC 1333 IRAS2A (Per-emb-27) was previously presented in the first VANDAM paper (Tobin et al. 2015b) and we include it with the new detections. We note that two Class I multiples (L1448 IRS1 and EDJ2009-183) in Figure 1 have companions that are quite faint. However, we know that these detections are real because the companions had been previously detected in the near-IR Connelley et al. (2008).

The companions with separations between 30 AU and 500 AU have a variety of relative flux densities, the faintest being ∼10 times fainter than the brightest source in the system, see Tables 3, 4, and 5. Furthermore, the spectral index of the 8 mm and 1 cm emission is positive for all companion sources, but often less than 2, indicating a combination of dust and free-free emission is responsible for generating the observed emission. The spectral index (α) for dust emission is expected to be steeply rising with $\alpha \sim 2 + \beta$ (if optically-thin), where beta is the dust opacity spectral index. Free-free emission typically has a flatter spectral index as compared to dust, with a 2 $\geq \alpha \geq$ -0.1 (Rodriguez et al. 1993). Non-thermal synchrotron emission on the other hand typically has $\alpha \sim$ -0.7 (Condon 1984). Thus, it is unlikely for any companion sources to be background extragalactic objects. See Section 4.6 for more details on the estimated number of extragalactic background sources.

4.1.2. Multiple Systems Separated by < 30 AU

The spatial resolution of 15 AU afforded by our observations enables us to uncover strong evidence for multiplicity on scales < 30 AU for 3 Class 0 sources. These three sources are shown in Figures 2, 3, and 4; the top panels show the emission at multiple resolutions and the bottom panels show the spectral index maps. All three systems are embedded within a larger structure and the companions are only revealed at the highest resolutions. Furthermore, the spectral index maps show that both dust and free-free emission are contributing to the source fluxes. These three close multiple sources have separations between 18.5 AU and 22.3 AU, making them the most compact multiple protostar systems directly detected. Previously, the closest known deeply embedded systems detected at millimeter/centimeter wavelengths were the 45 AU system in L1551 IRS 5 (Looney et al. 1997; Rodríguez et al. 1998) and the 40 AU system in IRAS 16293-2422A (Wootten 1989). The implications of these systems will be discussed further in Section 5.2 and more details of these sources are discussed in Appendix A. In addition to these three systems, four others showed evidence for resolved structure on <30 AU scales but did not have enough S/N to be regarded as a multiple system, and these additional sources are also shown in Appendix B.

4.2. Multiple Systems Separated by > 500 AU

We show images of the multiple systems on scales > 500 AU in Appendix C. Of the wide multiples shown, only Per-emb-37 (see Appendix C) is a new detection, though the companion sources are distinct in *Spitzer* IRAC imaging. Formally, our level of completeness is a function of separation given the decreased sensitivity away from field center, but the primary beam response is still 85% at 20″ from the field center. On scales >20″ (4600 AU), the multiplicity of protostars has been characterized at infrared and submillimeter wavelengths. We detect all known wide multiples with separations between 4600 AU and 10000 AU. The analysis of expected extragalactic background sources given in Section 4.6 suggests that there may be a background source within the VLA primary beam in a few fields. To check for such sources, we have cross-compared our images with infrared imaging from *Spitzer* or *Herschel* (Evans et al. 2009; Sadavoy et al. 2014) to verify that there are associated infrared sources with the wide multiple systems, and that their colors and flux densities that are inconsistent with being extragalactic objects.

4.3. Multiplicity Statistics

In our analysis of multiplicity in Perseus, we only consider the sources detected as multiples in our data and not those reported from other studies for consistent. See Appendix C for a discussion of non-detections of previously reported multiples. The detected Class 0 multiple systems are listed in Table 3, the detected Class I multiple systems are listed in Table 4, and the Class II multiple systems are listed in Table 5.

The MF and CSF (see section 1 for definitions) are the key figures of merit for describing the multiplicity for collections of stars. We have calculated these statistics for the VANDAM Perseus Survey: for the entire sample, MF = 0.40 ± 0.06 and CSF = 0.71 ± 0.06 (S:B:T:Q:5:6=37:17:5:2:2:1), for the Class 0 sources MF = 0.57 ± 0.09 and CSF = 1.2 ± 0.2 (S:B:T:Q:5:6=15:9:5:2:2:1), and for the Class I sources MF = 0.23 ± 0.08 and CSF = 0.23 ± 0.08 (S:B:T:Q=20:6:0:0), [4]. The statistics are further enumerated in Table 6 for different ranges of separations for the full sample, Class 0 sub-sample, and Class I sub-sample. Note that the Class 0 systems that have a wide Class I or Class II companion are only considered in the Class 0 MF and CSF, and the Class 0/I systems are also only considered in the Class 0 statistics. Furthermore, we only include the Class 0 and Class I systems detected in our survey within these statistics. Because the smallest separations that we can probe is ∼15 AU, the MF and CSF values given here and in Table 6 should be considered lower

[4]Note that the uncertainties throughout the text are calculated assuming binomial statistics, σ_{CSF} = (N_{comp}(1-N_{comp}/N_{sys})$^{-0.5}$ × 1/N_{sys} where N_{comp} is the number of companions and N_{sys} is the number of systems. σ_{MF} is calculated similarly, but by substituting N_{mult} (number of multiple systems) for N_{comp}. Poisson statistics are not used because the criteria of $N_{comp} >> N_{sys}$ is not met. However, we note that the variance calculated assuming binomial statistics is only slightly smaller than that of Poisson statistics. For the case of CSF > 1.0, σ_{CSF} is not a real number and we revert to Poisson statistics in this case.

limits.

The Class II sources have MF = 0.33 ± 0.19 and CSF = 0.33 ± 0.19 (S:B:T:Q=4:2:0:0), but our survey only included a small number of Class II sources and these systems are bright in the far-infrared. Thus, the Class II statistics are biased and too small to draw meaningful conclusions.

The multiplicity of Class 0 protostars was previously examined by Chen et al. (2013) and those authors found MF=0.64 ± 0.08 and CSF = 0.91 ± 0.05 for a separation range of 50 AU to 5000 AU. For the Class 0 multiples within this separation range, we find an MF = 0.45 ± 0.09 and CSF = 0.88 ± 0.06. The results are comparable, and the difference in the MF could be due to sample bias in Chen et al. (2013) and the fact that we do not detect multiplicity toward all Perseus sources where Chen et al. (2013) reported multiplicity (see Sections 5 and the Appendix for further discussion).

For the Class I sources, Connelley et al. (2008) find a MF = 0.35 ± 0.03 and CSF = 0.45 ± 0.04 (S:B:T:Q=122:51:12:4). Duchêne & Kraus (2013) presented a combined analysis of Connelley et al. (2009) and Duchêne et al. (2007) to derive a CSF of 0.35 ± 0.05 for Class I sources with separations between 50 AU and 2000 AU. For Class I multiples in the same separation range, we find both the MF and CSF = 0.28 ± 0.08; this is consistent with the results of Duchêne & Kraus (2013) within the uncertainties. We note that there are two systems comprised of a Class 0 and a Class I source within this range of separations that were included in the Class 0 statistics only. If we added these sources to the Class I statistics, the MF and CSF would be more consistent with the Duchêne & Kraus (2013) value.

We find that the overall values of MF and CSF for the Class 0 and Class I sources are not significantly different from previous studies, despite our larger and improved sample for several reasons: 1) many systems already considered multiple in the MF were found in our survey to have additional closer systems, 2) the number of new multiple systems is balanced by the number of additional systems confirmed to be single, and 3) some systems previously considered to be multiple are not confirmed in our study. The MF of Class 0s is lower, likely due to our unbiased sample which detected more single systems. Furthermore, past studies have often focused on systems that were known to be multiple, and samples were biased to the brightest sources at millimeter wavelengths.

4.4. Separation Distribution

Figure 5 shows the distribution of companion separation for our full sample and for the Class 0 and Class I sub-samples, using the separations listed in Tables 3, 4, and 5. For systems comprised of 3 or more members, the distances are all referenced to a single source, usually the most luminous. Thus, only two separations are considered for a triple system, not all three possible separations. In the case of a quadruple (or higher order) comprised of two close multiple systems (e.g., L1448-N, Appendix C) then only the brightest members in each close multiple system are used to compute the distance to the more widely separated system. For the full sample, we find a bi-modal distribution

with peaks at separations of ∼75 AU and ∼3000 AU. Between these peaks there is a valley with only 7 companion sources detected between 200 AU and 1000 AU. There is also a notable decline in multiplicity at separations < 57.7 AU, with only three sources having strong evidence of multiplicity. We emphasize that the range of spatial scales examined and the numbers of multiple systems detected and characterized is currently without precedent, especially for a sample within the same molecular cloud at a common distance. Much of the improvement in statistics comes at scales less than 500 AU, where there had been few previous observations. The largest previous study for Class 0 protostars by Chen et al. (2013) had median resolution of 600 AU. We do note, however, that the statistical significance of the two peaks is marginal in the histograms, but we will statistically compare the cumulative distribution in the following section.

The size of our sample enables us to examine the multiplicity of Class 0 and Class I systems independently and Figure 5 also shows several key differences between the Class 0 and Class I separation distributions. First, the Class I systems have a peak in companion frequency at ∼75 AU scales and only a few multiples on scales larger than 100 AU. The Class 0 systems on the other hand retain the double-peaked distribution seen for the full sample. We constructed cumulative distributions for the two samples (see Figure 6) and performed an Anderson-Darling (AD) test[5] (Scholz & Stephens 1987), the results of which indicate that the probability of the Class 0 and Class I sources being drawn from the same distribution is only 0.17. The inclusion of wide multiples comprised of both Class 0 and Class I sources with Class 0 would decrease the probability of the two samples being drawn from the same distribution, but if they were included with the Class I distribution only, that would make it more likely that the Class 0 and Class I samples were drawn from the same distribution. Thus, our results are suggestive of differences between the separation distributions of the Class 0 and Class I protostars but with marginal statistical significance.

4.5. Constraining the Functional Form of the Separation Distribution

We compared our dataset to several simple models to determine what the data can and cannot rule-out in terms of the underlying separation distribution. There are several possible models that could describe the underlying distribution of separations, and we tested a log-flat distribution, a model that represents the fields solar-type star separation distribution, and a model that employs multiple Gaussian functions.

We first compared to a log-flat distribution of multiples between 15 and 10000 AU, also known as Öpik's Law (Öpik 1924). Such a distribution would produce a constant level of multiplicity at all separations in a histogram like that of Figure 5. The cumulative distribution for a log-flat

[5]The Anderson-Darling test is similar to the Kolmogorov-Smirnoff (KS) test, but is more statistically robust. This because the KS-test uses the maximum deviation to calculate the probability and is not as sensitive when deviations are at the ends of the distribution or when there are small but significant deviations throughout the distribution. https://asaip.psu.edu/Articles/beware-the-kolmogorov-smirnov-test

distribution of separations is drawn in Figure 7 and compared to the data. The log-flat distribution is always in excess of the observed distribution, except for the largest separations, and the AD probability for this distribution is 0.08, so a log-flat distribution of separations is unlikely.

We also considered a model that represents the separation distribution of field solar-type multiple systems. The distribution was fit with a Gaussian by Raghavan et al. (2010) with a mean $log(a) = 1.7$ ($\sim$50 AU) and $\sigma_{loga} = 1.52$ in units of log(AU). These are derived from $log(P) = 5.03$, $\sigma_{logP} = 2.28$ in units of log(days) assuming a 1.5 $M_{\odot}$ primary mass. We compare our separation distribution to the Raghavan et al. (2010) fit, finding an AD probability of 0.00009, indicating that the separation distribution of solar-type multiples is very unlikely to match that of our protostellar multiples. The disagreement provides further evidence that binary systems dynamically evolve from their initial separations.

Finally, the double-peaked histogram in Figure 5 suggests that the separation distribution might be represented by two Gaussians. We compared the observed distribution to a grid of Gaussian functions and found that two Gaussians are consistent with the data (probabilities of 0.99 are achieved). However, the parameters of the Gaussians are not well-constrained; a typical fit has the inner peak at $\sim$ 90 AU and the outer peak between 3000 AU and 10000 AU.

4.6. Extragalactic Background Estimation

Extragalactic sources that are dominated by synchrotron emission increase in brightness at longer wavelengths and can become a source of contamination in sensitive radio surveys. We have followed the analysis for background objects presented in Anglada et al. (1998) to estimate the number of background source that we expect to find in our survey. Our typical sensitivity was 10 μJy, thus we estimate the number of extragalactic background sources at Ka-band with a flux density $\geq$30 μJy within a 5$''$ (1150 AU) field of view. This is done by extrapolating the 5 GHz number counts and assuming a typical spectral index of α = -0.7 for optically-thin synchrotron emission (Condon 1984). We find that there is a probability of only 3.3 $\times 10^{-4}$ of finding a background source within a 5$''$ field of view; the probability becomes 0.041 for a 60$''$ field of view. This analysis ignores the potential contributions of radio emission from submillimeter galaxies, where the combination of bright dust and free-free emission associated with star formation will likely produce flatter spectral indices, making them more detectable. For 90 observed fields, we expect to detect $\sim$4 extra-galactic sources. We conclusively identify two likely extragalactic sources in our observations, see Tables 1 and 2. They have negative spectral indices at Ka-band and no corresponding detections at shorter wavelengths. These numbers are consistent with the expected number of extragalactic sources considering that a portion of the fields observed overlapping regions of sky. Thus, it is very unlikely that any close or wide multiples are false detections due to extragalactic confusion.

5. Discussion

The origin of stellar multiplicity has gained significant attention recently due to the downward revision of solar-type star multiplicity frequency to 0.46 (Raghavan et al. 2010) and the finding that the fraction of single M-stars is ∼0.63 (Lada 2006). Furthermore, the searches for brown dwarf and planetary mass companions around pre-main sequence stars (e.g., White & Ghez 2001; Köhler et al. 2006; Reipurth et al. 2007; Kraus et al. 2008, 2011), have produced large statistical samples of multiplicity. Nevertheless, connecting these statistics to multiple star formation remained uncertain due to a lack of definitive results on the multiplicity and separation distribution toward embedded protostars.

The primary routes for the formation of multiple systems are (1) the fragmentation of the core or filament and (2) disk fragmentation. Core fragmentation can be either thermal (Jeans) fragmentation aided by rotation and asymmetry (e.g., Burkert & Bodenheimer 1993; Bonnell & Bastien 1993) or turbulent fragmentation (Padoan & Nordlund 2002, 2004; Offner et al. 2010); these routes tend to produce companions on ∼1000 AU scales, but can also result in companions with ultimate separations < 100 AU via migration (Offner et al. 2010; Bate 2012). Fragmentation of the protostellar disk via gravitational instability can also directly form close companion systems (e.g., Adams et al. 1989; Bonnell & Bate 1994a; Kratter et al. 2010; Zhu et al. 2012).

Large simulations of entire star forming molecular clouds have been conducted with enough resolution to examine fragmentation on the scales from the cloud down to the disks (e.g., Bate 2009, 2012). The multiplicity results from such simulations are typically compared to the field star multiplicity; however, several Gyr of dynamical evolution in the field population will impact such comparisons to simulations of younger systems. Observations of more deeply embedded multiple systems, such as those presented in this paper, will provide a more direct diagnostic to test models of star formation, given that their ages are most likely all less than 0.5 Myr (Dunham et al. 2014), comparable to the length of time explored in the simulations.

There has been debate on the origin and frequency of multiplicity in the Class 0 protostellar phase, centering around studies that have small, biased samples of sources. Looney et al. (2000) examined 11 Class 0 protostellar systems, finding a preponderance of multiplicity in these systems. However, the sources in the sample are among the brightest millimeter sources in the nearby star forming regions and may not be representative. Maury et al. (2010) then examined 5 systems (including 2 Very Low Luminosity Objects, protostellar sources which have internal luminosities < 0.1 $L_\odot$; Young et al. 2004), not finding any multiples on scales $\lesssim 1600$ AU. Their sample, combined with that of Looney et al. (2000), led them to conclude that there was no evidence for multiplicity on scales between 150 AU and 400 AU for Class 0 protostars; the separation of 400 AU reflects the updated distance to Perseus, which affects the separation of NGC 1333 IRAS4A. Moreover, Maury et al. (2010) went on to tentatively suggest that multiplicity *increased* from the Class 0 to Class I phase, at least for separations between 150 AU and 400 AU. This would not necessarily be a true increase in multiplicity but possibly an evolution in separations from initially wider separations to

closer separations (e.g., Offner et al. 2010; Zhao & Li 2013). Nonetheless, the robustness of these findings was unclear given the small sample sizes of both Maury et al. (2010) and Looney et al. (2000).

Chen et al. (2013) made use of archival SMA data to better characterize multiplicity in the Class 0 phase using a sample of 33 protostars located in various star forming regions. For the separation range (50 AU to 5000 AU), Chen et al. (2013) showed that the multiplicity fraction for Class 0 protostars is ∼0.65. This is much higher than the ∼0.35 for Class I systems (Connelley et al. 2008) and ∼0.2 for solar-type field stars (Raghavan et al. 2010), indicating that multiplicity is highest in the Class 0 phase in this separation range. However, that study did not necessarily rule-out the conclusion by Maury et al. (2010) of multiplicity increasing for separations between 150 AU and 400 AU. This is because Chen et al. (2013) lacked homogeneous sensitivity and resolution (median resolution of 600 AU), but multiples were reported by Chen et al. (2013) in the range between 150 AU to 400 AU.

The VANDAM survey surmounts these limitations of the previous studies by observing a large number of protostars (94; 77 detected) in a single star forming region, at nearly uniform sensitivity (apart from the sensitivity attenuation of the primary beam) and resolution. Multiple sources can be resolved with separations as small as ∼0.″065 (15 AU). This survey contains the largest and least biased sample of protostars ever observed with sub-arcsecond resolution. This survey also boasts the highest ever sensitivity in the 8 mm to 1 cm wavelength range for protostellar multiples. Thus, we have been able to characterize protostellar multiplicity with unprecedented statistics.

Although the results from this survey represent enormous progress, there are limitations to how well multiplicity can be characterized in the context of the protostellar properties. A major limitation is that we do not know the masses of the protostars (or systems) themselves. We only know the bolometric luminosities sampled from the near-infrared to submillimeter, which range between ∼0.1 L⊙ and ∼ 33 L⊙, with a median of 0.7 L⊙. The range and distribution of luminosities are typical of the population of known protostars (Dunham et al. 2014, 2015). However, it is not trivial to directly translate luminosity to stellar mass for protostars because the emergent luminosity is dominated by (or has a significant component from) accretion processes that can be highly variable.

To make estimates of the protostar masses, we can compare to models of the protostellar luminosity function with an underlying protostellar mass function, assuming smooth accretion (Offner & McKee 2011; McKee & Offner 2010). Within the context of these models, most protostars in our sample are expected to be progenitors of K and M-stars. However, even if those models are reliable, the bolometric luminosities of the components to multiple systems separated by $\lesssim$ 1500 AU cannot be determined due to the resolution limitations at mid to far-infrared wavelengths. Thus, we cannot say anything about the mass or luminosity ratios of the close protostellar binaries themselves. Finally, there is an inherent bias in characterizing multiplicity at millimeter/centimeter wavelengths, and we may not detect all companion sources as evidenced by some of the faint companion sources

detected toward some Class I systems. Therefore, our statistics represent lower limits to the MF, CSF, and the companion frequency as a function of separation, see section 5.6 for further discussion.

5.1. Origin of the Bi-modal Separation Distribution

The distributions of separations shown in Figure 5 represent the most complete snapshot of protostellar multiplicity and also the highest resolution study that has been compiled in a single star forming region. It is tempting to interpret the distribution of separations as the initial distribution of separations in multiple systems; however, even at these very young ages it is possible that significant migration has already taken place (e.g., Offner et al. 2010; Bate 2012). For example, systems driving orthogonal outflows, but with close separations, like NGC 1333 IRAS2A (Tobin et al. 2015b), may have resulted from migration. Nevertheless, our sample of embedded multiples, especially the Class 0 systems, should have a separation distribution that is closer to the initial separation distribution than what would be obtained from more evolved sources. Thus, the VANDAM survey provides the best direct constraints on the origin of multiplicity thus far.

The most striking feature of the separation distribution for the full sample and Class 0 sources in Figure 5 is that the distribution appears bi-modal, with one peak near ∼75 AU and the other near ∼3000 AU. This feature is unlikely to be the result of any selection bias because we have observed all the known protostars in the Perseus molecular clouds. Furthermore, our spatial resolution and sensitivity are sufficient to have detected multiples between 100 AU and 1000 AU if they were present.

An attractive interpretation of the bi-modal distribution is that the peaks are produced by two distinct mechanisms, namely disk and core fragmentation, respectively. Disk fragmentation would naturally produce the multiples of $\lesssim$ 300 AU scales and core fragmentation would then produce the multiplicity on scales $>$ 1000 AU. Early studies of thermal (Jeans) fragmentation of dense cores concentrated on the effects of rotation and non-spherical shape (e.g., Bonnell & Bastien 1993; Burkert & Bodenheimer 1993). More recent calculations have focused on fragmentation induced by turbulence (Walch et al. 2010; Offner et al. 2010; Padoan & Nordlund 2002). The complex structure and velocity fields often observed toward protostellar cores may provide some evidence for this picture (Tobin et al. 2011; Pineda et al. 2011, 2015). Furthermore, wide multiples produced through turbulent fragmentation can tighten their separations through orbital migration on timescales as short as 10 kyr, potentially contributing to the close multiple population (Offner et al. 2010). However, if the close multiples are the result of migration, some mechanism must then cause them to accumulate at $\sim$ 75 AU rather than continuing to migrate inward.

The differences in the separation distributions for the Class 0 and Class I systems are suggestive of evolutionary effects. Class 0 systems have considerably more wide multiples than Class I systems. The orbital period for a 4000 AU separation binary system is ∼250 kyr (assuming 1 $M_{\odot}$), and if the systems dissolves due to internal dynamics, the timescale should be longer than an orbital

period. This timescale is likely too long for protostellar systems because the expected lifetime of a Class 0 system is only ∼160 kyr (Dunham et al. 2014). Therefore, we consider two additional interpretations related to the formation and evolution of these systems.

The first possibility is that wide multiples had formed initially, and as they evolved into the Class I phase the separations increased because the companions may have been unbound at the time of formation due to initially large differential velocities as a result of turbulent fragmentation. While it is true that systems are not binary/multiple if they are not gravitationally bound, we are unable to assess whether or not all systems are bound. Therefore, we presently consider all systems with projected separations less than 10000 AU as a bound multiple system. The boundedness of the widely separated systems is an active area of investigation (e.g., Lee et al. 2015, Lee et al. in prep.), and systems that are currently bound within their star forming cores may later become unbound as their envelope material is dispersed by outflows (Arce & Sargent 2006; Offner & Arce 2014).

The second possibility is that the wide multiples dynamically evolved toward close separations, giving rise to the peak at ∼75 AU. We regard the first possibility as more likely because, many of the wide Class 0 multiples are separated by more than 1000 AU, making it possible that some of these systems would be unbound. In addition, the fraction of multiples at < 300 AU scales is comparable for both Class 0 and Class I sources. The similarity at scales < 300 AU can be explained by either wide multiples not frequently migrating to < 300 AU scales or by the currently observed Class 0 multiples at < 300 AU migrating to scales < 15 AU (i.e., are now unresolved). The >1000 AU companions would then need to migrate and fill-in the distribution at < 300 AU scales.

Turbulent fragmentation and disk fragmentation are expected to produce multiple systems that appear nearly coeval. On the other hand, the Class 0 sources with widely separated Class I or Class II companions may also be evidence that significant, rapid orbital evolution does not happen in all cases or that an additional process is at work. A promising route to explain these systems is a dynamical ejection scenario (Reipurth & Clarke 2001; Reipurth et al. 2010; Reipurth & Mikkola 2012). In this scenario, a close triple system would have formed initially and dynamical interactions cause one member to be ejected into a very wide orbit. Even though the ejected companion would be as young as the remaining compact binary, it might appear more evolved because it would no longer be so deeply embedded and perhaps directly visible at near-infrared wavelengths. Thus, the widely separated systems with different evolutionary states could be very young stars that were ejected from their cores.

5.2. Multiplicity Evolution

A principle conclusion of Chen et al. (2013) was that multiplicity is decreasing with evolution, decreasing from the Class 0 phase to the Class I phase within the separation range of 50 AU to 5000

AU. However, a limitation of that survey was the inhomogeneous resolution (median resolution of 600 AU). In comparison, the VANDAM survey consists of a large, homogeneous sample at ∼15 AU resolution. With this large dataset, we can examine the multiplicity frequency of Class 0 and Class I systems separately.

We also showed the apparent differences between the Class 0 and Class I multiplicity distributions at separations > 1000 AU in Figure 5 (see Section 4.4), and that there is marginal evidence for a statistical difference in the separations between the two populations. We can also compare the Class 0 and Class I populations in terms of their MF and CSF. Note that we count those Class 0 systems with a wide Class I or Class II companion in the MF and CSF for the Class 0 sources only. Our main results are unchanged if these sources were also included in the Class I statistics.

Across the full range of separations, from 15 AU to 10000 AU, we find that multiplicity is decreasing from the Class 0 to the Class I phase, in agreement with Chen et al. (2013) and in contrast with Maury et al. (2010). For example, we the MF = 0.57±0.09 for Class 0s and MF = 0.23±0.08 for Class Is. If we then examine the separation range from 15 AU to 5000 AU (the same outer limit as Chen et al. 2013), we still find decreasing multiplicity from Class 0 to Class I (MFs of 0.55±0.09 and 0.24±0.08, respectively). The same is true if we examine the separation range from 50 AU to 5000 AU (the same range as Chen et al. 2013), though we find that the MF for Class 0 sources is 0.45±0.09 and 0.24±0.08 for Class I sources. We note, however, that our value of Class I multiplicity is consistent within the uncertainties with both the Connelley et al. (2008) value of 0.35±0.03 and the value for field solar-type stars from Duquennoy & Mayor (1991) for the separation range between 50 AU and 5000 AU as calculated by Chen et al. (2013). Thus, while we confirm a multiplicity decrease on these scales from Class 0 to Class I, we do not confirm a further decrease from Class I to field stars from our data alone.

In contrast to the larger separations, the MF and CSF between 15 AU and 2000 AU of the Class 0 and Class I subsamples are consistent within the uncertainties. Thus, we conclude that on scales less than 2000 AU, there does not appear to be multiplicity evolution taking place between the Class 0 and Class I phase. Maury et al. (2010) had suggested that multiplicity increased from the Class 0 to the Class I phase on these scales, but this suggestion is not supported by our larger sample. Furthermore, Maury et al. (2010) suggested that there was no evidence for multiplicity between 150 AU and 550 AU (400 AU). While multiples are clearly found within this range of separations in our study and that of Chen et al. (2013), there is a deficit in multiples in this range of separations relative to smaller and larger scales. Suffice it to say that there is, however, evidence for slightly lower multiplicity for both Class 0 and Class I systems between 150 AU and 1000 AU.

5.3. Evidence for Disk Fragmentation

Three remarkable systems (IRAS 03292+3039/Per-emb-2, IRAS 03282+3035/Per-emb-5, and Per-emb-18) show multiplicity on scales < 30 AU; see Figures 2, 3, and 4. In each of these

cases, the sources are surrounded by an extended structure and only become resolved into discrete sources when imaged at higher resolution. IRAS 03292+3039/Per-emb-2 and Per-emb-18 have the largest continuum structures detected in our survey, about 1.″5 and 1″ in diameter, respectively. The A-configuration data resolve-out the extended emission and reveal additional brightness peaks separated by ∼19 AU in both cases. It is peculiar that the extended dust emission is only on the eastern side of Per-emb-18, having the appearance of a companion itself when viewed at lower resolution. The dusty structure surrounding IRAS 03282+3035 is only ∼0.″5 in diameter.

Gravitational instability in a disk is the most likely mechanism for the production of any substructures detected on scales <30 AU. This scale, however, this scale is near the inner limit of where the disk is expected to cool quickly enough for gravitational instability to make a bound object (Rafikov 2005; Matzner & Levin 2005). Thus, these companions may have migrated to their current locations from initially larger radii or the disks were cold enough to allow fragmentation on these scales due to the source luminosities being low; L_{bol} = 0.9, 1.3, and 2.8 for Per-emb-2, Per-emb-5, and Per-emb-18, respectively.

The masses associated with the extended structures on 0.″5 to 1.″5 scales are estimated to be > 0.1 $M_{\odot}$ from 1.3 mm dust emission (Tobin et al. 2015a). However, a missing piece of evidence is the dense gas kinematics, which is necessary to determine whether or not these clumps are the result of a fragmenting, rotationally supported disk. In the case of IRAS 03292+3039, there is evidence of inner envelope rotation (Schnee et al. 2012; Yen et al. 2015), suggesting that a rotationally supported disk is possible for this source. There have also been molecular line data for IRAS 03282+3035 (Arce & Sargent 2006; Yen et al. 2015), but a rotation signature is unclear toward this source and Per-emb-18 does not yet have existing observations.

The clumpy structure observed toward IRAS 03292+3039 on > 0.″5 scales appears real, sub-peaks within this structure have close coincidence with peaks observed at 1.3 mm (Tobin et al. 2015a). However, the 1.3 mm data have a much smoother appearance, a possible indication that the dust emission is optically thick at 1.3 mm, but optically thin at 8 mm and 1 cm. It is unclear if the clumpy structures surrounding the source have formed or are likely to form protostellar objects. The peaks observed north and south of the main protostar(s) are also present at 1.3 mm and when the 8 mm data are imaged at higher resolution (with lower S/N).

While we are confident that the structures observed on <30 AU scales are real, it is uncertain if they were formed in their current locations, given that fragmentation via gravitational instability is difficult at this scale. Furthermore, the ultimate fate of these structures is uncertain. For instance, gravitationally unstable disk models often show clumps that have yet to collapse into stellar objects migrating inward (Vorobyov & Basu 2006, 2010). Some clumps can be tidally disrupted if they have not formed a bound object, or they may be accreted on to the protostar (Zhu et al. 2012). The accretion of these clumps results in an increased luminosity and could be an explanation for the large spread observed in the luminosity distribution of young stellar objects (Dunham et al. 2014). If each of the observed structures is associated with a stellar object, then it is unlikely for them to

merge together. Thus, these structures could be transient or they might reflect the formation of close companions.

Another way to produce substructures in the dust emission is the Rossby Wave Instability (RWI) (Barge & Sommeria 1995; Klahr & Henning 1997). Bae et al. (2015) showed that RWI can be triggered in protostellar disks by the velocity shear of the material falling onto the disk. This process could possibly explain some of the features we observe, e.g., the asymmetric dust clump around Per-emb-18. However, the RWI only concentrates the dust and not gas, and the largest dust grains are more highly concentrated than the smaller grains. Thus, in this scenario, the detection of clumps would not necessarily be related to multiple star formation (e.g., van der Marel et al. 2015). Observations of molecular line kinematics will help elucidate the nature of the small-scale substructures and these sources are close enough that orbital motion can possibly be observed in just a few years time.

5.4. Orientation of Multiple Systems

Figure 8 shows the distribution of relative position angles between the close companions (separations < 500 AU) and the outflow axis of the protostars; the list of position angles is given in Table 7. The disk around the protostar is assumed to be oriented normal to the outflow direction (at least the portion driving the jet); therefore, if close companions have formed in the rotational plane as a result of disk fragmentation or fragmentation of the rotating envelope this should be reflected in the distribution of relative position angles. For comparison, we also draw the distributions for a uniform distribution of angles and the distribution of relative position angles for a random distribution of binary orbital phases and inclinations.

Without performing any statistical tests, it is apparent that the observations have a small excess of sources with small relative position angles over what would expected for randomly oriented circular orbits (dotted line in Figure 8). This is a random distribution of companion orbital phase and viewed with a random inclination, consistent with companions being located in the plane of the disk, normal to the outflow direction. The bottom panel of Figure 8 shows a scatter plot of companion separation versus position angle and there are no apparent trends. The average relative position angle is 50° in the observations, while the average angle for randomly oriented circular orbits is ∼70°. Elliptical orbits in the disk plane would not help resolve the inconsistency because the companion would spend more time at apastron and more sources would be expected to have relative PAs closer to 90°. Close companions formed via turbulent fragmentation are not expected to follow a preferred orbital configuration and could be partly responsible for the disagreement. Note, however, that the multiple system NGC 1333 IRAS2A (Per-emb-27) has two orthogonal outflows and we only list the dominant north-south outflow in the table, resulting in a small relative position angle. Including the east-west outflow as an independent point or instead of the north-south outflow would reduce the excess. Thus, the number of close companions with measured outflow position angles is currently too small to currently draw definitive conclusions. However, the distribution of

relative outflow position angles for both the close and wide multiple systems is being investigated further with new outflow data for the entire sample of Perseus protostars (Lee et al. in prep.).

Follow-up of these sources will enable proper motions to be measured and determine if companions are co-moving or rapidly moving away. If the companion sources are found to be moving away rapidly, then they are most likely to be blobs of free-free emission in the jet and not true companion sources; an event like this has been observed in the source IRAS 16293-2422A (Pech et al. 2010). However, the spectral indices of the companions are positive and not consistent with being optically thin free-free knots. Furthermore, the distribution of spectral indices for companions is indistinguishable from that of the single protostars, see Section 5.6.

5.5. Comparison to T Tauri Multiples in Taurus

The best characterized group of young stellar multiples is in Taurus, where Kraus et al. (2011) combined new observations down to 3 AU scales with previous multiplicity searches. This survey of visual multiples is sensitive to separations between 3 AU and 5000 AU for primary star masses ranging between 0.25 $M_\odot$ and 2.5 $M_\odot$. The large number of stars enabled the sample to be divided into low-mass and high-mass sub-samples. The high-mass sub-sample has a roughly uniform distribution of companions (in log(separation)) out to 5000 AU, while the low-mass sub-sample has very few companions at scales $>$ 200 AU.

We compare our results to their sample in the cumulative distribution shown in Figure 9 for separations ranging between 15 AU and 5000 AU. Both the full sample and low-mass sub-sample ($M_* < 0.7\ M_\odot$) from Kraus et al. (2011) appear inconsistent with the distribution of multiples found in our sample, having AD probabilities of 0.014 and 0.00008, respectively. The high-mass subsample ($2.5\ M_\odot \geq M_* > 0.7\ M_\odot$), on the other hand, appears consistent with our distribution having an AD probability of 0.86. The primary difference between the low-mass sample and the high-mass sample is a lack of wide multiples in the low-mass sample. Considering the Class 0 and Class I systems separately, the Class 0s agree best with the high-mass sample with an AD probability of 0.76 and the Class Is agree best with the full sample with an AD probability of 0.21. For the other possible combinations with the Taurus sample, the Class 0 and Class I are likely to not have been drawn from the same distributions with AD probabilities less than 0.085.

The separation distribution agreement with the high-mass subsample ($2.5\ M_\odot \geq M_* > 0.7\ M_\odot$) and the strong disagreement with the full/low-mass sample ($M_* < 0.7\ M_\odot$) is quite striking and can be interpreted in several ways. If we assume that companion separations do not significantly evolve between the Class 0 to Class II/III phases, then one could infer that the multiple protostar systems that we detect are going to be progenitors of high-mass systems. While protostellar mass measurements are not available, the closest available proxies for stellar mass are either luminosity or core mass. McKee & Offner (2010) and Offner & McKee (2011) examined both the protostellar mass function and protostellar luminosity functions. The observed protostellar luminosities can be

reproduced with a mass function closely following the Chabrier IMF; the two component turbulent core model (2CTC in their Figure 3). With this underlying mass function, the typical protostellar mass is $\sim$0.2 $M_{\odot}$ and only $\sim$14% of sources should have masses between 0.7 and 2.5 $M_{\odot}$, thus our sample should be comprised of mostly sources < 0.7 $M_{\odot}$. Furthermore, we observe no specific trend in multiplicity with respect to bolometric luminosity and there is no obvious trend with core mass. However, core mass will change with evolution as the protostars accrete material and outflows remove material from the envelope; most Class 0 systems have core masses > 0.5 $M_{\odot}$ (Enoch et al. 2009).

If the protostars we observe in our sample are indeed characteristic of the low-mass Taurus systems, then they must have undergone significant dynamical evolution since their formation and the binary orbits have contracted. Therefore, the separation distribution that we observe toward the protostars could evolve toward what is observed for the low-mass Taurus systems. If this interpretation is true, then by inference the high-mass systems in Taurus may have not undergone significant dynamical evolution. We caution that these statements implicitly assume that the Perseus and Taurus multiples will follow the same evolutionary path.

The paucity of low-mass Taurus systems with wide separations could imply that low-mass systems do not typically fragment on large-scales or that the low-mass systems cannot hold onto wide companions. It is unknown if the wide multiple systems in Perseus are bound. If these wide systems drift apart over time, then the distribution of separations in Perseus would become less consistent with the high-mass Taurus sample and more consistent with the low-mass Taurus sample. It was also argued in Kraus et al. (2011) that the high-frequency of close companions in the low-mass Taurus sample could be indicative of disk fragmentation occurring preferentially on a 50 AU - 100 AU scale. This finding is consistent with our distribution of close separations which peaks at $\sim$ 75 AU.

Furthermore, Kraus et al. (2011) argued that the mass ratio of close companions being consistent with a log-flat distribution is suggestive of disk fragmentation taking place after the primary has accumulated most of its mass, accounting for $\gtrsim 1/2$ the entire core mass. If disk fragmentation occurred early in protostellar evolution, Kraus et al. (2011) argued that the mass ratio would be skewed toward unity rather than log-flat. It is unclear if such a signature is present in our sample given that the Class 0 and Class I systems have similar numbers of companions separated by $<$ 300 AU.

Finally, it is also possible that the agreement and/or disagreement between the Perseus multiples and Taurus multiples is completely coincidental and reflects the different properties of the two clouds and their YSO populations. The two regions have significantly different clustering properties, gas densities, temperatures, and ratios of protostars to pre-main sequence stars. Thus, the differences could simply result from the different initial conditions.

5.6. Nature of 8 mm and 1 cm Emission

Continuum emission at 8 mm and 1 cm likely include significant contributions from both thermal dust emission and thermal free-free (Bremsstrahlung) are likely. The dust emission is likely tracing the protostellar disk and/or inner envelope and the free-free emission is thought to be produced from ionized gas resulting from shocks at the base of the protostellar jet on scales $\lesssim 10$ AU (e.g., Curiel et al. 1989; Anglada et al. 1998). Free-free emission typically becomes dominant, with respect to dust emission at $\lambda > 1$ cm. Discrete sources detected at centimeter wavelengths toward protostellar cores, have also been associated with multiple star formation (Rodríguez et al. 2000; Anglada et al. 2004; Reipurth et al. 2002, 2004). This is because the presence of free-free emission enhances the detectability of protostellar sources, where dust emission may be faint depending on the properties of the source. However, there are some examples of spatially-extended free-free emission with multiple clumps along the outflow (Rodriguez et al. 1989, 1990; Curiel et al. 1993), but these sources have luminosities > 50 $L_\odot$ and they have observed proper motion in the outflow direction (Rodríguez et al. 2000; Rodriguez et al. 1989). Furthermore, clumps of emission created along free-free jets should be preferentially aligned with outflows, which is not observed survey (see Figure 8).

Figure 10 shows the distributions of spectral indices from the Ka-band observations. The histograms and cumulative distributions of spectral indices calculated from the integrated flux densities and peak flux densities are quite comparable. The spectral index of optically thick emission (dust or free-free) will be ∼2. Optically thin free-free emission will have a spectral index of ∼ -0.1 and optically thin dust emission will have a spectral index of $\sim 2 + \beta$; β in dense dusty disks or inner protostellar envelopes is typically $\lesssim 1$ (e.g., Testi et al. 2014; Kwon et al. 2009), in contrast to interstellar medium dust which has $\beta \sim 2$ (e.g., Draine & Lee 1984). Most spectral indices are less than 2, indicative of an at least partially optically thin free-free contribution to the Ka-band flux density , causing spectral indices that are flatter than pure thermal dust emission.

The detection of compact free-free emission is strong evidence for the presence of a protostar, given the requirement of a jet-driving source. However, a lack of detected free-free emission is not evidence for the absence of a protostellar source. Nearly all the candidate companions exhibit a combination of free-free and dust emission at 8 mm and 1 cm, with varying levels of strength. The spectral index of the free-free emission is indicative of the physical conditions, extended jet emission toward higher-luminosity sources is generally optically thin (spectral index ∼-0.1), while protostellar sources typically have spectral indices between 0 and 2. The source NGC 1333 IRAS2A VLA2 described in Tobin et al. (2015b) has a spectral index of 1.7 and models of free-free emission (Ghavamian & Hartigan 1998) indicate that shock velocities in excess of 150 km s^{-1} and/or densities $\sim 10^9$ cm^{-3} are required to have such optically thick free-free emission. Such extreme conditions favor generation of emission on small-scales close to a protostellar source rather than from a jet impacting the surrounding medium. A detailed analysis of the dust and free-free contributions using the 4 cm and 6 cm for the full sample and newly detected multiples will be analyzed in a future paper (Tychoniec et al. in prep.).

Each component of the multiple systems identified in this paper represents spatially compact emission on scales less than 30 AU. The densities required to produce detectable dust emission and the necessity of a jet driving source to produce free-free emission makes it highly probable that the detected sources are indeed protostellar in origin.

5.6.1. VLA-detected Companions at Millimeter Wavelengths

Many of the multiple systems uncovered by our VLA data do not currently have data available with comparable resolution at millimeter wavelengths to verify pure dust emission associated at shorter wavelengths. Sensitive, high-resolution data (0.″3; 5x coarser than the VLA A-configuration data) do exist for a few sources. L1448 IRS2 (Per-emb-22), L1448 IRS3 (A,B, and C), and NGC 1333 IRAS2A (Per-emb-27) were observed at 0.″3 resolution at 1.3 mm by Tobin et al. (2015b,a). NGC 1333 IRAS4A was observed by Looney et al. (2000) and Jørgensen et al. (2007) at 2.7 mm and 1.3 mm, respectively.

For L1448 IRS2, the companion separated by 0.″75 that was detected in the VANDAM data is not detected at 1.3 mm. The 1.3 mm emission is, however, extended toward the companion position. L1448 IRS3B was found to be a triple system in the VANDAM data, with a close pair separated by 0.″26 and separated from the main source by 0.″9 (Tobin et al. 2015a). At 1.3mm, the main source is detected and the close pair is well-resolved from the main source; the close pair themselves are marginally resolved. L1448 IRS3C, which is identified in the VANDAM data as a close binary (0.″25) is marginally resolved at 1.3 mm, having a deconvolved position angle consistent with the orientation of the multiple system. NGC 1333 IRAS2A (Per-emb-27) has a companion separated by 0.″62 and there is a marginal (5σ) detection at 1.3 mm at the companion location. Lastly, the more widely separated companion toward NGC 1333 IRAS4A (1.″8) is detected at 2.7 mm, 1.3 mm, and at $\sim$850 μm (Lay et al. 1995).

While these are only a few examples, as a whole we can suggest that multiplicity at millimeter wavelengths is often also reflected at 8 mm and 1 cm, but not in all cases. The companions toward L1448 IRS2 and NGC 1333 IRAS2A (Per-emb-22-B and Per-emb-27-B) were undetected or marginally detected at 1.3 mm, indicating that there is less than $\sim$0.001 $M_{\odot}$, of compact mass traced by dust emission surrounding both of these companions (assuming Ossenkopf & Henning (1994) dust opacities, a dust to gas mass ratio of 1:100, and a dust temperature of 20 K). The estimated flux densities from dust emission at 8 mm from these two sources would be 22 μJy and 8 μJy for Per-emb-22-B and Per-emb-27-B, respectively. This would be below our sensitivity, thus the detected emission at 8 mm must have a significant contribution from free-free emission. At longer wavelengths, IRAS2A VLA2 (Per-emb-27-B) is detected at 4 cm, but not 6.4 cm (Tobin et al. 2015b).

The detection of free-free emission is strong evidence for the presence of a protostellar source driving at jet. Therefore, the most likely explanation for their lack of strong millimeter emission is

a lack of concentrated circumstellar dust or compact, optically thick circumstellar dust. This may imply that any circumstellar disk around these companions is quite low mass. Without significant circumstellar dust, it is unlikely that ALMA will be able to detect such companion sources out of the extended circumstellar dust surrounding the primary protostars. Therefore, to gain a complete picture of multiplicity, observations at longer wavelengths where other emission mechanisms contribute to the emergent flux are crucial to fully characterizing protostellar multiplicity.

5.6.2. Potential Bias in Millimeter/Centimeter Characterizations of Multiplicity

The methods of characterizing multiplicity toward Class 0 protostars are fundamentally different from those typically employed to characterize multiplicity of Class I and more-evolved systems. Direct-detection of stellar or inner-disk radiation can be employed in most cases to characterize the multiplicity toward Class I and more evolved systems. Moreover, adaptive optics and other high-contrast imaging techniques can be used to identify close multiples, in addition to radial velocity monitoring. These techniques cannot be employed for Class 0 and early Class I protostellar systems due to the high extinction through the protostellar envelopes and the large amount of scattered light emission typically associated with young stars.

Characterizing multiplicity in protostellar systems relies on the indirect methods of detecting circumstellar dust emission and/or free-free emission, with the implicit assumption that multiple sources in the emission maps reflect discrete protostellar objects. Dust emission is expected to reflect dense concentrations of dust in the form of a circumstellar disk or an inner envelope near the individual protostars (e.g., Rodríguez et al. 1998; Terebey & Padgett 1997; Looney et al. 2000; Chen et al. 2013). However, a clump of material in a protostellar disk or envelope does not necessarily harbor a protostellar source and it is unknown whether such clumps will form a protostellar source. For free-free emission, it is necessary to assume that the emission is originating from shocks near the base of the protostellar jet on < 10 AU scales (Curiel et al. 1989; Anglada et al. 1998).

Multiplicity characterized by dust emission assumes that the protostellar sources either have increasing density toward them or compact, emission from a circumstellar disk. The fundamental problem with using dust emission to characterize multiplicity lies in the assumption that peaks in the millimeter dust emission harbor protostellar sources. We fail to detect some previously reported multiplicity in some Class 0 systems (see Appendix C.13), but our results are consistent with the millimeter detections in most cases, especially for the wider multiples detected by Looney et al. (2000) and Chen et al. (2013). We emphasize that caution will be needed when interpreting continuum data in the ALMA era given that sensitivity is typically $>10\times$ better than was possible with PdBI/NOEMA, CARMA, and the SMA. ALMA data are already enabling many more low-surface brightness features to be detected, which may or may not harbor or go on to form protostars (e.g., L1521F; Tokuda et al. 2014).

The dust emission detected in our VLA survey is largely immune from the detection of low-

surface brightness, extended sources due to our observations at high resolution, requiring that dust emission be quite concentrated to be detected, let alone not be resolved-out. However, note the case of Per-emb-18 where we detected an extended dust structure that does not appear to harbor a companion, but its appearance is quite distinct from that of point-like emission. Per-emb-2 also has a very extended and apparently clumpy structure and most of this extended emission is resolved-out at higher resolution. Moreover, we are typically detecting a combination of dust and free-free emission at Ka-band. This is demonstrated by the spectral index being less than 2 (Figure 10). The addition of free-free emission is advantageous because it enhances the detectability of the protostars.

We can conclude that there are not likely many false detections in our sample from free-free emission associated with outflow shocks. The strong outflows toward SVS13, IRAS2A, L1448C, IRAS4A, and HH211 do not yield detections of Ka-band emission associated with shock knots in the outflows. Furthermore, the close companion to SVS13 (SVS13A2) does not exhibit significant proper motion away from SVS13A (Carrasco-González et al. 2008a), nor is it associated with a shock feature in high-resolution near-infrared imaging (Hodapp & Chini 2014). We have also examined the distribution of spectral indices in the Ka-band of the close multiples ($<$ 500 AU separations) relative to the single sources, and the histograms and cumulative distributions are quite comparable. We performed an AD test on the samples to see how likely the are to be drawn from the same distribution. The resulting probabilities are 0.7 and 0.35 for the integrated and peak spectral indices, respectively, indicating that the spectral indices for the singles and multiples are likely drawn from the same distribution. Thus, we argue that the Ka-band data are unlikely to have significant numbers of false companions.

The characterization of multiplicity from both dust emission and free-free emission has potential pitfalls. Both methods can lead to detections of sources that are not truly protostellar and both can also yield non-detections toward genuine protostellar sources. Therefore, the biases associated with the characterization of multiplicity are difficult to quantify and correct for.

5.6.3. Completeness Limits

The discussion in Section 5.6 illustrates the difficulties in quantifying the incompleteness of our multiplicity detections given that dust and free-free emission process are not directly connected to physical properties of the source, i.e., protostellar mass. The best, albeit poor, proxy for mass is L_{bol}, and this value can only be determined for the system as a whole, not individual components of multiple systems separated by $<$ 1000 AU. Figure 11 shows the histograms of L_{bol} and plots of 8 mm flux density versus L_{bol}. These figures show that the few non-detections in our Class 0 and Class I protostellar samples are typically the lower luminosity sources. In the case of the Class 0 sources, many of the non-detections are candidate FHSCs. However, we cannot simply assign a minimum luminosity that we can detect because some of the lowest luminosity sources are well-detected. Furthermore, the single sources similarly show a broad scatter in terms of 8 mm flux

density at a given luminosity. This makes us unable to assign a lower-limit to the luminosity of companions that we are able to detect from single sources, nor can we provide a lower mass limit.

Therefore, it is possible that there may be non-detections of some companions due to a lack of concentrated dust emission and/or free-free emission toward some companions. Given that we are examining multiplicity from indirect methods that do not directly correlate with source properties, the level of incompleteness cannot be quantified with any degree of accuracy, nor can we give sensitivity limits as a function of mass ratio and separation. Thus, the multiplicity statistics derived from millimeter/centimeter studies should be further considered as lower limits. Moreover, we cannot examine multiplicity at scale smaller than 15 AU, making our MF and CSFs lower limits.

While we cannot reliably quantify our level of incompleteness, we do detect all the currently known infrared companions (i.e., EDJ2009-183 and L1448 IRS1 Connelley et al. 2008) and most millimeter companions (except for VeLLOs/candidate FHSCs). Furthermore, our observed CSF of Class I protostars is consistent with the near-infrared studies. Thus, incompleteness may not be a serious issue given the agreement of our results with those obtained from independent techniques.

6. Conclusions

We have conducted a multi-wavelength VLA survey (8 mm, 1 cm, 4 cm, and 6.4 cm) of all known protostellar systems in the Perseus molecular cloud and presented our results on the multiplicity of the protostellar systems based on our 8 mm and 1 cm data. Our survey observed an unprecedented number of systems with uniform sensitivity and resolution in a single star forming region. The high-resolution data taken in A and B configurations have enabled us to carry out a relatively unbiased characterization of protostellar multiplicity down to 15 AU scales for all protostars in the Perseus molecular cloud. We note, however, that the MF, CSF, and companion frequencies with separation given in this paper are most likely lower limits. This is because of the inherent bias associated with detecting multiplicity from the presence of dust or free-free emission toward companions and there are likely unresolved systems at separations smaller than our resolution limit.

1. We detect 18 multiple systems with separations between 15 AU and 500 AU, of which 16 are new detections by the VANDAM survey. This increases the number of known Class 0 systems with companion separations between 15 AU and 500 AU by more than a factor of two.

2. The distribution of protostellar companion separations in Perseus appears bi-modal or double-peaked, with one peak at $\sim$75 AU and the second peak at $\sim$3000 AU. We argue that the double-peaked distribution is suggestive of two formation mechanisms for the wide and close multiple systems, disk fragmentation for scales $\lesssim$ 300 AU and core/turbulent fragmentation for scales larger than 1000 AU.

3. The MF and CSF for separations from 15 AU to 5000 AU (and 10000 AU) are larger for Class 0 sources than Class I sources and field solar-type stars, confirming the results Chen et al.

(2013). However, for separations $\leq$ 2000 AU, the MF and CSF of Class 0 sources are consistent with Class I sources and field solar-type stars.

4. The distribution of separations for the Class 0 and Class I sources appear different. There is a clear deficit of wide companions toward Class I sources relative to Class 0 sources, which we interpret as evidence for evolution of companion separations between the Class 0 and Class I phases. Systems could either form or become unbound as the star forming gas is dispersed. Alternatively, wide companions could migrate inward. However, the MF and CSF for Class 0 and I protostars are consistent with each other on scales between 15 AU and 2000 AU. Therefore, a significant fraction of multiples may not be migrating inward from >1000 AU separations.

5. We detect companions embedded within extended dust continuum structures toward 3 systems (Per-emb-2/IRAS 03292+3039, Per-emb-5/IRAS 03282+3035, and Per-emb-18); the companions are separated by $\leq$30 AU. We interpret this structure as evidence on-going disk fragmentation in these systems, given that the companion sources are found within a larger surrounding structure. Though the surrounding structures are not confirmed to be rotationally-supported, this is the first observed evidence for such small-scale substructure toward young protostars.

6. WE compared our distribution of separations to the Taurus pre-main sequence samples from Kraus et al. (2011). The separation distribution for the Perseus sample is more consistent with the high-mass Taurus sub-sample (2.5 $M_{\odot} \geq M_{*} > 0.7\ M_{\odot}$) than their low-mass sub-sample ($M_{*} < 0.7\ M_{\odot}$). The primary difference is the number of wide companions. If the wide systems in Perseus are not bound, then the separation distribution may evolve to be more consistent with the Taurus low-mass sub-sample. We caution, however, that the comparisons of Perseus and Taurus may not be valid given the differences in the star formation conditions.

7. While millimeter observations of the newly discovered multiple systems are not complete, both L1448 IRS2 and NGC 1333 IRAS2A have existing 1.3 mm observations with sufficient resolution to resolve the VLA-detected companions. However, the companions are not convincingly detected at 1.3 mm. This result carries the implication that ALMA may not be able to completely characterize protostellar multiplicity because not all protostellar companions will be detectable. Moreover, optically thick dust emission on <100 AU scales may inhibit the detection of embedded companions separated by <50 AU at millimeter/submillimeter wavelengths.

8. We demonstrate that close companions are likely to be real sources and not knots of free-free emission in the outflows. First there is a lack of correlation between companion separation and relative position angle between the outflow and companions, and secondly the distribution of spectral indices for companion sources is consistent with having the same distribution as single protostellar sources. While we cannot absolutely rule-out the possibility that some companions are features of the protostellar jet interacting with the surrounding cloud, proper motion studies can be carried out on timescales of a few years to determine whether or not the sources move in the jet direction or if the companion sources are co-moving. Orbital motion will likely require longer time baselines of order 10-20 years to determine.

We thank the anonymous referee for constructive suggestions that improved the quality of the manuscript. The authors wish to thank K. I. Lee, A. Stutz, B. Reipurth, J. Jorgensen, A. Kraus, and L. Tychoniec for useful discussions regarding this work. J.J.T. is currently supported by grant 639.041.439 from the Netherlands Organisation for Scientific Research (NWO). J.J.T. acknowledges past support provided by NASA through Hubble Fellowship grant #HST-HF-51300.01-A awarded by the Space Telescope Science Institute, which is operated by the Association of Universities for Research in Astronomy, Inc., for NASA, under contract NAS 5-26555. L.W.L. acknowledges support from the Laboratory for Astronomical Imaging at the University of Illinois and the NSF under grant AST-07-09206. Z.Y.L. is supported in part by NSF1313083 and NASA NNX14AB38G. C.M. acknowledges financial support from the U.S. National Science Foundation through award AST-1313428. M.M.D. acknowledges support from the Submillimeter Array through an SMA postdoctoral fellowship. This research made use of Astropy, a community-developed core Python package for Astronomy (Astropy Collaboration, 2013, http://www.astropy.org). This research made use of APLpy, an open-source plotting package for Python hosted at http://aplpy.github.com. This research has made use of NASA's Astrophysics Data System. The National Radio Astronomy Observatory is a facility of the National Science Foundation operated under cooperative agreement by Associated Universities, Inc.

Facilities: VLA

A. Notes on Multiple Sources with < 30 AU Separations

A.1. Per-emb-2/IRAS 03292+3039

Figure 2 shows the source Per-emb-2 (IRAS 03292+3039) at 9 mm (top) and the 8 mm - 1 cm spectral index maps (bottom), generated using the *nterms=2* option in the CASA *clean* task. The A+B configuration images, tapered at 1000 kλ are shown in the left panel, emphasizing the structured extended emission; the extent of the resolved structure agrees with the 1.3 mm observation presented by Tobin et al. (2015a). When zooming in on the inner region in the middle panel with the A-configuration-only image, the extended structure is resolved-out. The main source appears extended and another source clearly detected with a separation of 18.5 AU when imaged with Briggs weighting, shown in the right panel of Figure 2. The spectral index is $\sim$2 at the peak intensity, but the extensions north and east have steeper spectral slopes indicative of dust emission. In the higher resolution images, the eastern source has a spectral index of $\sim$3, while the western source has a spectral index of $\sim$1.5. The shallower spectral index is an indication that both dust and free-free emission are contributing to the source flux.

A.2. Per-emb-5/IRAS 03282+3035

Per-emb-5 (IRAS 03282+3035) is shown in Figure 3; it is resolved at lower resolutions in the left panels of Figure 3, but the emission is not as extended as Per-emb-2. The middle panels of Figure 3 begin to show double-peaked structure with a separation of 22.3 AU. The highest resolution data in the upper right panel also shows that the eastern peak is resolved. The eastern source also has a steeper spectral index ($\sim$3), indicative of dust emission being the dominant emission component. The spectral index of the western source is shallower ($\sim$1), suggesting that it has a larger contribution from free-free emission than the eastern source.

A.3. Per-emb-18

Per-emb-18 (NGC 1333 IRAS 7), shown in Figure 4, shows an apparent secondary source in the low-resolution image in the left panels of Figure 4 with a separation of $\sim$84 AU. When viewed at higher resolution in the middle panels, the apparent secondary source appears resolved-out and is most likely an extended dust structure; thus, we do not consider it as a companion source. However, the main source then shows evidence of resolved structure. The upper right panel of Figure 4 appears double peaked with a separation of 19.6 AU. Both sources have shallow spectral indices indicating that free-free emission is dominating at the source location and there is evidence for a steeper spectral index between the sources, suggesting dust emission between the two sources.

B. Possible Close Multiples

In addition to the clear multiples that are presented in the main text, there are several sources for which resolved structure is apparent, but the significance of the detections are below the 5σ criteria or only detected in one band. We show these sources in Figure 12. These sources are only revealed at the highest resolutions or only with the increased sensitivity of the combined A and B configuration data. These may be resolved disk structures or possibly bonafide companions and their nature may be further revealed by higher sensitivity imaging.

C. Notes on Multiple Sources with $>$ 500 AU Separations and Specific Multiple Systems

C.1. IC348 MMS

IC348 MMS/Per-emb-11 was previously identified as a multiple system with $15''$ separation by Chen et al. (2013); the VLA 9mm image is shown in Figure 13. Rodríguez et al. (2014) also identified another source separated by $\sim 3''$ southwest at 2.1 cm and 3.3 cm (JVLA3a); the

brightest source in Figure 13 is associated with Per-emb-11-A at the center of the image and denoted JVLA3b by Rodríguez et al. (2014). JVLA3a/Per-emb-11-B appears coincident with the MIPS 24 μm source, and it is directly between outflow cavities evident at shorter wavelengths (Pech et al. 2012). JVLA3b/Per-emb-11-A seems to be located to the side of the outflow cavity and Pech et al. (2012) showed CO outflow possibly misaligned with knots observed at IRAC wavelengths. Finally, Tobin et al. (2015a) presented 1.3 mm imaging toward IC348 MMS with $0\farcs3$ resolution and 1 mJy sensitivity; the 1.3 mm emission toward JVLA3b is well-detected, but JVLA3a is not. A reexamination of the image finds that there is indeed a 3σ peak at the position of JVLA3a at 1.3 mm. The spectral index of JVLA3a/Per-emb-11-B is positive in Ka-band as well as from 3.3 cm to 2.1 cm, but overall shallow. Thus, JVLA3a may be protostellar in nature but with faint continuum emission at 1.3 mm.

C.2. NGC 1333 IRAS4B

The wide multiple system of IRAS 4B and IRAS 4B$'$ is well detected by the VLA at 9mm (Figure 14), with a separation of 2450 AU. Both sources have resolved structure at this wavelength. Compact outflows originating from the two sources were identified by Hull et al. (2014), and they are in nearly orthogonal directions.

C.3. Per-emb-16 and Per-emb-28

Per-emb-16 and Per-emb-28 comprise a wide multiple system in the IC348 region. Per-emb-16 is a Class 0 object and Per-emb-28 is classified as a Class 0/I source. Per-emb-28 is notable because it shows a high degree of periodic variability, possibly from pulsed accretion (Muzerolle et al. 2013). Both sources are rather faint at 9 mm, see Figure 15.

C.4. NGC 1333 IRAS7

Within the system collectively known as NGC 1333 IRAS7, Per-emb-18, Per-emb-21, and Per-emb-49 are found to comprise a quintuple system, see Figure 16. Both Per-emb-18 and Per-emb-49 have companions separated by less than 100 AU and Per-emb-21 is single. Per-emb-49 appears to be a Class I source, while Per-emb-18 and Per-emb-21 are Class 0 objects. Per-emb-18 appears to drive a long system of HH objects, while Per-emb-21 has a relatively compact outflow (Davis et al. 2008).

C.5. L1448C

We detected both components of the L1448C system, Per-emb-26 (L1448C-N) and Per-emb-42 (L1448C-S), see Figure 17. These sources were previously resolved by *Spitzer* observations (Jørgensen et al. 2006; Tobin et al. 2007) and at submillimeter and millimeter wavelengths (Hirano et al. 2010; Maury et al. 2010). Per-emb-42/L1448C-S is located in the direction of the outflow from Per-emb-26/L1448C-N; however, an independent outflow is found to originate from Per-emb-42/L1448C-S (Hirano et al. 2010). Per-emb-42 may be more evolved than L1448C, given that it is classified as a Class I by Enoch et al. (2009).

C.6. L1448N/IRS3

The L1448 IRS3 (also known as L1448-N) system comprises Per-emb-33 (L1448 IRS3B), L1448 IRS3A, and L1448NW, the three components are within a radius of 5000 AU, see Figure 18. A companion in the Class 0 system L1448 IRS3B (Per-emb-33) had been reported by Tobin et al. (2015a), but the VLA observations have resolved the secondary into two distinct sources making Per-emb-33 a triple. L1448NW is also found to be a binary in our study, the previous CARMA observations of Tobin et al. (2015a) had noted that this source was extended. Thus, the as a whole is a sextuple. L1448NW is the most widely separated system from the rest, 4945 AU from Per-emb-33 and 3749 AU from L1448 IRS3A. Per-emb-33 and L1448NW are both Class 0 systems and L1448 IRS3A is likely Class I. Then Per-emb-26 (L1448C) is ∼18500 AU south of Per-emb-33 and Per-emb-22 is ∼41000 AU (0.2 pc) to the west. The kinematics and outflows of this system are analyzed in detail by Lee et al. (2015).

C.7. SVS13

The SVS13 (HH 7-11 region)is comprised of three main sources: SVS13A, B and C, as denoted by Looney et al. (2000), see Figure 19. Per-emb-44 (SVS13A) is the driving source of HH 7-11 and the companion SVS13B was first tentatively identified by Grossman et al. (1987); subsequent maps of the region by Chini et al. (1997) confirmed the detection of SVS13B and identified the source that is now known as SVS13C as MMS3. Looney et al. (2000) confirmed all of these detections with interferometry at 2.7 mm. SVS13B is ∼3400 AU from SVS13A and SVS13C is ∼ 4500 AU from SVS13B.

Per-emb-44 (SVS13A) itself is a close binary (first discovered by Rodríguez et al. 1999) and it has another companion 1222 AU away which we refer to as SVS13A2 (also known as VLA3 Anglada et al. 2004). Carrasco-González et al. (2008b) examined the proper motions of sources in this region and found that SVS13A2 is indeed co-moving with the other sources and not likely to be an outflow ejection. Per-emb-44 is classified as Class I, but its outflow power is comparable to Class 0 sources

(Plunkett et al. 2013). SVS13B and SVS13C also appear to be Class 0 sources (Sadavoy et al. 2014), but their nature is more uncertain given their close proximity Per-emb-44, a bright source from the near to far-infrared, making photometry difficult. Finally, another source is apparent northeast of Per-emb-44 in Figure 19, denoted VLA20 by Rodríguez et al. (1999). This source had been classified as a YSO by those authors given its rising spectral index, but no counterpart is detected in the infrared (e.g., Jørgensen et al. 2006) or the millimeter (Looney et al. 2000). We find that this source has a flat spectral index in Ka-band; this and the lack of counterparts at millimeter and infrared wavelengths indicate that this source is most likely extragalactic in nature and we do not consider it in the multiplicity statistics.

C.8. NGC 1333 IRAS2B

NGC 1333 IRAS2B has an apparent companion separated by $3\farcs8$ (∼870 AU), in addition to the 72.5 AU companion source, see Figure 20. However, the more widely separated source does not appear to be physically associated with the IRAS2B system. Its position is coincident with an optically visible star (BD +30 547) that appears to be illuminating the near side of the dark cloud and not embedded like IRAS 2B, suggesting that this is a line-of-sight alignment (Rodríguez et al. 1999). Therefore, we do not consider the more widely separated source in the multiplicity statistics. However, BD +30 547 could be a Class III source given that it appears to be located physically close to the molecular cloud. BD +30 547 also has a negative spectral index, possibly indicative of gyrosynchrotron emission from an active corona (Dulk 1985).

C.9. Per-emb-8 and Per-emb-55

Per-emb-8 and Per-emb-55 form another Class 0 - Class I wide binary system separated by ∼2200 AU. Per-emb-55 itself is a close binary,separated by 142 AU, see Figure 21. Per-emb-55 is quite bright in the IRAC bands, while Per-emb-8 is faint and shows some diffuse emission.

C.10. Barnard 1-b Region

The B1-b region comprises the three sources B1-bN, B1-bS, and Per-emb-41, see Figure 22. Both B1-bN and B1-bS have been suggested to be candidate first hydrostatic core objects and are faint even at 70 μm; B1-bS is also quite faint at 100 μm (Pezzuto et al. 2012). Per-emb-41 appears to be more evolved and is classified as Class I, having bright emission at IRAC wavelengths.

C.11. Per-emb-37

Per-emb-37 was mentioned in Section 2 because it is a Class 0 source that had been incorrectly associated with a brighter IRAC source and subsequently classified as Class I. Sadavoy et al. (2014) also detected this source in their search for Class 0 sources in Perseus. We do not detect all the infrared-associated sources in the 8 mm image, see Figure 23, but two sources are detected at 8 mm with separations of 2428 AU and 7752 AU. Thus, Per-emb-37 is the only new wide multiple reported in this study.

C.12. Per-emb-35

Per-emb-35, also known as NGC 1333 IRAS1, is located on the western outskirts of NGC 1333. It is particularly interesting that this source is found to be a ∼440 AU binary (Figure 1), given that it is also found to have a apparent S-shaped outflow in the *Spitzer* image of the region (Gutermuth et al. 2008). Thus, the companion could pay a role in shaping the outflow morphology.

C.13. Non-Detections Toward Previously Reported Multiples

There are a few cases where multiplicity has been previously reported toward sources in Perseus, but we do not confirm the presence of companion sources. One notable case is NGC 1333 IRAS2A (Per-emb-27) where a candidate companion was reported by Codella et al. (2014) and Maury et al. (2014), along with a non-protostellar continuum source. As discussed extensively in Tobin et al. (2015b), we did not detect these sources in the VLA data nor at 1.3 mm and 850 μm, despite having sufficient sensitivity at all wavelengths given their measurement of the spectral index. We did, however, discover a new companion with our VLA data separated by 142 AU. Thus, it is likely that the new VLA-detected companion is the driving source of the second outflow from this system (Sandell et al. 1994) and that the other reported sources are spurious; see Tobin et al. (2015b) for more details.

HH211-mms (Per-emb-1) was reported to have a candidate companion separated by $0\farcs3$ (∼69 AU) in Lee et al. (2009) and Chen et al. (2013) with 870 μm data. We failed to detect a companion toward this source in our VLA data. Moreover, the companion is not detected in CARMA 3 mm A-array data with $0\farcs3$ resolution (H.-F. Chiang, private communication). The lack of detection at multiple wavelengths casts doubt on the robustness of the claimed companion. It was only detected in an image generated with super-uniform weighting and could be spurious. The flux density of the companion at 870 μm is 25 mJy; assuming optically thin emission and a dust opacity spectral index of 3, the estimated peak flux density at 8.1 mm is 31 μJy at about our 3σ sensitivity limit. Therefore, the source detected by Lee et al. (2009) could be a dust clump that is most apparent at 870 μm.

Finally, Chen et al. (2013) reported a companion toward IRAS 03282+3035 (Per-emb-5) separated by 1.″5 (345 AU) at 870 μm. We did not detect a companion at this location in our VLA data, nor did Tobin et al. (2015a) detect this source at 1.3 mm. Thus, the lack of detection at multiple wavelengths suggests that this companion is likely spurious.

REFERENCES

Adams, F. C., Ruden, S. P., & Shu, F. H. 1989, ApJ, 347, 959

Allen, P. R., Koerner, D. W., McElwain, M. W., Cruz, K. L., & Reid, I. N. 2007, AJ, 133, 971

André, P., Ward-Thompson, D., & Barsony, M. 1993, ApJ, 406, 122

Anglada, G., Rodríguez, L. F., Osorio, M., et al. 2004, ApJ, 605, L137

Anglada, G., Rodríguez, L. F., & Torrelles, J. M. 2000, ApJ, 542, L123

Anglada, G., Villuendas, E., Estalella, R., et al. 1998, AJ, 116, 2953

Arce, H. G., & Sargent, A. I. 2006, ApJ, 646, 1070

Aspin, C., Sandell, G., & Russell, A. P. G. 1994, A&AS, 106, 165

Bachiller, R., Gueth, F., Guilloteau, S., Tafalla, M., & Dutrey, A. 2000, A&A, 362, L33

Bachiller, R., Guilloteau, S., Gueth, F., et al. 1998, A&A, 339, L49

Bae, J., Hartmann, L., & Zhu, Z. 2015, ArXiv e-prints, arXiv:1503.02694

Barge, P., & Sommeria, J. 1995, A&A, 295, L1

Bate, M. R. 2009, MNRAS, 392, 590

—. 2012, MNRAS, 419, 3115

Benson, P. J., & Myers, P. C. 1989, ApJS, 71, 89

Bonnell, I., & Bastien, P. 1993, ApJ, 406, 614

Bonnell, I. A., & Bate, M. R. 1994a, MNRAS, 269, L45

—. 1994b, MNRAS, 271, 999

Boss, A. P., & Keiser, S. A. 2013, ApJ, 764, 136

—. 2014, ArXiv e-prints, arXiv:1408.2479

Burkert, A., & Bodenheimer, P. 1993, MNRAS, 264, 798

Carrasco-González, C., Anglada, G., Rodríguez, L. F., Torrelles, J. M., & Osorio, M. 2008a, AJ, 136, 2238

Carrasco-González, C., Anglada, G., Rodríguez, L. F., et al. 2008b, ApJ, 676, 1073

Chen, X., Arce, H. G., Zhang, Q., et al. 2010, ApJ, 715, 1344

—. 2013, ApJ, 768, 110

Chiang, H., Looney, L. W., & Tobin, J. J. 2012, ApJ, 709, 470

Chini, R., Reipurth, B., Sievers, A., et al. 1997, A&A, 325, 542

Codella, C., Maury, A. J., Gueth, F., et al. 2014, A&A, 563, L3

Condon, J. J. 1984, ApJ, 287, 461

Connelley, M. S., Reipurth, B., & Tokunaga, A. T. 2008, AJ, 135, 2526

—. 2009, AJ, 138, 1193

Cox, E. G., Harris, R. J., Looney, L. W., et al. 2015, ApJ, 814, L28

Curiel, S., Rodriguez, L. F., Bohigas, J., et al. 1989, Astrophysical Letters and Communications, 27, 299

Curiel, S., Rodriguez, L. F., Moran, J. M., & Canto, J. 1993, ApJ, 415, 191

Davis, C. J., Scholz, P., Lucas, P., Smith, M. D., & Adamson, A. 2008, MNRAS, 387, 954

Draine, B. T., & Lee, H. M. 1984, ApJ, 285, 89

Duchêne, G., Bontemps, S., Bouvier, J., et al. 2007, A&A, 476, 229

Duchêne, G., & Kraus, A. 2013, ARA&A, 51, 269

Dulk, G. A. 1985, ARA&A, 23, 169

Dunham, M. M., Stutz, A. M., Allen, L. E., et al. 2014, Protostars and Planets VI, 195

Dunham, M. M., Allen, L. E., Evans, II, N. J., et al. 2015, ApJS, 220, 11

Duquennoy, A., & Mayor, M. 1991, A&A, 248, 485

Enoch, M. L., Evans, N. J., Sargent, A. I., & Glenn, J. 2009, ApJ, 692, 973

Enoch, M. L., Lee, J.-E., Harvey, P., Dunham, M. M., & Schnee, S. 2010, ApJ, 722, L33

Evans, N. J., Dunham, M. M., Jørgensen, J. K., et al. 2009, ApJS, 181, 321

Fischer, D. A., & Marcy, G. W. 1992, ApJ, 396, 178

Gerin, M., Pety, J., Fuente, A., et al. 2015, A&A, 577, L2

Ghavamian, P., & Hartigan, P. 1998, ApJ, 501, 687

Grossman, E. N., Masson, C. R., Sargent, A. I., et al. 1987, ApJ, 320, 356

Gutermuth, R. A., Myers, P. C., Megeath, S. T., et al. 2008, ApJ, 674, 336

Hirano, N., Ho, P. P. T., Liu, S.-Y., et al. 2010, ApJ, 717, 58

Hirano, N., Kamazaki, T., Mikami, H., Ohashi, N., & Umemoto, T. 1999, in Star Formation 1999, ed. T. Nakamoto, 181–182

Hirano, N., & Liu, F.-c. 2014, ApJ, 789, 50

Hirota, T., Honma, M., Imai, H., et al. 2011, PASJ, 63, 1

Hirota, T., Bushimata, T., Choi, Y. K., et al. 2008, PASJ, 60, 37

Hodapp, K. W., & Chini, R. 2014, ApJ, 794, 169

Hull, C. L. H., Plambeck, R. L., Kwon, W., et al. 2014, ApJS, 213, 13

Inutsuka, S.-I., & Miyama, S. M. 1992, ApJ, 388, 392

Jørgensen, J. K., Harvey, P. M., Evans, II, N. J., et al. 2006, ApJ, 645, 1246

Jørgensen, J. K., Bourke, T. L., Myers, P. C., et al. 2007, ApJ, 659, 479

Klahr, H. H., & Henning, T. 1997, Icarus, 128, 213

Köhler, R., Petr-Gotzens, M. G., McCaughrean, M. J., et al. 2006, A&A, 458, 461

Kratter, K. M., Matzner, C. D., Krumholz, M. R., & Klein, R. I. 2010, ApJ, 708, 1585

Kraus, A. L., & Hillenbrand, L. A. 2012, ApJ, 757, 141

Kraus, A. L., Ireland, M. J., Martinache, F., & Hillenbrand, L. A. 2011, ApJ, 731, 8

Kraus, A. L., Ireland, M. J., Martinache, F., & Lloyd, J. P. 2008, ApJ, 679, 762

Kwon, W., Looney, L. W., Crutcher, R. M., & Kirk, J. M. 2006, in astro-ph/0609176

Kwon, W., Looney, L. W., Mundy, L. G., Chiang, H.-F., & Kemball, A. J. 2009, ApJ, 696, 841

Lada, C. J. 1987, in IAU Symp. 115: Star Forming Regions, ed. M. Peimbert & J. Jugaku, 1–17

Lada, C. J. 2006, ApJ, 640, L63

Larson, R. B. 1995, MNRAS, 272, 213

Launhardt, R., Stutz, A. M., Schmiedeke, A., et al. 2013, A&A, 551, A98

Lay, O. P., Carlstrom, J. E., & Hills, R. E. 1995, ApJ, 452, L73

Lee, C., Hirano, N., Palau, A., et al. 2009, ApJ, 699, 1584

Lee, K. I., Dunham, M. M., Myers, P. C., et al. 2015, ApJ, 814, 114

Looney, L. W., Mundy, L. G., & Welch, W. J. 1997, ApJ, 484, L157+

—. 2000, ApJ, 529, 477

Machida, M. N., Tomisaka, K., Matsumoto, T., & Inutsuka, S. 2008, ApJ, 677, 327

Marks, M., & Kroupa, P. 2012, A&A, 543, A8

Mathieu, R. D. 1994, ARA&A, 32, 465

Matzner, C. D., & Levin, Y. 2005, ApJ, 628, 817

Maury, A. J., André, P., Hennebelle, P., et al. 2010, A&A, 512, A40

Maury, A. J., Belloche, A., André, P., et al. 2014, A&A, 563, L2

McKee, C. F., & Offner, S. S. R. 2010, ApJ, 716, 167

McMullin, J. P., Waters, B., Schiebel, D., Young, W., & Golap, K. 2007, in Astronomical Society of the Pacific Conference Series, Vol. 376, Astronomical Data Analysis Software and Systems XVI, ed. R. A. Shaw, F. Hill, & D. J. Bell, 127

Muzerolle, J., Furlan, E., Flaherty, K., Balog, Z., & Gutermuth, R. 2013, Nature, 493, 378

Myers, P. C., & Ladd, E. F. 1993, ApJ, 413, L47

Offner, S. S. R., & Arce, H. G. 2014, ApJ, 784, 61

Offner, S. S. R., Kratter, K. M., Matzner, C. D., Krumholz, M. R., & Klein, R. I. 2010, ApJ, 725, 1485

Offner, S. S. R., & McKee, C. F. 2011, ApJ, 736, 53

Öpik, E. 1924, Publications of the Tartu Astrofizica Observatory, 25, 1

Ossenkopf, V., & Henning, T. 1994, A&A, 291, 943

Padoan, P., & Nordlund, Å. 2002, ApJ, 576, 870

—. 2004, ApJ, 617, 559

Pech, G., Loinard, L., Chandler, C. J., et al. 2010, ApJ, 712, 1403

Pech, G., Zapata, L. A., Loinard, L., & Rodríguez, L. F. 2012, ApJ, 751, 78

Pezzuto, S., Elia, D., Schisano, E., et al. 2012, A&A, 547, A54

Pineda, J. E., Arce, H. G., Schnee, S., et al. 2011, ApJ, 743, 201

Pineda, J. E., Offner, S. S. R., Parker, R. J., et al. 2015, Nature, 518, 213

Plunkett, A. L., Arce, H. G., Corder, S. A., et al. 2013, ApJ, 774, 22

Rafikov, R. R. 2005, ApJ, 621, L69

Raghavan, D., McAlister, H. A., Henry, T. J., et al. 2010, ApJS, 190, 1

Reipurth, B., & Clarke, C. 2001, AJ, 122, 432

Reipurth, B., Clarke, C. J., Boss, A. P., et al. 2014, ArXiv e-prints, arXiv:1403.1907

Reipurth, B., Guimarães, M. M., Connelley, M. S., & Bally, J. 2007, AJ, 134, 2272

Reipurth, B., & Mikkola, S. 2012, Nature, 492, 221

Reipurth, B., Mikkola, S., Connelley, M., & Valtonen, M. 2010, ApJ, 725, L56

Reipurth, B., Rodríguez, L. F., Anglada, G., & Bally, J. 2002, AJ, 124, 1045

—. 2004, AJ, 127, 1736

Rodríguez, L. F., Anglada, G., & Curiel, S. 1997, ApJ, 480, L125

—. 1999, ApJS, 125, 427

Rodriguez, L. F., Curiel, S., Moran, J. M., et al. 1989, ApJ, 346, L85

Rodríguez, L. F., Delgado-Arellano, V. G., Gómez, Y., et al. 2000, AJ, 119, 882

Rodriguez, L. F., Ho, P. T. P., Torrelles, J. M., Curiel, S., & Canto, J. 1990, ApJ, 352, 645

Rodriguez, L. F., Marti, J., Canto, J., Moran, J. M., & Curiel, S. 1993, Rev. Mexicana Astron. Astrofis., 25, 23

Rodríguez, L. F., Reipurth, B., Raga, A. C., & Cantó, J. 1998, Rev. Mexicana Astron. Astrofis., 34, 69

Rodríguez, L. F., Zapata, L. A., & Palau, A. 2014, ApJ, 790, 80

Sadavoy, S. I., Di Francesco, J., André, P., et al. 2014, ApJ, 787, L18

Sana, H., & Evans, C. J. 2011, in IAU Symposium, Vol. 272, IAU Symposium, ed. C. Neiner, G. Wade, G. Meynet, & G. Peters, 474–485

Sandell, G., Knee, L. B. G., Aspin, C., Robson, I. E., & Russell, A. P. G. 1994, A&A, 285, L1

Schnee, S., Sadavoy, S., Di Francesco, J., Johnstone, D., & Wei, L. 2012, ApJ, 755, 178

Scholz, F. W., & Stephens, M. A. 1987, Journal of the American Statistical Association, 82, 918

Seale, J. P., & Looney, L. W. 2008, ApJ, 675, 427

Simon, M., Dutrey, A., & Guilloteau, S. 2000, ApJ, 545, 1034

Stamatellos, D., & Whitworth, A. P. 2009, MNRAS, 392, 413

Strom, S. E., Vrba, F. J., & Strom, K. M. 1976, AJ, 81, 314

Stutz, A. M., Tobin, J. J., Stanke, T., et al. 2013, ApJ, 767, 36

Takakuwa, S., Saito, M., Lim, J., et al. 2012, ApJ, 754, 52

Terebey, S., & Padgett, D. L. 1997, in IAU Symp. 182: Herbig-Haro Flows and the Birth of Stars, ed. B. Reipurth & C. Bertout, 507–514

Testi, L., Birnstiel, T., Ricci, L., et al. 2014, Protostars and Planets VI, 339

Tobin, J. J., Hartmann, L., Looney, L. W., & Chiang, H. 2010, ApJ, 712, 1010

Tobin, J. J., Looney, L. W., Mundy, L. G., Kwon, W., & Hamidouche, M. 2007, ApJ, 659, 1404

Tobin, J. J., Hartmann, L., Chiang, H.-F., et al. 2011, ApJ, 740, 45

Tobin, J. J., Bergin, E. A., Hartmann, L., et al. 2013, ApJ, 765, 18

Tobin, J. J., Looney, L. W., Wilner, D. J., et al. 2015a, ApJ, 805, 125

Tobin, J. J., Dunham, M. M., Looney, L. W., et al. 2015b, ApJ, 798, 61

Tohline, J. E. 2002, ARA&A, 40, 349

Tokuda, K., Onishi, T., Saigo, K., et al. 2014, ApJ, 789, L4

van der Marel, N., Pinilla, P., Tobin, J., et al. 2015, ApJ, 810, L7

Vorobyov, E. I., & Basu, S. 2006, ApJ, 650, 956

—. 2010, ApJ, 719, 1896

Walch, S., Naab, T., Whitworth, A., Burkert, A., & Gritschneder, M. 2010, MNRAS, 402, 2253

Werner, M. W., Roellig, T. L., Low, F. J., et al. 2004, ApJS, 154, 1

White, R. J., & Ghez, A. M. 2001, ApJ, 556, 265

Wootten, A. 1989, ApJ, 337, 858

Yen, H.-W., Koch, P. M., Takakuwa, S., et al. 2015, ApJ, 799, 193

Young, C. H., Jørgensen, J. K., Shirley, Y. L., et al. 2004, ApJS, 154, 396

Young, K. E., Young, C. H., Lai, S.-P., Dunham, M. M., & Evans, II, N. J. 2015, ArXiv e-prints, arXiv:1505.08122

Zhao, B., & Li, Z.-Y. 2013, ApJ, 763, 7

Zhu, Z., Hartmann, L., Nelson, R. P., & Gammie, C. F. 2012, ApJ, 746, 110

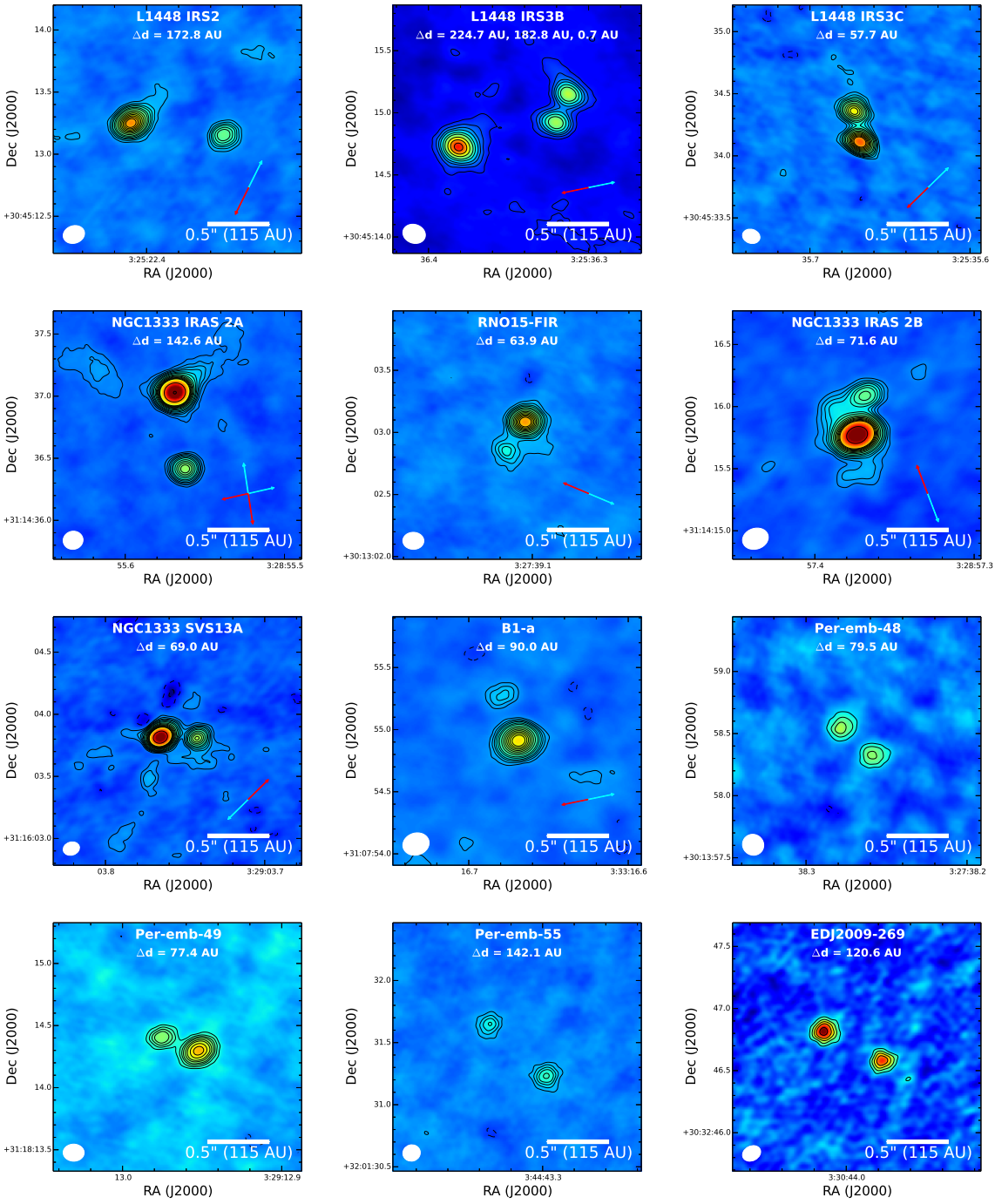

Fig. 1.— Images of multiple systems with separations < 500 AU. The images are produced from the combined A and B configuration data. Natural weighting is used, along with the full Ka-band bandwidth (9 mm effective wavelength; SVS13A uses Briggs weighting with robust=0.5). The outflow directions (where available) are indicated by blue and red arrows in the lower right corner. The outflows are assumed to be driven by the brightest source; the only source with a definitive second outflow is NGC 1333 IRAS2A (Tobin et al. 2015b). The contours are [-6,-3, 3, 5, 7, 9, 12, 15, 20, 25, 30, 35, 40, 45, 50, 100, 200, 300, 400, 500, 600] × σ. White circles are drawn around low S/N companions that are verified at other wavelengths, see Section 4.1.

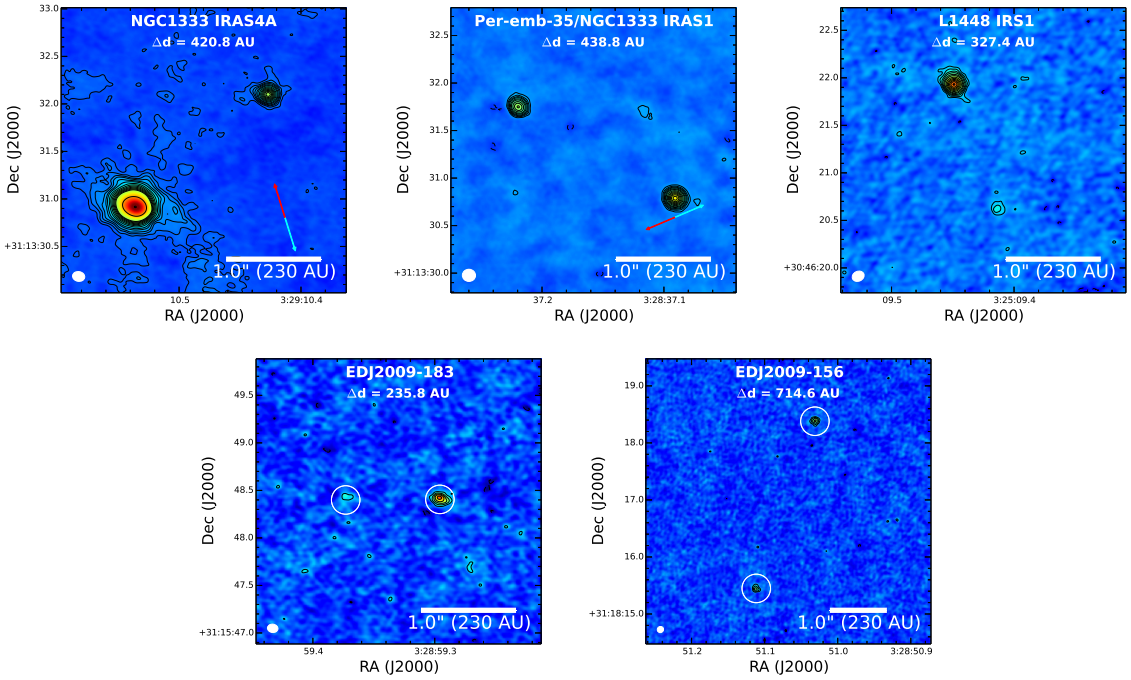
NGC1333 IRAS4A
Δd = 420.8 AU
Per-emb-35/NGC1333 IRAS1
Δd = 438.8 AU
L1448 IRS1
Δd = 327.4 AU
EDJ2009-183
Δd = 235.8 AU
EDJ2009-156
Δd = 714.6 AU
1.0" (230 AU)
Dec (J2000)
RA (J2000)

Fig. 1b.—

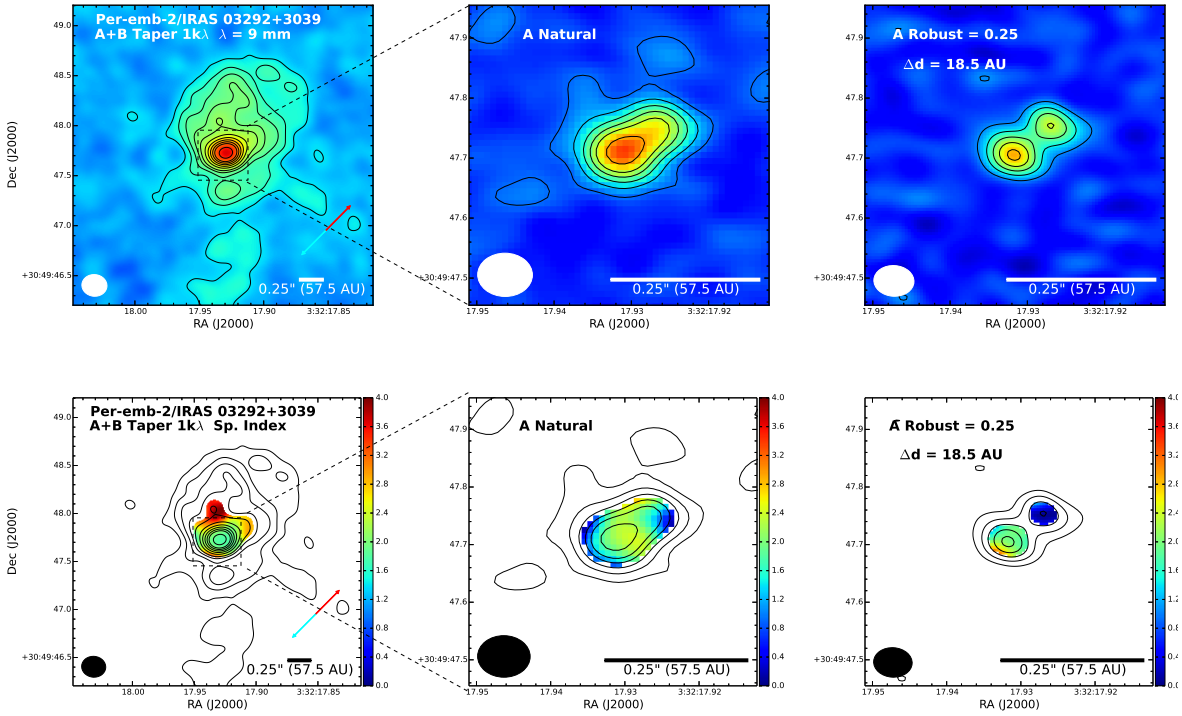

Fig. 2.— Images of Per-emb-2 (IRAS 03292+3039) at 9 mm (top) and the 8 mm to 1 cm spectral index map (bottom) at increasing resolution from left to right. The left panels with the lowest resolution and most sensitivity to extended structure show significant, structured emission surrounding a bright source that we interpret as the position of the main protostar; the middle and right panels zoom-in on the region outlined with a dashed box. The middle panels with higher resolution have resolved-out the extended structure and only detect the bright peak at the position of the protostar; however, the source appears extended at this resolution. The highest resolution images in the right panels show that the source is resolved into two sources separated by 18.5 AU. The contours in each panel are [-6, -3, 3, 6, 9, 12, 15, 20, 25, 30, 35, 40, 50, 60, 70, 80, 90, 100, 150] $\times$ σ, where σ = 7.3 μJy, 9.6 μJy, 11.9 μJy from left to right at 9 mm. The spectral index maps are only drawn in regions where the S/N $>$ 10.

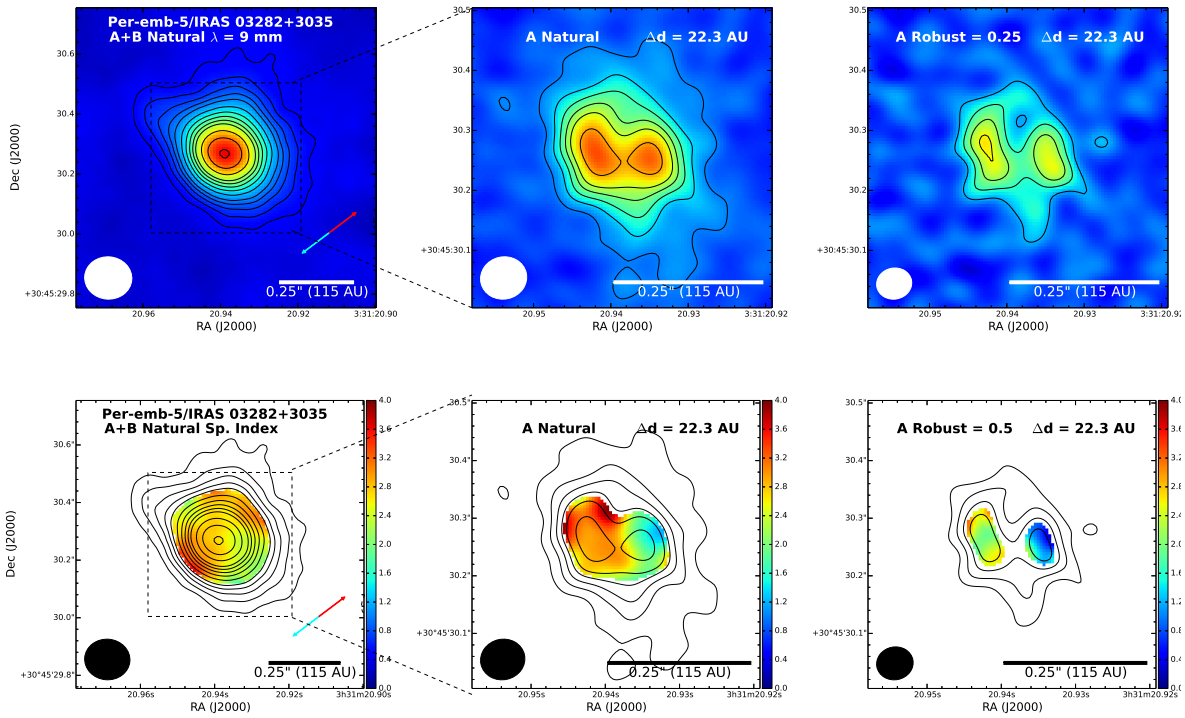

Fig. 3.— Images of Per-emb-5 (IRAS 03282+3035) at 9 mm (top) and the 8 mm to 1 cm spectral index map (bottom) at increasing resolution from left to right. The left panels with the lowest resolution show marginally-resolved emission, but the middle panels with higher resolution show that this source breaks into a double-peaked structure at higher resolution. The highest resolution images in the right panels show that the eastern peak is elongated in the north-south direction; the two sources are separated by 22.3 AU. The contours in each panel are [-6, -3, 3, 6, 9, 12, 15, 20, 25, 30, 35, 40, 50, 60, 70, 80, 90, 100, 150] $\times$ σ, where σ = 6.35 μJy, 8.4 μJy, 9.3 μJy from left to right at 9 mm. The spectral index maps are only drawn in regions where the S/N $>$ 10.

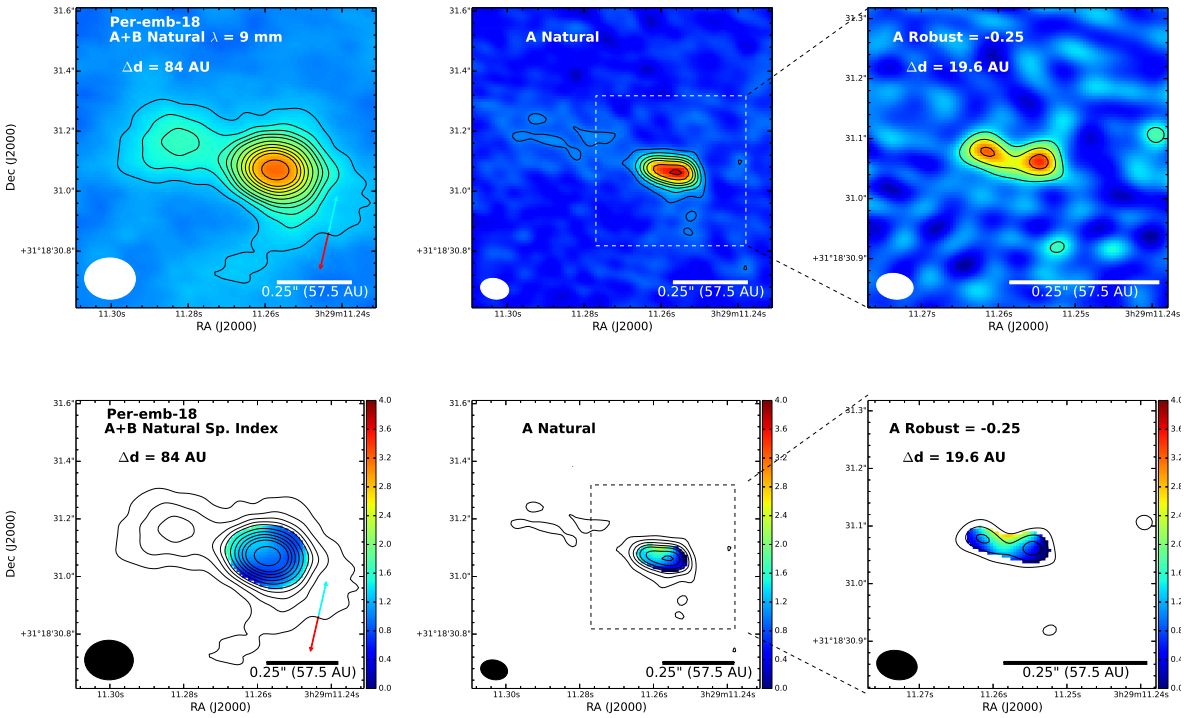

Fig. 4.— Images of Per-emb-18 (NGC 1333 IRAS7) at 9 mm (top) and the 8 mm to 1 cm spectral index map (bottom) at increasing resolution from left to right. The left panels with the lowest resolution show double-peaked emission with the eastern source being significantly fainter than the western source. Higher resolution data are shown in the middle panels and the eastern source is now absent, indicating that it has been resolved-out at higher resolution. However, the western source is resolved at this scale. The highest-resolution view is shown in the right panels as a zoom-in on the dashed-box shown in the middle panel toward the western source. At 9 mm the source is clearly double-peaked, separated by 19.6 AU. The contours in each panel are [-6, -3, 3, 6, 9, 12, 15, 20, 25, 30, 35, 40, 50, 60, 70, 80, 90, 100, 150] $\times$ σ, where σ = 6.56 μJy, 8.8 μJy, 9.8 μJy from left to right at 9 mm. The spectral index maps are only drawn in regions where the S/N $>$ 10.

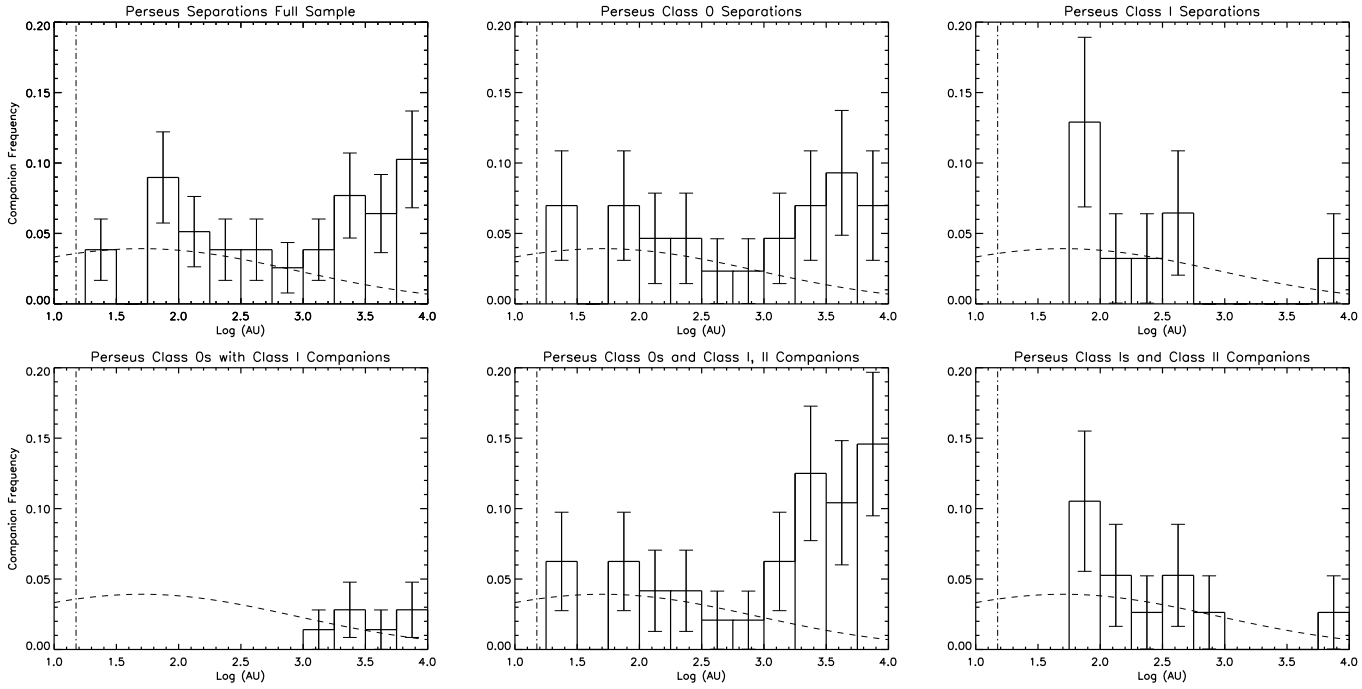

Fig. 5.— Histograms of companion frequency versus separation for multiple sources in Perseus. The top left panel shows the distribution for all sources in the sample; the top middle and top right panels break the distribution into sources that are only comprised of Class 0 protostars and Class I protostars, respectively. The bottom left panel shows only the multiple systems comprised of Class 0 and I sources, the bottom middle shows the separation distribution of all systems with a Class 0 primary source and the bottom left panel shows the same, but with a Class I primary. The systems comprised of a Class 0 and Class I protostar are not included in the Class I plot in the bottom right. Note the apparent bi-modal distribution for the full sample and Class 0 samples and the apparent deficit of wide companions for the Class I systems. In all plots, the dashed curve is the Gaussian fit to the field star separation distribution from Raghavan et al. (2010) and the vertical dot-dashed line corresponds to the approximate resolution limit of 15 AU.

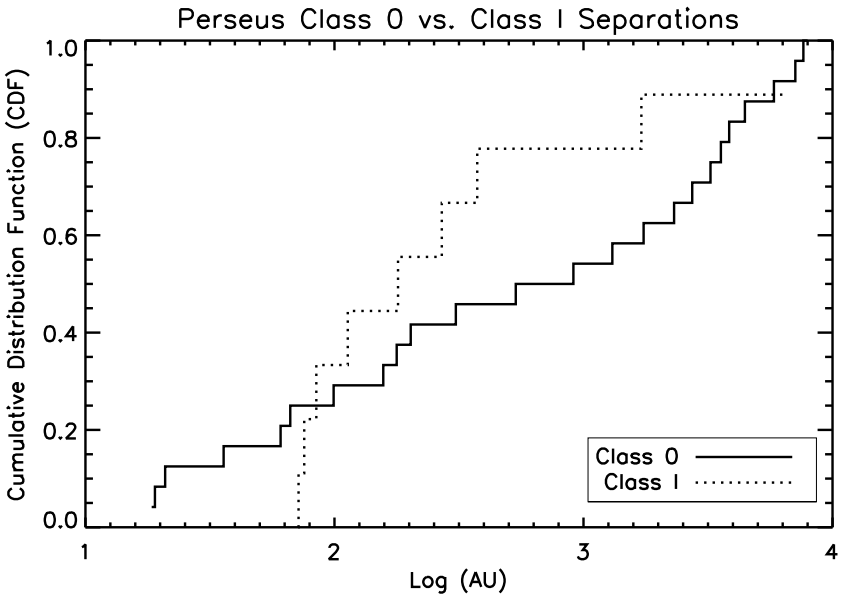

Fig. 6.— Cumulative distribution function versus separation for the Class 0 and Class I protostars. There is a large difference between the two functions and the results from the Anderson-Darling (AD) test on the two samples indicates a probability of only 0.17 that they are drawn from the same distribution. The Class I sources have substantially fewer wide companions relative to the Class 0s (also see Figure 5), this may be indicative of wide companions either migrating inward or moving apart as sources evolve to the Class I phase. The Class 0 sources with wide Class I or Class II companions are not included in either of the cumulative distributions.

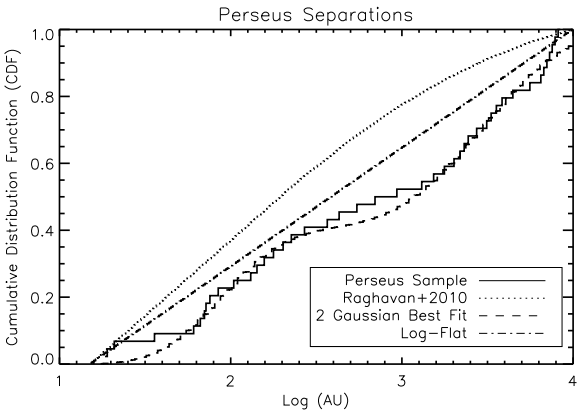

Fig. 7.— Cumulative distribution function of the full sample of Perseus multiples compared to different empirical and observed separation distributions. The comparisons shown are for a log-flat distribution, the Raghavan et al. (2010) distribution, and a distribution defined by 2 Gaussians. The AD test probabilities for the log-flat distribution and the Raghavan et al. (2010) distribution are 0.08 and 0.00009 respectively, meaning that the Perseus separations are most likely not drawn from either of these distributions. Two Gaussians fit the data well, but the parameters of the second Gaussian at large separations are poorly constrained.

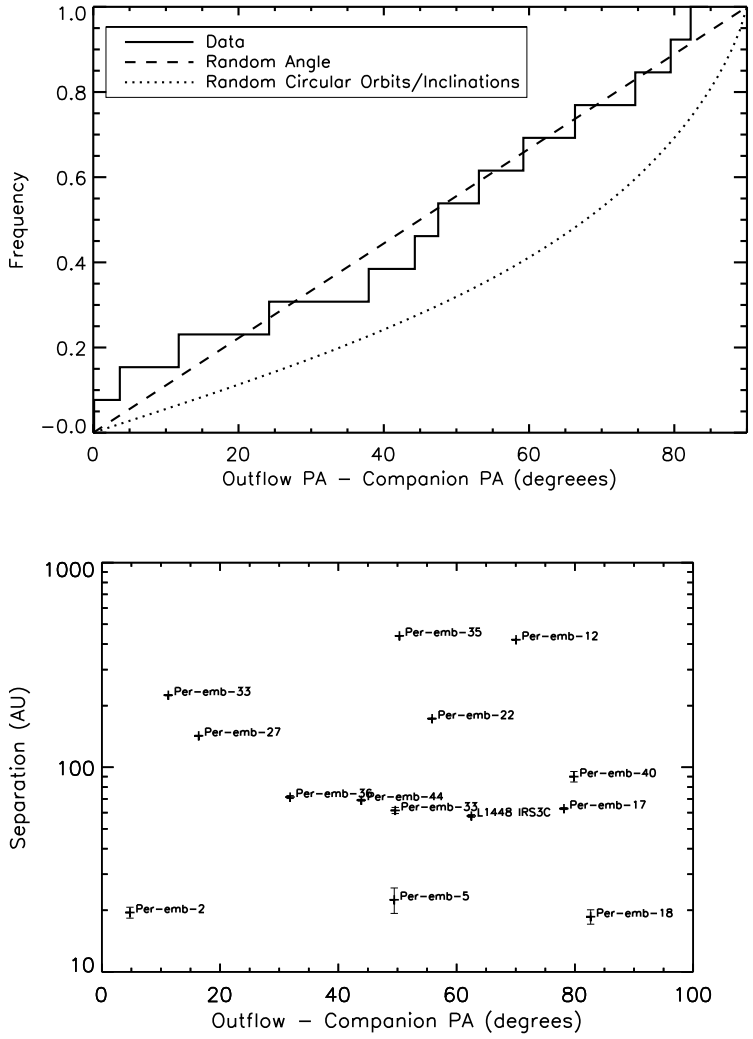

Fig. 8.— Cumulative distribution of companion position angles relative to outflow position angles (top panel) for Class 0 and Class I sources with separations < 500 AU and known outflow position angles. The bottom panel shows a plot of separation versus companion position angles relative to outflow position angles. In the top panel, the solid line shows the data, the dashed line shows a random distribution of relative position angles, and the dotted line shows the distribution for position angles for companions at a random phase in a circular orbit projected with a uniform distribution of inclinations. The position angles, as measured on-sky, appear to be consistent with random. The observations have a clear excess of companions at position angles $< 40°$ relative to the expectation for random orientations and inclinations. However, the bottom plot shows that there is no apparent correlation with relative position angle and separation; the apparent excess may be due to small number statistics. The outflow position angles are given in Table 7.

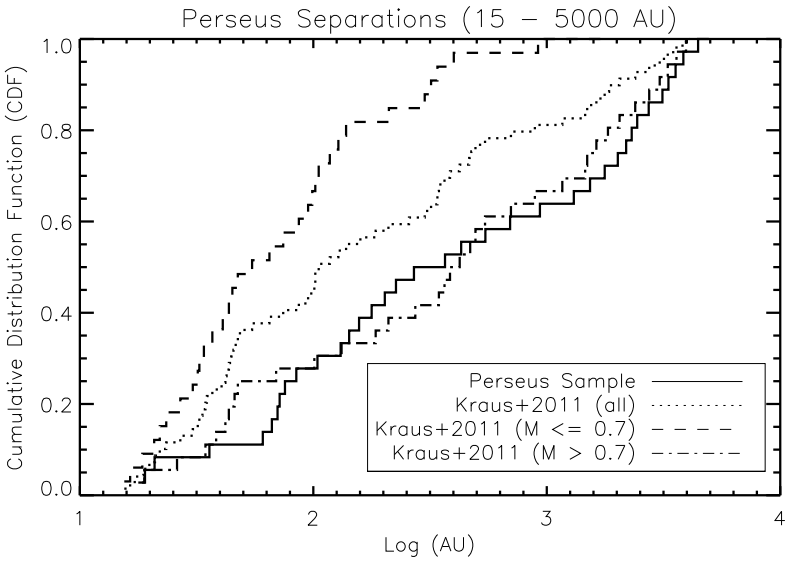

Fig. 9.— Comparison of the Perseus multiples to the more-evolved multiple stars in Taurus from Kraus et al. (2011). The whole Taurus sample and low-mass Taurus sub-sample are in disagreement with the Perseus results, while the high-mass Taurus sub-sample is reasonably consistent with the Perseus sample. The AD test results of the Taurus samples relative to Perseus indicate probabilities of being drawn from the same distribution of 0.015, 0.00008, and 0.86 for the full sample, low-mass, and high-mass samples, respectively.

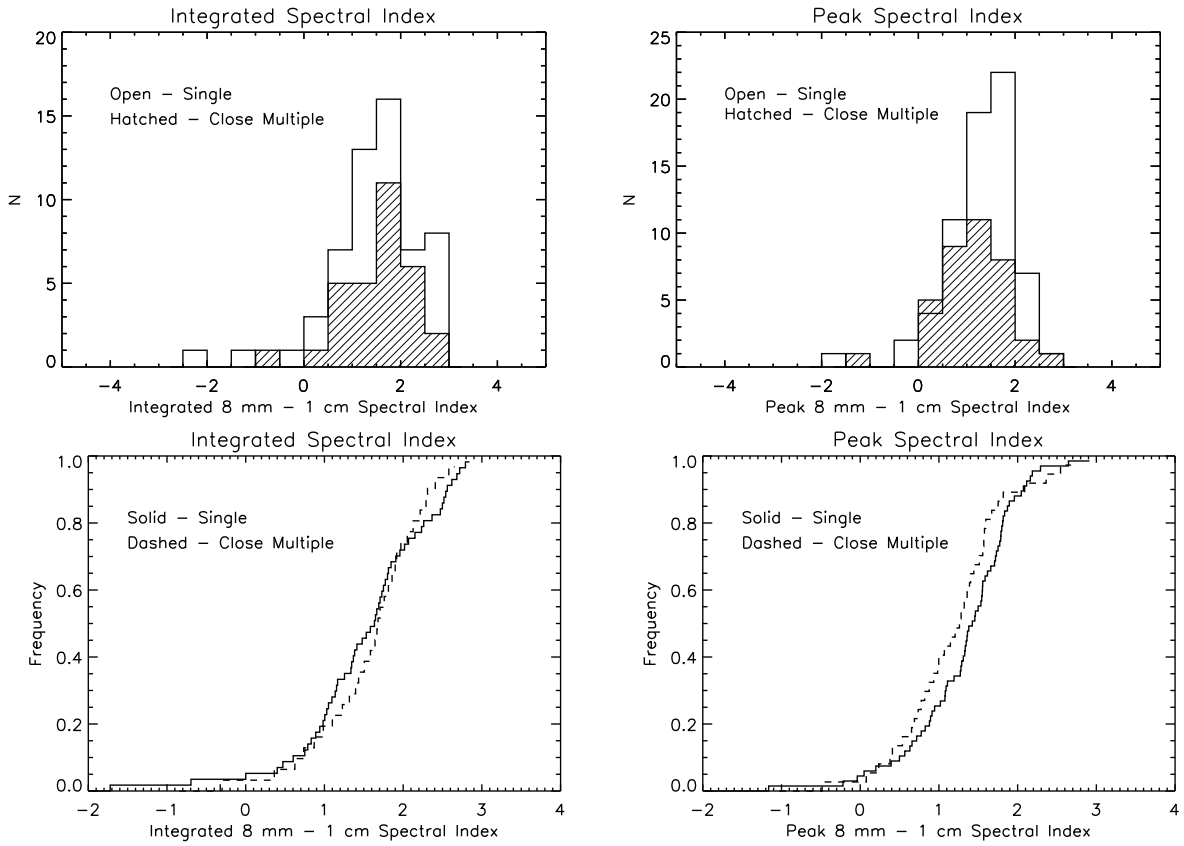

Fig. 10.— Distributions of spectral indices for the single and multiple sources. The distributions only include sources that have spectral index error less than 0.9. The histograms of the peak and integrated spectral index are quite comparable for the single and multiple sources. The cumulative distributions also show close correspondence of the two samples. Running the AD test on the distributions of integrated and peak spectral indices yield probabilities of 0.7 and 0.35, respectively, indicating that the distributions for single and multiple sources are most likely drawn from the same sample. Thus, the emission properties of single and multiple sources are statistically indistinguishable.

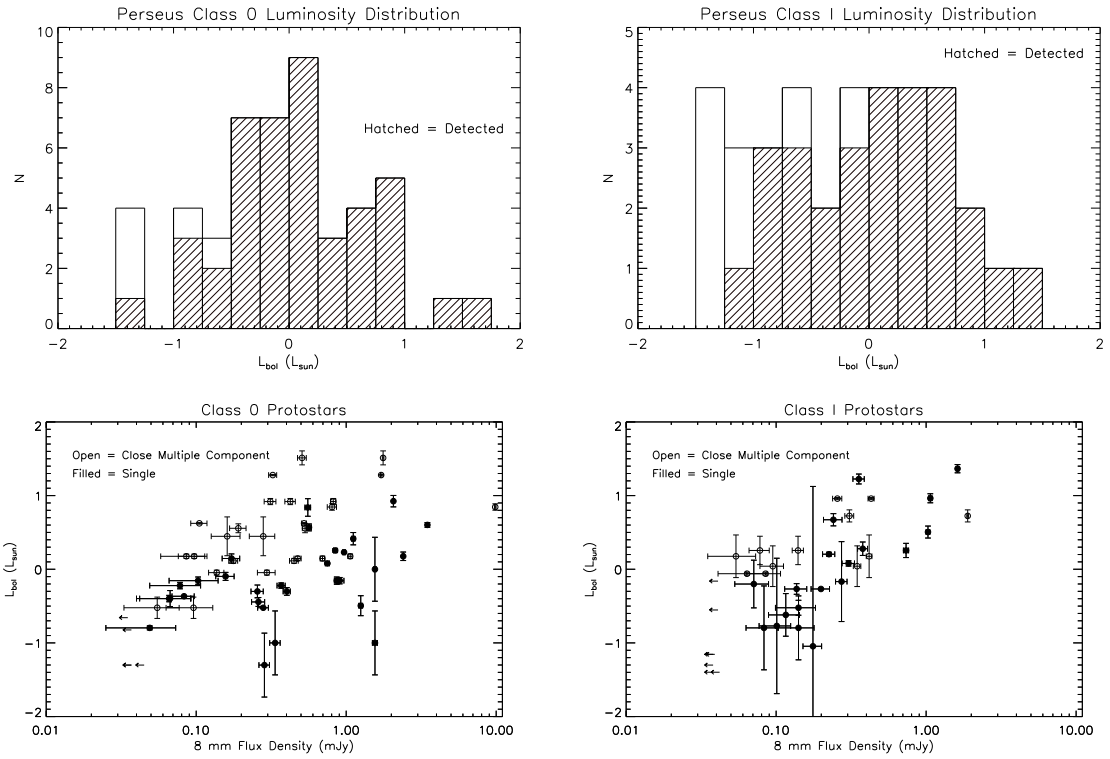

Fig. 11.— The bolometric luminosity distributions of the Class 0 and Class I samples are shown in the top left and top right panels, respectively. The hatched regions show the histogram for sources that were detected in the VLA survey; we detect nearly all of the Class 0 and Class I samples except for mainly a few low-luminosity sources. In the case of the Class 0 sample, most of these low-luminosity sources are comprised of candidate first hydrostatic cores. The distribution of 8 mm flux densities as a function of bolometric luminosity are then shown in the bottom left and bottom right panels, respectively. The components of multiple systems are drawn as open circles and the single sources are filled circles. There is an apparent weak correlation between 8 mm flux density and bolometric luminosity, but there is significant scatter. The Class I sources show a more clear relationship since there are no low-luminosity sources with large 8 mm flux densities.

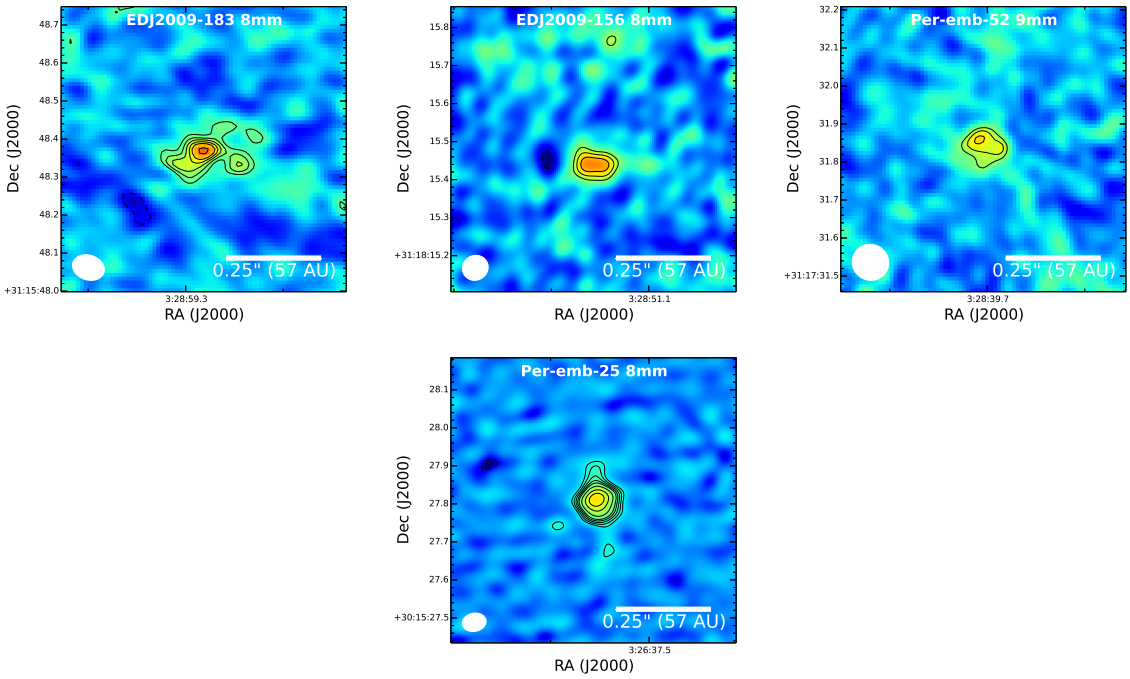

Fig. 12.— Images of resolved structures that are not significant enough to be classified as companions. The contours in these images start at 3σ and increase in 1σ intervals; σ= 11.5 μJy, 17.4μJy, 11.0 μJy, 14.1 μJy and 14.5 μJy for EDJ2009-156, EDJ2009-183, Per-emb-52, and Per-emb-25, respectively. Images are from combined A and B-configuration images, except for EDJ2009-156 and EDJ2009-183 where they are A-configuration data only.

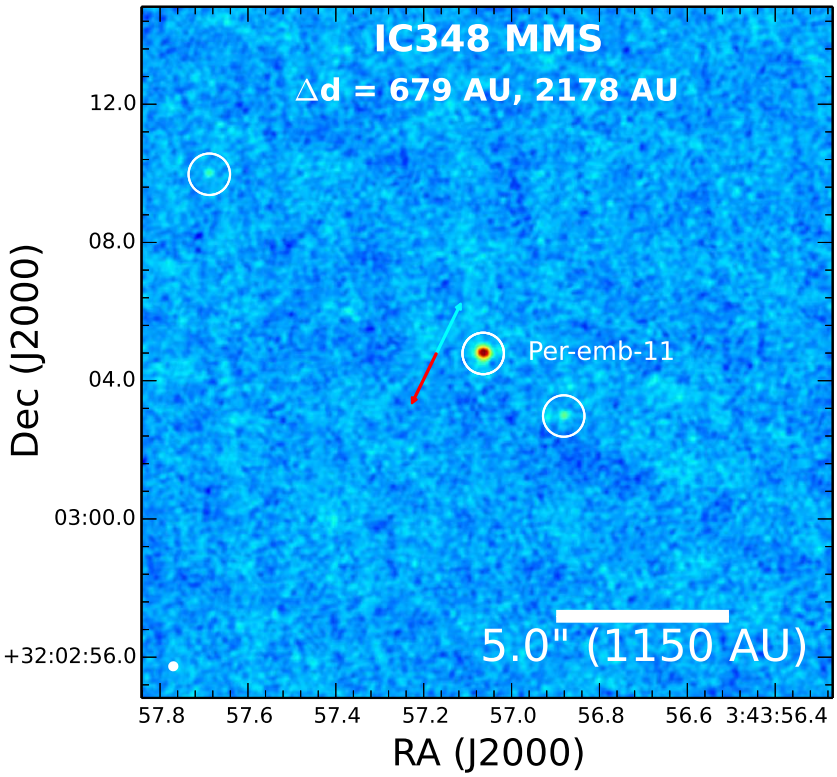

Fig. 13.— Image of the wide multiple system toward IC348 MMS (Per-emb-11). The image is a B configuration image of the region and three sources are detected. IC348 MMS1/Per-emb-11-A is the brightest source in the middle, JVLA3a from Rodríguez et al. (2014) is 2.″95 southwest and IC348 MMS2 (Per-emb-11-C) is separated by 9.″47. White circles are drawn around the companion sources. Separations written inside the figure are relative to Per-emb-11 at the center. The blue and red arrows drawn near sources denote the blue and red-shifted direction of the outflows when known.

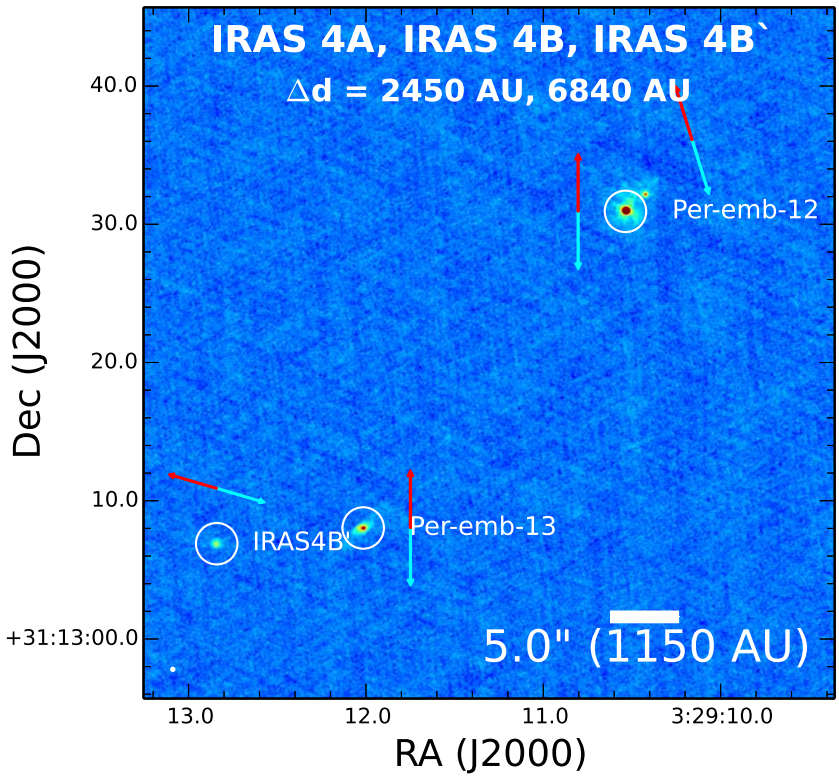

Fig. 14.— B configuration image of NGC 1333 IRAS4A/Per-emb-12, NGC 1333 IRAS 4B/Per-emb-13, and NGC 1333 IRAS4B' (IRAS4B' was also called IRAS4C by Looney et al. 2000). Both sources appear resolved in the images, with IRAS4B being extended to the east. The blue and red arrows drawn near sources denote the blue and red-shifted direction of the outflows when known.

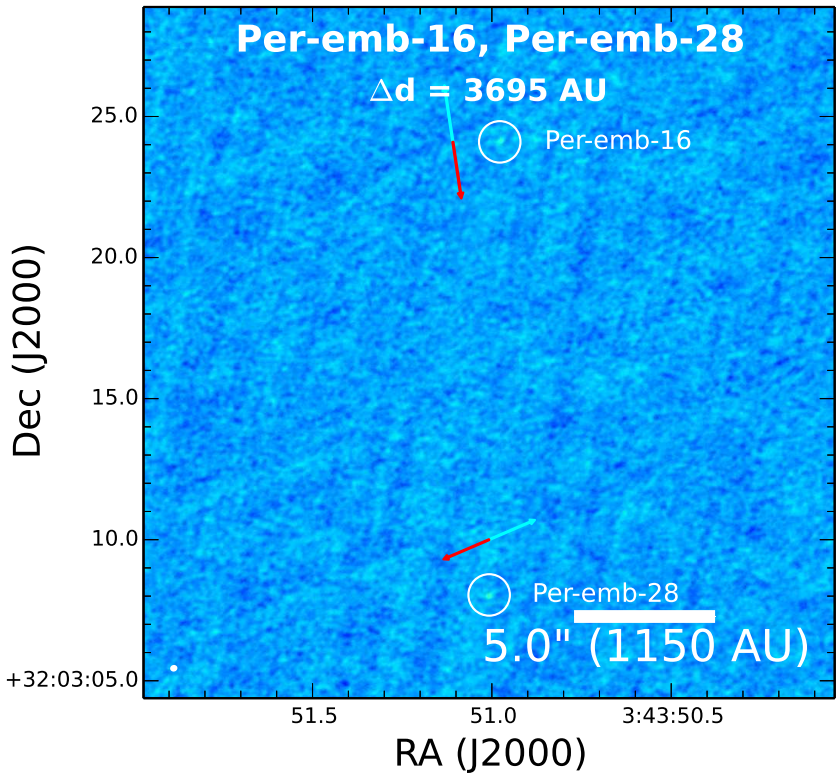

Fig. 15.— A+B configuration image of Per-emb-16 and Per-emb-28, forming a wide multiple system. Per-emb-28 is also known as LRLL 54361 and has been shown to exhibit strong variability by Muzerolle et al. (2013). The blue and red arrows drawn near sources denote the blue and red-shifted direction of the outflows. The position angle of the outflow from Per-emb-16 is approximately in the north-south direction Yen et al. (2015) and the outflow direction of Per-emb-28 is about 60° different with a position angle of ∼300° (Muzerolle et al. 2013).

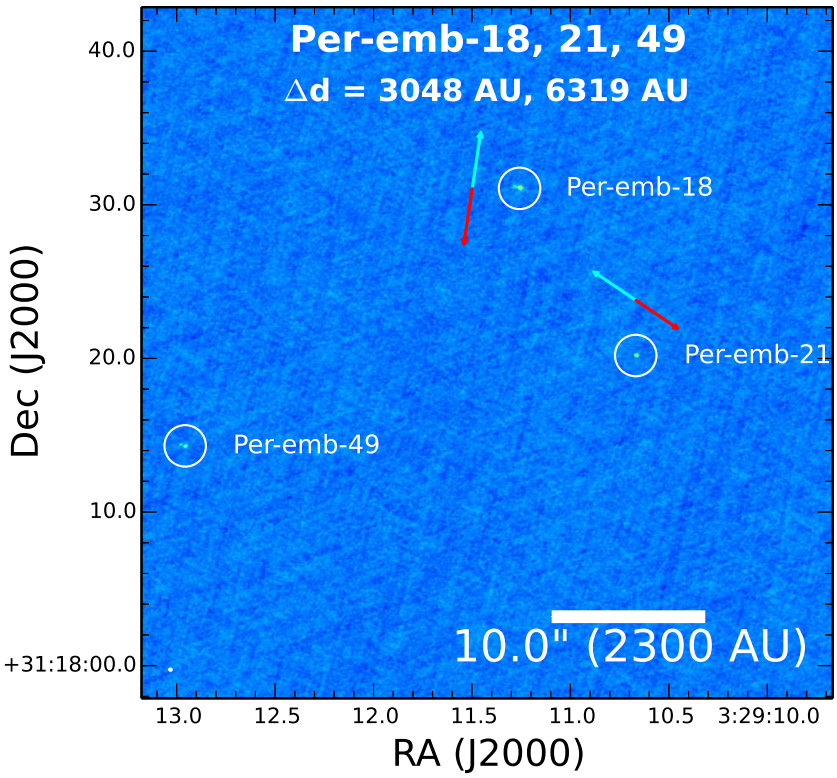

Fig. 16.— Wide view of the NGC 1333 IRAS7 system in a 9 mm A+B configuration image. Both Per-emb-18 and Per-emb-49 are multiples with separations less than 100 AU and Per-emb-21 is single to the limit of our resolution. The blue and red arrows drawn near sources denote the blue and red-shifted direction of the outflows when known. The outflow direction of Per-emb-18 is approximately north-south, a position angle of ∼159° is estimated from H_2 knots (Davis et al. 2008). The outflow of Per-emb-21 is oriented approximately orthogonal to that of Per-emb-18 with a position angle of 48°. Note that Per-emb-18 = YSO23 and Per-emb-21 = YSO24 from Davis et al. (2008). The outflow position angle for Per-emb-49 is currently unknown. Separations written inside the figure are relative to Per-emb-18.

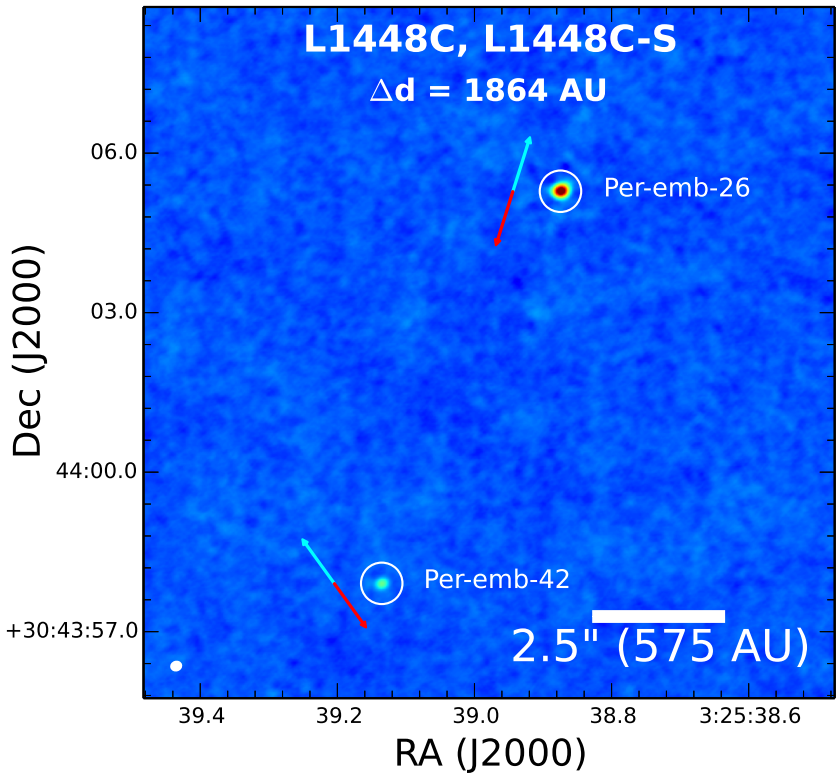

Fig. 17.— Image of the region around L1448C/Per-emb-26, also known as L1448-mm. Per-emb-42 was referred to as L1448C-S in Jørgensen et al. (2006) where the source is detected by *Spitzer* with IRAC and MIPS (see also Tobin et al. 2007). Both sources are found to drive an outflow. The blue and red arrows drawn near sources denote the blue and red-shifted direction of the outflows. The outflow from Per-emb-42 oriented with a position angle of 40° relative to the ∼340° position angle of Per-emb-26 (Hirano et al. 2010).

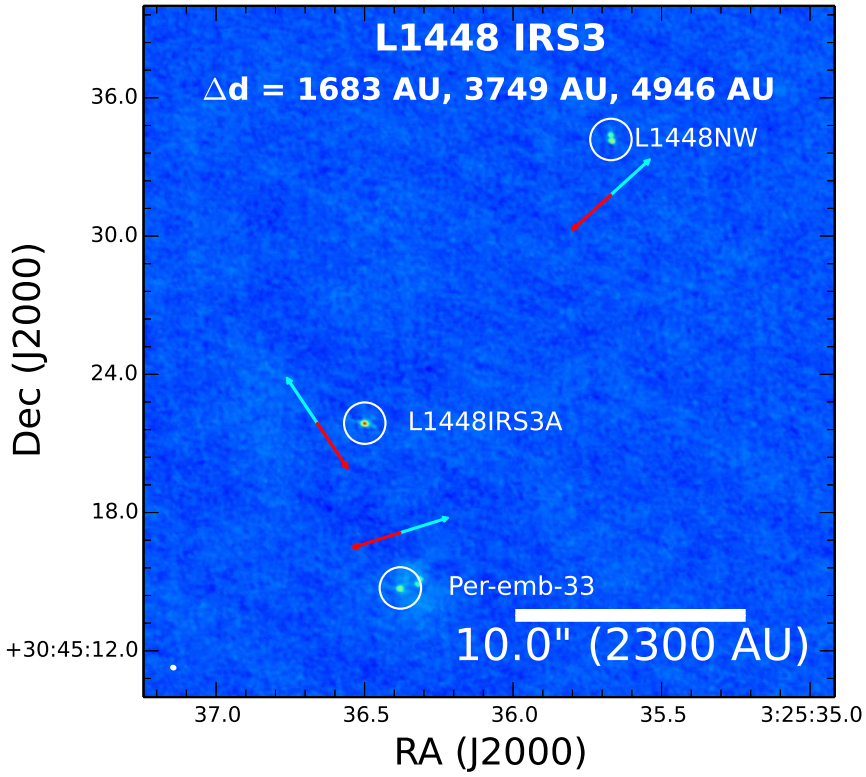

Fig. 18.— Image of the L1448-N or IRS3 region; Per-emb-33 corresponds to L1448 IRS3B. Both Per-emb-33 and L1448NW (L1448 IRS3C) are Class 0 sources and multiple systems with separations less than 200 AU; L1448 IRS3A is single at the limit of our resolution. The blue and red arrows drawn near sources given the blue and red-shifted direction of the outflows when known. The position angle of the outflow from Per-emb-33 is ∼275° and the outflow from L1448NW has a position angle of ∼330°. The outflow from L1448 IRS3A is uncertain (Tobin et al. 2015a), but may have a position angle of ∼30° (Lee et al. 2015). Separations written inside the figure are relative to Per-emb-33.

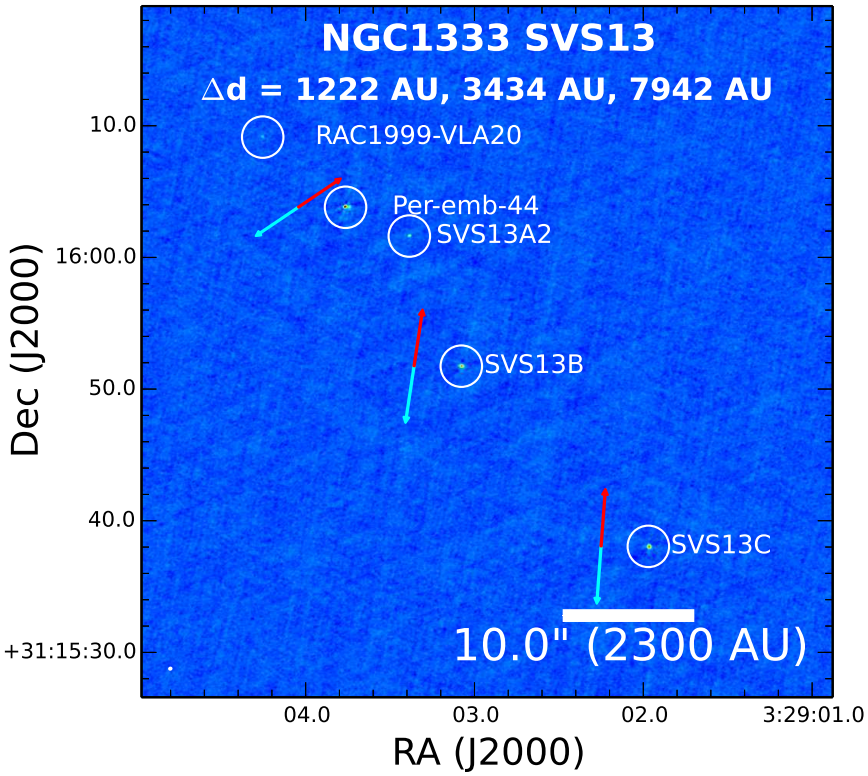

Fig. 19.— NGC 1333 SVS13 region. Per-emb-44 corresponds to SVS13A and the close companion to Per-emb-44 was first discovered by Anglada et al. (2000) with the VLA at 3.6 cm (VLA4) and later at 7 mm (Anglada et al. 2004). SVS13A2 was discovered at 3.6 cm by Rodríguez et al. (1997) and was referred to as VLA3. Thus far, outflows have only been conclusively detected toward Per-emb-44 with a position angle of 120° (Plunkett et al. 2013) and SVS13B with a position angle of ∼160° (Bachiller et al. 1998, 2000). SVS13C has a candidate outflow position angle of ∼8° (Plunkett et al. 2013). Separations written inside the figure are relative to Per-emb-44. The blue and red arrows drawn near sources given the blue and red-shifted direction of the known outflows.

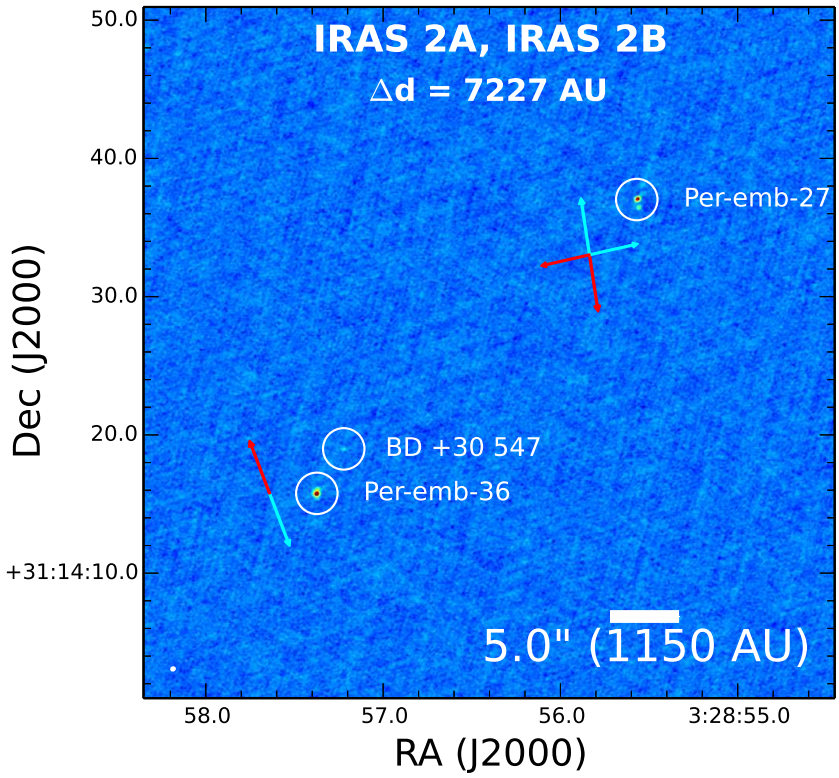

Fig. 20.— NGC 1333 IRAS2 at 9 mm in A+B configuration. IRAS 2B is ∼7225 AU east of IRAS 2A and is most likely a Class I protostar. The faint source northwest of IRAS2B is an optically-visible star (BD +30 547) that appears to be illuminating the near side of the molecular cloud. We do not believe that it is physically associated with IRAS2B itself. The blue and red arrows drawn near sources given the blue and red-shifted direction of the outflows identified by Plunkett et al. (2013).

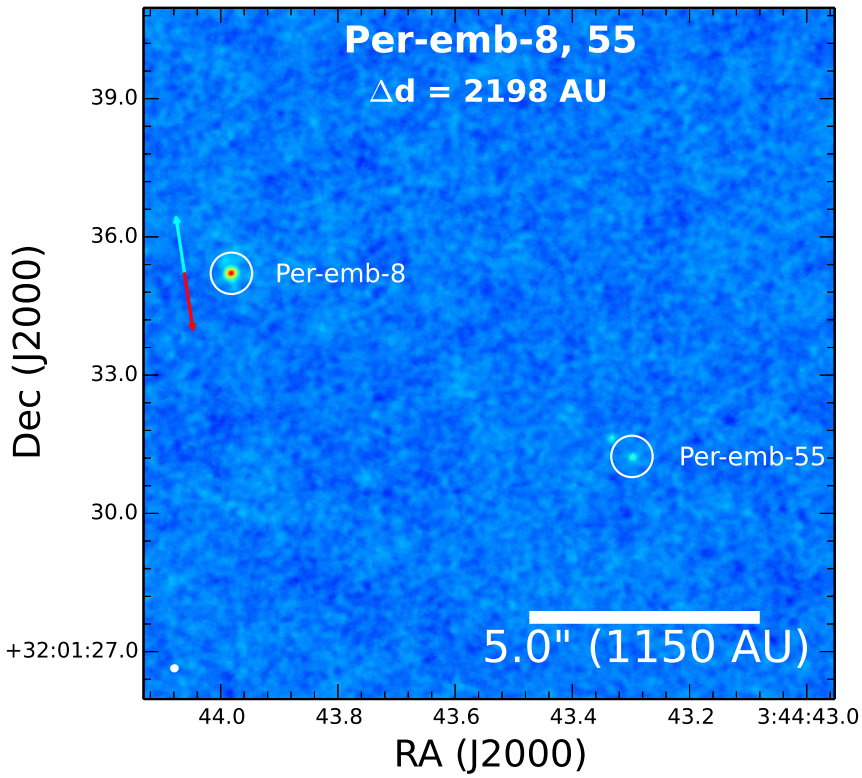

Fig. 21.— Image of Per-emb-8 and Per-emb-55 at 9 mm in A+B configuration. Per-emb-8 is a Class 0 protostar, while Per-emb-55 is a Class I protostar with a close companion (Figure 1) and much brighter at IRAC wavelengths (Jørgensen et al. 2006). The relative outflow directions from these sources are unknown, but we estimate that Per-emb-8 has a position angle of ∼30° from the IRAC scattered light morphology (denoted by red and blue arrows).

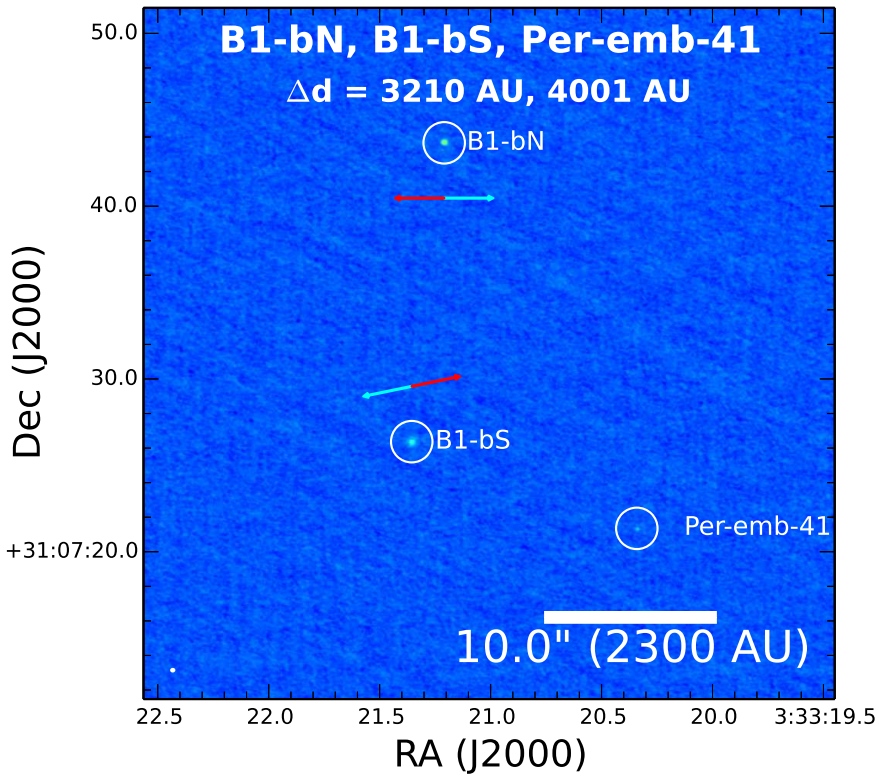

Fig. 22.— B1-b region in A+B configuration at 9 mm. Both B1-bN and B1-bS are deeply embedded systems and candidate FHSC objects, while Per-emb-41 is a Class I object. Hirano & Liu (2014) suggests that all three sources are driving misaligned outflows, but their directions are difficult to discern. Gerin et al. (2015) finds that the B1-bN and B1-bS are both driving outflows in the east-west directions (blue and red arrows). Separations are with respect to B1-bS.

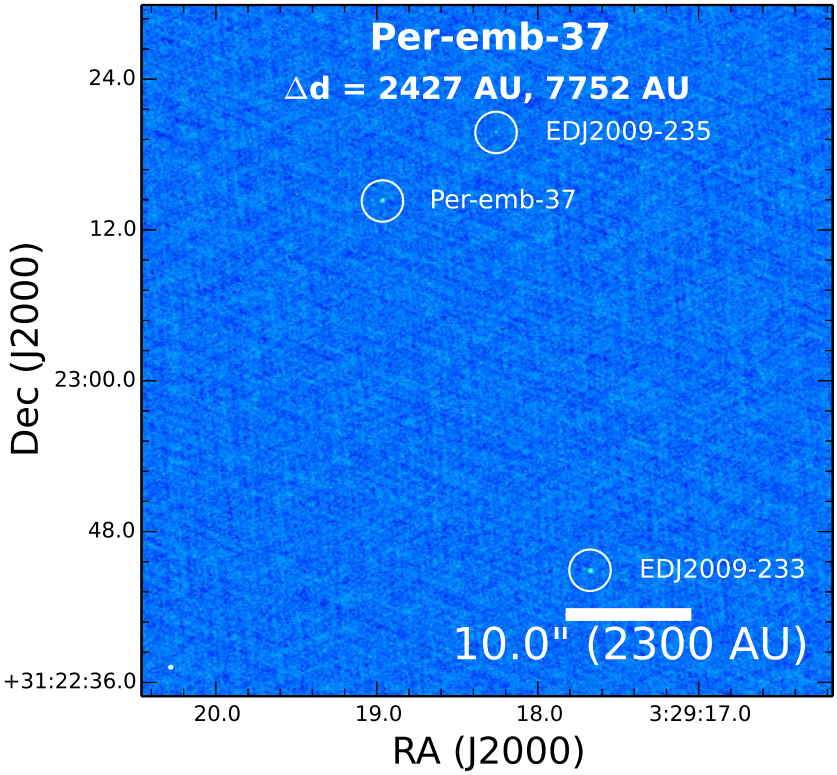

Fig. 23.— Image of the Per-emb-37 region at 9 mm in A+B configuration. Per-emb-37 was associated with a brighter infrared source located directly north by a few arcseconds in Enoch et al. (2009). However, *Herschel* imaging showed that the 70 μm peak emission was not coincident with the IRAC position, therefore Per-emb-37 must be a deeply embedded Class 0 system, perhaps similar to the PBRS in Orion (Stutz et al. 2013). The source originally associated with Per-emb-37 was not detected in our 9 mm data; however, we did detect two other sources associated with IRAC detections, but not *Herschel* 70 μm or 100 μm indicating that they may be more-evolved Class II sources. No outflow has currently been detected toward Per-emb-37. Separations are relative to Per-emb-37.

Table 1. Source List

Source	RA (J2000)	Dec (J2000)	Other Names	Detected[a] (Y/N)	Multiple[b] (Y/N)	Configuration[c]	Class[d]	L_{bol} ($L_\odot$)	T_{bol} (K)
Per-emb-1	03:43:56.806	+32:00:50.202	HH211-MMS	Y	N	A,B	0	1.80 ± 0.10	27.0 ± 1.0
Per-emb-2	03:32:17.928	+30:49:47.825	IRAS 03292+3039	Y	Y	A,B	0	0.90 ± 0.07	27.0 ± 1.0
Per-emb-3	03:29:00.575	+31:12:00.204		Y	N	A,B	0	0.50 ± 0.06	32.0 ± 2.0
Per-emb-4	03:28:39.101	+31:06:01.800		N	N	B	0	0.22 ± 0.03	31.0 ± 3.0
Per-emb-5	03:31:20.939	+30:45:30.273	IRAS 03282+3035	Y	Y	A,B	0	1.30 ± 0.10	32.0 ± 2.0
Per-emb-6	03:33:14.404	+31:07:10.715		Y	N	A,B	0	0.30 ± 0.00	52.0 ± 3.0
Per-emb-7	03:30:32.681	+30:26:26.480		N	N	B	0	0.15 ± 0.06	37.0 ± 4.0
Per-emb-8	03:44:43.982	+32:01:35.210		Y	Y	A,B	0	2.60 ± 0.50	43.0 ± 6.0
Per-emb-9	03:29:51.832	+31:39:05.905	IRAS 03267+3128, Perseus5	Y	N	A,B	0	0.60 ± 0.06	36.0 ± 2.0
Per-emb-10	03:33:16.424	+31:06:52.063		Y	N	A,B	0	0.60 ± 0.05	30.0 ± 2.0
Per-emb-11	03:43:57.065	+32:03:04.788	IC348MMS	Y	Y	A,B	0	1.50 ± 0.10	30.0 ± 2.0
Per-emb-12	03:29:10.537	+31:13:30.933	NGC 1333 IRAS4A	Y	Y	A,B	0	7.00 ± 0.70	29.0 ± 2.0
Per-emb-13	03:29:12.016	+31:13:08.031	NGC 1333 IRAS4B	Y	Y	A,B	0	4.00 ± 0.30	28.0 ± 1.0
Per-emb-14	03:29:13.548	+31:13:58.150	NGC 1333 IRAS4C	Y	N	A,B	0	0.70 ± 0.08	31.0 ± 2.0
Per-emb-15	03:29:04.055	+31:14:46.237	RNO15-FIR	Y	N	A,B	0	0.40 ± 0.10	36.0 ± 4.0
Per-emb-16	03:43:50.978	+32:03:24.101		Y	Y	A,B	0	0.40 ± 0.04	39.0 ± 2.0
Per-emb-17	03:27:39.105	+30:13:03.068		Y	Y	A,B	0	4.20 ± 0.10	59.0 ± 11.0
Per-emb-18	03:29:11.258	+31:18:31.073	NGC 1333 IRAS7	Y	Y	A,B	0	2.80 ± 1.70	59.0 ± 12.0
Per-emb-19	03:29:23.498	+31:33:29.173		Y	N	A,B	0/I	0.36 ± 0.05	60.0 ± 3.0
Per-emb-20	03:27:43.276	+30:12:28.781	L1455-IRS4	Y	N	A,B	0/I	1.40 ± 0.20	65.0 ± 3.0
Per-emb-21	03:29:10.668	+31:18:20.191		Y	Y	A,B	0	6.90 ± 1.90	45.0 ± 12.0
Per-emb-22	03:25:22.409	+30:45:13.258	L1448-IRS2	Y	Y	A,B	0	3.60 ± 0.50	43.0 ± 2.0
Per-emb-23	03:29:17.211	+31:27:46.302	ASR 30	Y	N	A,B	0	0.80 ± 0.10	42.0 ± 2.0
Per-emb-24	03:28:45.297	+31:05:41.693		Y	N	A,B	0/I	0.43 ± 0.01	67.0 ± 10.0
Per-emb-25	03:26:37.511	+30:15:27.813		Y	N	A,B	0/I	1.20 ± 0.02	61.0 ± 12.0
Per-emb-26	03:25:38.875	+30:44:05.283	L1448C, L1448-mm	Y	Y	A,B	0	8.40 ± 1.50	47.0 ± 7.0
Per-emb-27	03:28:55.569	+31:14:37.025	NGC 1333 IRAS2A	Y	Y	A,B	0/I	19.00 ± 0.40	69.0 ± 1.0
Per-emb-28	03:43:51.008	+32:03:08.042		Y	Y	A,B	0	0.70 ± 0.08	45.0 ± 2.0
Per-emb-29	03:33:17.877	+31:09:31.817	B1-c	Y	N	A,B	0	3.70 ± 0.40	48.0 ± 1.0
Per-emb-30	03:33:27.303	+31:07:10.160		Y	N	A,B	0/I	1.70 ± 0.01	78.0 ± 6.0
Per-emb-31	03:28:32.547	+31:11:05.151		Y	N	A,B	0/I	0.16 ± 0.01	80.0 ± 13.0
Per-emb-32	03:44:02.403	+32:02:04.734		Y	Y	A,B	0	0.30 ± 0.10	57.0 ± 10.0
Per-emb-33	03:25:36.379	+30:45:14.728	L1448IRS3B, L1448N	Y	Y	A,B	0	8.30 ± 0.80	57.0 ± 3.0

Table 1—Continued

Source	RA (J2000)	Dec (J2000)	Other Names	Detected[a] (Y/N)	Multiple[b] (Y/N)	Configuration[c]	Class[d]	L_{bol} ($L_\odot$)	T_{bol} (K)
Per-emb-34	03:30:15.163	+30:23:49.233	IRAS 03271+3013	Y	N	A,B	I	1.60 ± 0.10	99.0 ± 13.0
Per-emb-35	03:28:37.090	+31:13:30.788	NGC 1333 IRAS1	Y	Y	A,B	I	9.10 ± 0.30	103.0 ± 26.0
Per-emb-36	03:28:57.374	+31:14:15.772	NGC 1333 IRAS2B	Y	Y	A,B	I	5.30 ± 1.00	106.0 ± 12.0
Per-emb-37	03:29:18.965	+31:23:14.304		Y	Y	A,B	0	0.50 ± 0.10	22.0 ± 1.0
Per-emb-38	03:32:29.197	+31:02:40.759		Y	N	A,B	I	0.54 ± 0.01	115.0 ± 21.0
Per-emb-39	03:33:13.781	+31:20:05.204		N	N	B	I	0.04 ± 0.08	125.0 ± 47.0
Per-emb-40	03:33:16.669	+31:07:54.901	B1-a	Y	Y	A,B	I	1.50 ± 1.00	132.0 ± 25.0
Per-emb-41	03:33:20.341	+31:07:21.355	B1-b	Y	Y	A,B	I	0.17 ± 0.36	157.0 ± 72.0
Per-emb-42	03:25:39.135	+30:43:57.909	L1448C-S	Y	Y	A,B	I	0.68 ± 0.85	163.0 ± 51.0
Per-emb-43	03:42:02.160	+31:48:02.081		N	N	B	I	0.07 ± 0.06	176.0 ± 42.0
Per-emb-44	03:29:03.764	+31:16:03.808	SVS13A	Y	Y	A,B	0/I	32.50 ± 7.10	188.0 ± 9.0
Per-emb-45	03:33:09.569	+31:05:31.193		N	N	B	I	0.05 ± 0.06	197.0 ± 93.0
Per-emb-46	03:28:00.415	+30:08:01.013		Y	N	A,B	I	0.30 ± 0.07	221.0 ± 7.0
Per-emb-47	03:28:34.507	+31:00:50.990	IRAS 03254+3050	Y	N	A,B	I	1.20 ± 0.10	230.0 ± 17.0
Per-emb-48	03:27:38.268	+30:13:58.448	L1455-FIR2	Y	Y	A,B	I	0.87 ± 0.04	238.0 ± 14.0
Per-emb-49	03:29:12.957	+31:18:14.307		Y	Y	A,B	I	1.10 ± 0.70	239.0 ± 68.0
Per-emb-50	03:29:07.768	+31:21:57.128		Y	N	A,B	I	23.20 ± 3.00	128.0 ± 23.0
Per-emb-51	03:28:34.536	+31:07:05.520		N	N	B	I	0.07 ± 0.10	263.0 ± 115.0
Per-emb-52	03:28:39.699	+31:17:31.882		Y	N	A,B	I	0.16 ± 0.21	278.0 ± 119.0
Per-emb-53	03:47:41.591	+32:51:43.672	B5-IRS1	Y	N	A,B	I	4.70 ± 0.90	287.0 ± 8.0
Per-emb-54	03:29:01.549	+31:20:20.497	NGC 1333 IRAS6	Y	N	A,B	I	16.80 ± 2.60	131.0 ± 63.0
Per-emb-55	03:44:43.298	+32:01:31.236	IRAS 03415+3152	Y	Y	A,B	I	1.80 ± 0.80	309.0 ± 64.0
Per-emb-56	03:47:05.450	+32:43:08.240	IRAS 03439+3233	Y	N	A,B	I	0.54 ± 0.09	312.0 ± 1.0
Per-emb-57	03:29:03.331	+31:23:14.573		Y	N	A,B	I	0.09 ± 0.45	313.0 ± 200.0
Per-emb-58	03:28:58.422	+31:22:17.481		Y	N	A,B	I	0.63 ± 0.47	322.0 ± 88.0
Per-emb-59	03:28:35.040	+30:20:09.884		N	N	B	I	0.04 ± 0.06	341.0 ± 179.0
Per-emb-60	03:29:20.068	+31:24:07.488		N	N	B	I	0.28 ± 1.05	363.0 ± 240.0
Per-emb-61	03:44:21.357	+31:59:32.514		Y	N	A,B	I	0.24 ± 0.16	371.0 ± 107.0
Per-emb-62	03:44:12.977	+32:01:35.419		Y	N	A,B	I	1.80 ± 0.40	378.0 ± 29.0
Per-emb-63	03:28:43.271	+31:17:32.931		Y	N	A,B	I	1.90 ± 0.40	436.0 ± 9.0
Per-emb-64	03:33:12.852	+31:21:24.020		Y	N	A,B	I	3.20 ± 0.60	438.0 ± 8.0
Per-emb-65	03:28:56.316	+31:22:27.798		Y	N	A,B	I	0.16 ± 0.16	440.0 ± 191.0
Per-emb-66	03:43:45.150	+32:03:58.608		Y	N	A,B	I	0.69 ± 0.22	542.0 ± 110.0

Table 1—Continued

Source	RA (J2000)	Dec (J2000)	Other Names	Detected[a] (Y/N)	Multiple[b] (Y/N)	Configuration[c]	Class[d]	L_{bol} ($L_\odot$)	T_{bol} (K)
Per-bolo-58	03:29:25.464	+31:28:14.880	Per-Bolo-58	N	N	B	0	0.05 ± 0.50	15.0 ± -99.0
Per-bolo-45	03:29:07.700	+31:17:16.800	Per-Bolo-45	N	N	B	0	0.05 ± 0.05	15.0 ± -99.0
L1451-MMS	03:25:10.245	+30:23:55.059	L1451-MMS	Y	N	A,B	0	0.05 ± 0.05	15.0 ± -99.0
L1448IRS2E	03:25:25.660	+30:44:56.695	L1448IRS2E	N	N	B	0	0.05 ± 0.05	15.0 ± -99.0
B1-bN	03:33:21.209	+31:07:43.665	B1-bN	Y	Y	A,B	0	0.32 ± 0.10	14.7 ± 1.0
B1-bS	03:33:21.355	+31:07:26.372	B1-bS	Y	Y	A,B	0	0.70 ± 0.07	17.7 ± 1.0
L1448IRS1	03:25:09.449	+30:46:21.933	L1448IRS1	Y	Y	A,B	I	-99.90 ± -99.90	-99.9 ± -99.9
L1448NW	03:25:35.671	+30:45:34.193	L1448IRS3C	Y	Y	A,B	0	1.40 ± 0.10	22.0 ± 1.0
L1448IRS3A	03:25:36.499	+30:45:21.880		Y	Y	A,B	I	9.20 ± 1.30	47.0 ± 2.0
SVS13C	03:29:01.970	+31:15:38.053	SVS13C	Y	Y	A,B	0	1.50 ± 0.20	21.0 ± 1.0
SVS13B	03:29:03.078	+31:15:51.740	SVS13B	Y	Y	A,B	0	1.00 ± 1.00	20.0 ± 20.0
IRAS 03363+3207	03:39:25.547	+32:17:07.089		Y	N	A,B	I?	-99.90 ± -99.90	-99.9 ± -99.9
EDJ2009-161	03:28:51.480	+30:45:00.360		N	N	B	II	1.10 ± 0.10	1200.0 ± -99.0
EDJ2009-263	03:30:27.161	+30:28:29.613		Y	N	A,B	Flat	0.23 ± 0.10	340.0 ± -99.0
EDJ2009-285	03:32:46.942	+30:59:17.797		N	N	B	II	0.47 ± 0.10	920.0 ± -99.0
IRAS 03295+3050	03:32:34.066	+31:00:55.621	EDJ2009-282	Y	N	A,B	II	0.25 ± 0.10	1300.0 ± -99.0
L1455IRS2	03:27:47.690	+30:12:04.314	EDJ2009-133	Y	N	A,B	Flat	2.50 ± 0.10	740.0 ± -99.0
EDJ2009-333	03:42:55.772	+31:58:44.386		N	N	B	II	1.30 ± 0.10	980.0 ± -99.0
EDJ2009-385	03:44:18.168	+32:04:56.907		Y	N	A,B	II	0.38 ± 0.10	1200.0 ± -99.0
EDJ2009-366	03:43:59.651	+32:01:54.008		Y	N	A,B	II	1.80 ± 0.10	620.0 ± -99.0
EDJ2009-269	03:30:44.014	+30:32:46.812		Y	Y	A,B	II	1.30 ± 0.10	1200.0 ± -99.0
EDJ2009-268	03:30:38.231	+30:32:11.666		N	N	A	Flat	0.04 ± 0.10	320.0 ± -99.0
EDJ2009-183	03:28:59.297	+31:15:48.410	ASR 106	Y	Y	A,B	Flat	3.20 ± 0.10	100.0 ± -99.0
EDJ2009-164	03:28:53.961	+31:18:09.349	ASR 40	N	N	A,B	II	0.14 ± 0.10	890.0 ± -99.0
EDJ2009-156	03:28:51.029	+31:18:18.409	ASR 122	Y	Y	A,B	II	0.04 ± 0.10	740.0 ± -99.0
EDJ2009-172	03:28:56.650	+31:18:35.449	ASR 120	Y	N	A,B	II	0.39 ± 0.10	1100.0 ± -99.0
IRAS4B'	03:29:12.842	+31:13:06.893	NGC 1333 IRAS4B'	Y	Y	A,B	0	0.10 ± 0.10	15.0 ± -99.0
RAC1999-VLA20	03:29:04.255	+31:16:09.138		Y	N	A,B	Extragalactic	-99.00 ± -99.00	-99.0 ± -99.0
EDJ2009-233	03:29:17.675	+31:22:44.922		Y	Y	A,B	II	1.40 ± 0.10	1300.0 ± -99.0
EDJ2009-235	03:29:18.259	+31:23:19.758		Y	Y	A,B	II	0.54 ± 0.10	-99.0 ± -99.0
SVS3	03:29:10.420	+31:21:59.072		Y	N	A,B	II	0.54 ± 0.10	-99.0 ± -99.0
EDJ2009-173	03:28:56.964	+31:16:22.199	ASR 118, SVS15	Y	N	A,B	II	0.10 ± 0.10	1100.0 ± -99.0
RAC97-VLA1	03:28:57.657	+31:15:31.450		Y	N	A,B	Extragalactic	-99.00 ± -99.00	-99.0 ± -99.0

Table 1—Continued

Source	RA (J2000)	Dec (J2000)	Other Names	Detected[a] (Y/N)	Multiple[b] (Y/N)	Configuration[c]	Class[d]	L_{bol} ($L_\odot$)	T_{bol} (K)

Note. — The sources denoted Per-emb-XX correspond to the sources published in Enoch et al. (2009), EDJ2009 sources are from Evans et al. (2009), ASR refers to Aspin et al. (1994), SVS refers to (Strom et al. 1976) and RAC1999-VLA20 is from Rodríguez et al. (1999). IRAS4B' was observed in the same field Per-emb-13, EDJ2009-233/235 were observed in the same field, and RAC1999-VLA20 was observed in the same field as Per-emb-44.

[a]Refers to whether or not the associated source was detected above 5σ in the observations (at either 8 mm or 1 cm).

[b]Denotes whether or not the object comprises a multiple system or is a component of a multiple system based on our data.

[c]VLA Configuration(s) in which observations were taken.

[d]Young Stellar Object Classification based on T_{bol} from Enoch et al. (2009), Sadavoy et al. (2014), and Young et al. (2015).

Table 2. Source Properties

Source	RA (J2000)	Dec (J2000)	$F_{\nu,int}$ (8 mm) (mJy)	$F_{\nu,peak}$ (8 mm) (mJy)	RMS (8 mm) (mJy)	$F_{\nu,int}$ (10 mm) (mJy)	$F_{\nu,peak}$ (10 mm) (mJy)	RMS (10 mm) (mJy)	Sp. Index (Int.)	Sp. Index (Peak)
Per-emb-1	03:43:56.806	+32:00:50.202	0.845 ± 0.022	0.673	0.010	0.567 ± 0.019	0.464	0.009	1.653 ± 0.031	1.54 ± 0.010
Per-emb-2										
Per-emb-2-comb	03:32:17.928	+30:49:47.825	2.482 ± 0.103	0.504	0.012	1.251 ± 0.068	0.355	0.010	2.843 ± 0.080	1.46 ± 0.025
Per-emb-2-A	03:32:17.932	+30:49:47.705	0.296 ± 0.040	0.210	0.017	0.185 ± 0.039	0.131	0.017	1.95 ± 5.663	1.97 ± 2.139
Per-emb-2-B	03:32:17.927	+30:49:47.753	0.137 ± 0.016	0.124	0.017	0.124 ± 0.014	0.133	0.017	0.42 ± 2.468	-0.28 ± 3.260
Per-emb-3	03:29:00.575	+31:12:00.204	0.402 ± 0.022	0.363	0.012	0.291 ± 0.020	0.250	0.010	1.337 ± 0.138	1.55 ± 0.047
Per-emb-4	03:28:39.101	+31:06:01.800	<0.035 ± 0.012	<0.035	0.012	<0.030 ± 0.010	<0.030	0.010	-99.9 ± -99.9	-99.9 ± -99.9
Per-emb-5										
Per-emb-5-comb	03:31:20.939	+30:45:30.273	1.357 ± 0.035	0.814	0.013	0.702 ± 0.026	0.482	0.011	2.739 ± 0.035	2.17 ± 0.013
Per-emb-5-A	03:31:20.942	+30:45:30.263	0.449 ± 0.030	0.162	0.013	0.211 ± 0.018	0.112	0.011	3.13 ± 1.101	1.55 ± 1.511
Per-emb-5-B	03:31:20.935	+30:45:30.247	0.177 ± 0.012	0.122	0.013	0.135 ± 0.010	0.117	0.011	1.12 ± 0.934	0.18 ± 1.857
Per-emb-6	03:33:14.404	+31:07:10.715	0.280 ± 0.023	0.270	0.012	0.211 ± 0.019	0.195	0.010	1.173 ± 0.259	1.35 ± 0.086
Per-emb-7	03:30:32.681	+30:26:26.480	<0.037 ± 0.013	<0.037	0.013	<0.032 ± 0.011	<0.032	0.011	-99.9 ± -99.9	-99.9 ± -99.9
Per-emb-8	03:44:43.982	+32:01:35.210	1.115 ± 0.029	0.835	0.013	0.739 ± 0.026	0.574	0.011	1.710 ± 0.033	1.56 ± 0.011
Per-emb-9	03:29:51.832	+31:39:05.905	0.078 ± 0.029	0.056	0.013	0.041 ± 0.017	0.051	0.011	2.677 ± 5.624	0.38 ± 1.700
Per-emb-10	03:33:16.424	+31:06:52.063	0.369 ± 0.023	0.356	0.012	0.265 ± 0.020	0.258	0.011	1.380 ± 0.159	1.33 ± 0.053
Per-emb-11										
Per-emb-11-A	03:43:57.065	+32:03:04.788	1.064 ± 0.032	0.717	0.013	0.583 ± 0.025	0.435	0.011	2.50 ± 0.255	2.07 ± 0.087
Per-emb-11-B	03:43:56.881	+32:03:02.977	0.097 ± 0.021	0.105	0.013	0.079 ± 0.023	0.072	0.011	0.85 ± 11.726	1.60 ± 3.494
Per-emb-11-C	03:43:57.688	+32:03:09.975	0.086 ± 0.028	0.073	0.013	0.040 ± 0.014	0.050	0.011	3.12 ± 21.052	1.62 ± 7.219
Per-emb-12										
Per-emb-12-A	03:29:10.537	+31:13:30.925	9.858 ± 0.123	1.810	0.019	5.025 ± 0.076	1.292	0.014	2.80 ± 0.035	1.40 ± 0.021
Per-emb-12-B	03:29:10.427	+31:13:32.099	0.805 ± 0.057	0.459	0.019	0.534 ± 0.034	0.386	0.014	1.70 ± 0.818	0.72 ± 0.281
Per-emb-13	03:29:12.016	+31:13:08.031	3.480 ± 0.057	1.300	0.013	1.830 ± 0.041	0.823	0.011	2.668 ± 0.013	1.90 ± 0.005
Per-emb-14	03:29:13.548	+31:13:58.150	0.865 ± 0.031	0.622	0.013	0.507 ± 0.025	0.402	0.012	2.222 ± 0.063	1.81 ± 0.023
Per-emb-15	03:29:04.055	+31:14:46.237	0.067 ± 0.025	0.059	0.012	0.070 ± 0.024	0.052	0.011	-0.220 ± 4.560	0.48 ± 1.486
Per-emb-16	03:43:50.978	+32:03:24.101	0.066 ± 0.026	0.048	0.012	0.069 ± 0.027	0.055	0.011	-0.200 ± 5.215	-0.50 ± 1.798
Per-emb-17										
Per-emb-17-A	03:27:39.104	+30:13:03.078	0.524 ± 0.019	0.468	0.010	0.364 ± 0.018	0.318	0.009	1.50 ± 0.340	1.60 ± 0.113
Per-emb-17-B	03:27:39.115	+30:13:02.840	0.105 ± 0.013	0.081	0.010	0.056 ± 0.007	0.055	0.009	2.56 ± 2.940	1.59 ± 3.755
Per-emb-18										
Per-emb-18-comb	03:29:11.258	+31:18:31.073	0.733 ± 0.035	0.458	0.012	0.573 ± 0.028	0.404	0.011	1.019 ± 0.079	0.52 ± 0.025

Table 2—Continued

Source	RA (J2000)	Dec (J2000)	$F_{\nu,int}$ (8 mm) (mJy)	$F_{\nu,peak}$ (8 mm) (mJy)	RMS (8 mm) (mJy)	$F_{\nu,int}$ (10 mm) (mJy)	$F_{\nu,peak}$ (10 mm) (mJy)	RMS (10 mm) (mJy)	Sp. Index (Int.)	Sp. Index (Peak)
Per-emb-18-A	03:29:11.255	+31:18:31.059	0.161 ± 0.035	0.175	0.021	0.191 ± 0.041	0.150	0.019	-0.73 ± 8.456	0.64 ± 2.762
Per-emb-18-B	03:29:11.261	+31:18:31.073	0.280 ± 0.054	0.169	0.021	0.161 ± 0.037	0.131	0.019	2.29 ± 8.141	1.07 ± 3.313
Per-emb-19	03:29:23.498	+31:33:29.173	0.260 ± 0.026	0.210	0.012	0.201 ± 0.022	0.179	0.011	1.064 ± 0.376	0.66 ± 0.122
Per-emb-20	03:27:43.276	+30:12:28.781	0.172 ± 0.023	0.165	0.013	0.187 ± 0.021	0.168	0.011	-0.345 ± 0.522	-0.09 ± 0.178
Per-emb-21	03:29:10.668	+31:18:20.191	0.555 ± 0.024	0.496	0.012	0.300 ± 0.020	0.292	0.011	2.553 ± 0.106	2.20 ± 0.035
Per-emb-22										
Per-emb-22-A	03:25:22.410	+30:45:13.254	0.532 ± 0.022	0.454	0.011	0.448 ± 0.020	0.377	0.010	0.72 ± 0.338	0.77 ± 0.115
Per-emb-22-B	03:25:22.352	+30:45:13.151	0.191 ± 0.024	0.151	0.011	0.136 ± 0.019	0.122	0.010	1.39 ± 3.115	0.90 ± 1.068
Per-emb-23	03:29:17.211	+31:27:46.302	0.157 ± 0.022	0.160	0.013	0.090 ± 0.016	0.104	0.011	2.311 ± 0.904	1.79 ± 0.312
Per-emb-24	03:28:45.297	+31:05:41.693	0.083 ± 0.014	0.079	0.010	0.052 ± 0.007	0.064	0.009	1.977 ± 0.830	0.90 ± 0.661
Per-emb-25	03:26:37.511	+30:15:27.813	0.749 ± 0.023	0.600	0.011	0.491 ± 0.019	0.413	0.009	1.750 ± 0.041	1.55 ± 0.014
Per-emb-26	03:25:38.875	+30:44:05.283	2.065 ± 0.024	1.813	0.012	1.294 ± 0.020	1.186	0.011	1.940 ± 0.006	1.76 ± 0.002
Per-emb-27										
Per-emb-27-A	03:28:55.569	+31:14:37.022	1.711 ± 0.019	1.510	0.010	1.135 ± 0.016	1.018	0.008	1.70 ± 0.029	1.63 ± 0.010
Per-emb-27-B	03:28:55.563	+31:14:36.408	0.324 ± 0.020	0.286	0.010	0.215 ± 0.015	0.209	0.008	1.70 ± 0.749	1.30 ± 0.248
Per-emb-28	03:43:51.008	+32:03:08.042	0.103 ± 0.037	0.058	0.013	0.053 ± 0.025	0.050	0.012	2.729 ± 5.967	0.66 ± 1.892
Per-emb-29	03:33:17.877	+31:09:31.817	0.565 ± 0.022	0.486	0.011	0.365 ± 0.019	0.314	0.009	1.819 ± 0.073	1.82 ± 0.024
Per-emb-30	03:33:27.303	+31:07:10.160	0.968 ± 0.022	0.817	0.011	0.701 ± 0.019	0.600	0.009	1.336 ± 0.022	1.28 ± 0.007
Per-emb-31	03:28:32.547	+31:11:05.151	0.049 ± 0.024	0.038	0.013	0.075 ± 0.023	0.054	0.012	-1.812 ± 5.933	-1.38 ± 2.718
Per-emb-32										
Per-emb-32-A	03:44:02.403	+32:02:04.751	0.055 ± 0.022	0.045	0.011	0.028 ± 0.011	0.035	0.008	2.85 ± 27.780	1.09 ± 9.967
Per-emb-32-B	03:44:02.633	+32:01:59.431	0.096 ± 0.033	0.052	0.011	0.029 ± 0.010	0.041	0.008	4.92 ± 22.100	0.98 ± 7.468
Per-emb-33										
Per-emb-33-A	03:25:36.380	+30:45:14.723	0.820 ± 0.034	0.453	0.011	0.484 ± 0.031	0.257	0.010	2.19 ± 0.539	2.35 ± 0.183
Per-emb-33-B	03:25:36.312	+30:45:15.154	0.424 ± 0.034	0.258	0.011	0.317 ± 0.030	0.181	0.010	1.20 ± 1.427	1.48 ± 0.427
Per-emb-33-C	03:25:36.321	+30:45:14.914	0.312 ± 0.028	0.212	0.011	0.247 ± 0.020	0.208	0.010	0.96 ± 1.320	0.09 ± 0.443
Per-emb-34	03:30:15.163	+30:23:49.233	0.225 ± 0.021	0.241	0.013	0.175 ± 0.019	0.184	0.012	1.039 ± 0.365	1.12 ± 0.119
Per-emb-35										
Per-emb-35-A	03:28:37.091	+31:13:30.788	0.430 ± 0.020	0.340	0.009	0.307 ± 0.017	0.258	0.009	1.40 ± 0.480	1.15 ± 0.168
Per-emb-35-B	03:28:37.219	+31:13:31.751	0.256 ± 0.018	0.231	0.009	0.201 ± 0.018	0.158	0.009	1.01 ± 1.200	1.58 ± 0.412
Per-emb-36										
Per-emb-36-A	03:28:57.374	+31:14:15.765	1.893 ± 0.026	1.545	0.013	1.190 ± 0.023	0.988	0.011	1.93 ± 0.053	1.86 ± 0.018

Table 2—Continued

Source	RA (J2000)	Dec (J2000)	$F_{\nu,int}$ (8 mm) (mJy)	$F_{\nu,peak}$ (8 mm) (mJy)	RMS (8 mm) (mJy)	$F_{\nu,int}$ (10 mm) (mJy)	$F_{\nu,peak}$ (10 mm) (mJy)	RMS (10 mm) (mJy)	Sp. Index (Int.)	Sp. Index (Peak)
Per-emb-36-B	03:28:57.370	+31:14:16.073	0.308 ± 0.021	0.226	0.013	0.180 ± 0.011	0.167	0.011	2.22 ± 0.767	1.26 ± 0.711
Per-emb-37	03:29:18.965	+31:23:14.304	0.256 ± 0.024	0.232	0.012	0.172 ± 0.021	0.167	0.012	1.645 ± 0.411	1.37 ± 0.136
Per-emb-38	03:32:29.197	+31:02:40.759	0.199 ± 0.028	0.154	0.013	0.127 ± 0.023	0.112	0.011	1.873 ± 0.926	1.32 ± 0.296
Per-emb-39	03:33:13.781	+31:20:05.204	<0.038 ± 0.013	<0.038	0.013	<0.030 ± 0.010	<0.030	0.010	-99.9 ± -99.9	-99.9 ± -99.9
Per-emb-40										
Per-emb-40-A	03:33:16.669	+31:07:54.902	0.417 ± 0.018	0.356	0.009	0.312 ± 0.014	0.280	0.007	1.21 ± 0.352	1.00 ± 0.118
Per-emb-40-B	03:33:16.680	+31:07:55.269	0.054 ± 0.019	0.042	0.009	0.062 ± 0.015	0.052	0.007	-0.56 ± 16.636	-0.86 ± 5.822
Per-emb-41	03:33:20.341	+31:07:21.355	0.101 ± 0.024	0.102	0.013	0.081 ± 0.025	0.057	0.011	0.929 ± 2.633	2.40 ± 0.982
Per-emb-42	03:25:39.135	+30:43:57.909	0.273 ± 0.024	0.245	0.012	0.182 ± 0.019	0.180	0.011	1.677 ± 0.321	1.28 ± 0.103
Per-emb-43	03:42:02.160	+31:48:02.081	<0.038 ± 0.013	<0.038	0.013	<0.030 ± 0.010	<0.030	0.010	-99.9 ± -99.9	-99.9 ± -99.9
Per-emb-44										
Per-emb-44-A	03:29:03.766	+31:16:03.810	1.763 ± 0.022	1.501	0.011	1.115 ± 0.019	0.988	0.010	1.90 ± 0.042	1.74 ± 0.015
Per-emb-44-B	03:29:03.743	+31:16:03.790	0.508 ± 0.034	0.320	0.011	0.375 ± 0.026	0.265	0.010	1.25 ± 0.841	0.78 ± 0.244
Per-emb-45	03:33:09.569	+31:05:31.193	<0.038 ± 0.013	<0.038	0.013	<0.030 ± 0.010	<0.030	0.010	-99.9 ± -99.9	-99.9 ± -99.9
Per-emb-46	03:28:00.415	+30:08:01.013	0.141 ± 0.042	0.089	0.015	0.118 ± 0.034	0.082	0.013	0.749 ± 2.925	0.31 ± 0.897
Per-emb-47	03:28:34.507	+31:00:50.990	0.304 ± 0.029	0.268	0.014	0.193 ± 0.022	0.177	0.012	1.874 ± 0.385	1.72 ± 0.124
Per-emb-48										
Per-emb-48-A	03:27:38.277	+30:13:58.559	0.085 ± 0.022	0.077	0.011	0.072 ± 0.024	0.053	0.010	0.66 ± 16.174	1.52 ± 5.375
Per-emb-48-B	03:27:38.258	+30:13:58.320	0.064 ± 0.023	0.052	0.011	0.072 ± 0.019	0.063	0.010	-0.51 ± 18.333	-0.79 ± 6.809
Per-emb-49										
Per-emb-49-A	03:29:12.953	+31:18:14.289	0.347 ± 0.020	0.286	0.010	0.305 ± 0.021	0.217	0.009	0.53 ± 0.730	1.14 ± 0.258
Per-emb-49-B	03:29:12.976	+31:18:14.397	0.095 ± 0.017	0.089	0.010	0.117 ± 0.015	0.113	0.009	-0.84 ± 4.512	-1.03 ± 1.685
Per-emb-50	03:29:07.768	+31:21:57.128	1.620 ± 0.031	1.274	0.014	1.063 ± 0.024	0.918	0.012	1.749 ± 0.015	1.36 ± 0.005
Per-emb-51	03:28:34.536	+31:07:05.520	<0.039 ± 0.013	<0.039	0.013	<0.035 ± 0.012	<0.035	0.012	-99.9 ± -99.9	-99.9 ± -99.9
Per-emb-52	03:28:39.699	+31:17:31.882	0.083 ± 0.020	0.090	0.013	0.067 ± 0.029	0.036	0.011	0.854 ± 4.118	3.81 ± 2.116
Per-emb-53	03:47:41.591	+32:51:43.672	0.241 ± 0.034	0.182	0.015	0.190 ± 0.027	0.146	0.012	0.976 ± 0.687	0.93 ± 0.219
Per-emb-54	03:29:01.549	+31:20:20.497	0.356 ± 0.031	0.292	0.015	0.294 ± 0.021	0.292	0.012	0.791 ± 0.214	0.01 ± 0.073
Per-emb-55										
Per-emb-55-A	03:44:43.298	+32:01:31.223	0.140 ± 0.012	0.114	0.010	0.058 ± 0.007	0.056	0.009	3.65 ± 2.066	2.96 ± 2.977
Per-emb-55-B	03:44:43.334	+32:01:31.636	0.078 ± 0.012	0.063	0.010	0.063 ± 0.007	0.060	0.009	0.90 ± 3.377	0.17 ± 4.241
Per-emb-56	03:47:05.450	+32:43:08.240	0.137 ± 0.023	0.134	0.014	0.054 ± 0.018	0.066	0.013	3.824 ± 2.297	2.91 ± 0.859
Per-emb-57	03:29:03.331	+31:23:14.573	0.176 ± 0.025	0.164	0.014	0.159 ± 0.032	0.119	0.013	0.429 ± 1.045	1.34 ± 0.335

Table 2—Continued

Source	RA (J2000)	Dec (J2000)	$F_{\nu,int}$ (8 mm) (mJy)	$F_{\nu,peak}$ (8 mm) (mJy)	RMS (8 mm) (mJy)	$F_{\nu,int}$ (10 mm) (mJy)	$F_{\nu,peak}$ (10 mm) (mJy)	RMS (10 mm) (mJy)	Sp. Index (Int.)	Sp. Index (Peak)
Per-emb-58	03:28:58.422	+31:22:17.481	0.071 ± 0.018	0.093	0.014	0.093 ± 0.037	0.055	0.013	-1.120 ± 3.830	2.16 ± 1.368
Per-emb-59	03:28:35.040	+30:20:09.884	<0.042 ± 0.014	<0.042	0.014	<0.037 ± 0.012	<0.037	0.012	-99.9 ± -99.9	-99.9 ± -99.9
Per-emb-60	03:29:20.068	+31:24:07.488	<0.041 ± 0.014	<0.041	0.014	<0.036 ± 0.012	<0.036	0.012	-99.9 ± -99.9	-99.9 ± -99.9
Per-emb-61	03:44:21.357	+31:59:32.514	0.116 ± 0.027	0.101	0.014	0.056 ± 0.024	0.051	0.012	2.997 ± 3.970	2.87 ± 1.297
Per-emb-62	03:44:12.977	+32:01:35.419	0.735 ± 0.029	0.616	0.015	0.488 ± 0.024	0.417	0.012	1.703 ± 0.070	1.62 ± 0.024
Per-emb-63	03:28:43.271	+31:17:32.931	0.378 ± 0.029	0.306	0.014	0.270 ± 0.020	0.264	0.011	1.387 ± 0.193	0.61 ± 0.069
Per-emb-64	03:33:12.852	+31:21:24.020	1.029 ± 0.029	0.891	0.015	0.810 ± 0.024	0.687	0.012	0.989 ± 0.029	1.08 ± 0.010
Per-emb-65	03:28:56.316	+31:22:27.798	0.141 ± 0.038	0.094	0.014	0.108 ± 0.032	0.070	0.013	1.105 ± 2.766	1.22 ± 0.963
Per-emb-66	03:43:45.150	+32:03:58.608	<0.041 ± 0.014	<0.041	0.014	<0.035 ± 0.012	<0.035	0.012	-99.9 ± -99.9	-99.9 ± -99.9
Per-bolo-58	03:29:25.464	+31:28:14.880	<0.037 ± 0.013	<0.037	0.013	<0.036 ± 0.012	<0.036	0.012	-99.9 ± -99.9	-99.9 ± -99.9
Per-bolo-45	03:29:07.700	+31:17:16.800	<0.037 ± 0.012	<0.037	0.012	<0.035 ± 0.012	<0.035	0.012	-99.9 ± -99.9	-99.9 ± -99.9
L1451-MMS	03:25:10.245	+30:23:55.059	0.285 ± 0.023	0.276	0.013	0.173 ± 0.019	0.170	0.011	2.078 ± 0.314	2.02 ± 0.106
L1448IRS2E	03:25:25.660	+30:44:56.695	<0.045 ± 0.015	<0.045	0.015	<0.040 ± 0.013	<0.040	0.013	-99.9 ± -99.9	-99.9 ± -99.9
B1-bN	03:33:21.209	+31:07:43.665	1.251 ± 0.036	0.756	0.013	0.680 ± 0.028	0.458	0.011	2.529 ± 0.044	2.08 ± 0.016
B1-bS	03:33:21.355	+31:07:26.372	0.906 ± 0.060	0.286	0.013	0.551 ± 0.048	0.188	0.011	2.058 ± 0.206	1.74 ± 0.101
L1448IRS1										
L1448IRS1-A	03:25:09.449	+30:46:21.924	0.871 ± 0.035	0.547	0.013	0.614 ± 0.031	0.398	0.012	1.45 ± 0.374	1.32 ± 0.131
L1448IRS1-B	03:25:09.413	+30:46:20.625	0.116 ± 0.022	0.080	0.013	0.063 ± 0.013	0.058	0.012	2.56 ± 7.440	1.33 ± 6.129
L1448NW										
L1448NW-A	03:25:35.669	+30:45:34.110	0.695 ± 0.022	0.609	0.012	0.486 ± 0.020	0.429	0.010	1.49 ± 0.243	1.45 ± 0.085
L1448NW-B	03:25:35.673	+30:45:34.357	0.475 ± 0.026	0.370	0.012	0.323 ± 0.023	0.254	0.010	1.61 ± 0.729	1.56 ± 0.237
L1448IRS3A	03:25:36.499	+30:45:21.880	1.067 ± 0.028	0.929	0.014	0.981 ± 0.026	0.829	0.013	0.345 ± 0.024	0.47 ± 0.008
SVS13C	03:29:01.970	+31:15:38.053	2.401 ± 0.031	1.717	0.013	2.134 ± 0.026	1.682	0.012	0.489 ± 0.005	0.09 ± 0.002
SVS13B	03:29:03.078	+31:15:51.740	1.555 ± 0.033	1.116	0.014	0.905 ± 0.027	0.723	0.013	2.245 ± 0.024	1.81 ± 0.008
IRAS 03363+3207	03:39:25.547	+32:17:07.089	0.898 ± 0.026	0.792	0.014	0.519 ± 0.020	0.507	0.011	2.278 ± 0.041	1.85 ± 0.014
EDJ2009-161	03:28:51.480	+30:45:00.360	<0.041 ± 0.014	<0.041	0.014	<0.035 ± 0.012	<0.035	0.012	-99.9 ± -99.9	-99.9 ± -99.9
EDJ2009-263	03:30:27.161	+30:28:29.613	0.088 ± 0.017	0.080	0.013	0.057 ± 0.009	0.062	0.012	1.835 ± 1.058	1.01 ± 1.095
EDJ2009-285	03:32:46.942	+30:59:17.797	<0.042 ± 0.014	<0.042	0.014	<0.039 ± 0.013	<0.039	0.013	-99.9 ± -99.9	-99.9 ± -99.9
IRAS 03295+3050	03:32:34.066	+31:00:55.621	0.146 ± 0.021	0.146	0.013	0.097 ± 0.020	0.095	0.011	1.717 ± 1.058	1.79 ± 0.385
L1455IRS2	03:27:47.690	+30:12:04.314	0.044 ± 0.013	0.067	0.013	0.088 ± 0.028	0.059	0.011	-2.907 ± 3.303	0.53 ± 1.299
EDJ2009-333	03:42:55.772	+31:58:44.386	<0.040 ± 0.013	<0.040	0.013	<0.034 ± 0.011	<0.034	0.011	-99.9 ± -99.9	-99.9 ± -99.9
EDJ2009-385	03:44:18.168	+32:04:56.907	0.247 ± 0.061	0.095	0.013	0.130 ± 0.028	0.077	0.011	2.647 ± 1.881	0.87 ± 0.677

Table 2—Continued

Source	RA (J2000)	Dec (J2000)	$F_{\nu,int}$ (8 mm) (mJy)	$F_{\nu,peak}$ (8 mm) (mJy)	RMS (8 mm) (mJy)	$F_{\nu,int}$ (10 mm) (mJy)	$F_{\nu,peak}$ (10 mm) (mJy)	RMS (10 mm) (mJy)	Sp. Index (Int.)	Sp. Index (Peak)
EDJ2009-366	03:43:59.651	+32:01:54.008	0.152 ± 0.021	0.162	0.013	0.137 ± 0.021	0.128	0.011	0.454 ± 0.742	0.96 ± 0.244
EDJ2009-269										
EDJ2009-269-A	03:30:44.014	+30:32:46.811	0.258 ± 0.035	0.163	0.013	0.224 ± 0.043	0.115	0.013	0.58 ± 5.130	1.46 ± 1.704
EDJ2009-269-B	03:30:43.978	+30:32:46.576	0.210 ± 0.039	0.127	0.013	0.121 ± 0.026	0.096	0.013	2.29 ± 7.484	1.15 ± 2.559
EDJ2009-268	03:30:38.231	+30:32:11.666	<0.040 ± 0.013	<0.040	0.013	<0.034 ± 0.011	<0.034	0.011	-99.9 ± -99.9	-99.9 ± -99.9
EDJ2009-183										
EDJ2009-183-A	03:28:59.296	+31:15:48.405	0.242 ± 0.048	0.099	0.011	0.122 ± 0.018	0.114	0.011	2.84 ± 5.665	-0.58 ± 2.012
EDJ2009-183-B	03:28:59.373	+31:15:48.399	0.047 ± 0.025	0.045	0.011	0.056 ± 0.023	0.037	0.011	-0.75 ± 40.680	0.86 ± 13.324
EDJ2009-164	03:28:53.961	+31:18:09.349	<0.055 ± 0.018	<0.055	0.018	<0.052 ± 0.017	<0.052	0.017	-99.9 ± -99.9	-99.9 ± -99.9
EDJ2009-156										
EDJ2009-156-A	03:28:51.031	+31:18:18.380	0.193 ± 0.032	0.139	0.014	0.107 ± 0.026	0.080	0.011	2.44 ± 7.858	2.32 ± 2.511
EDJ2009-156-B	03:28:51.111	+31:18:15.448	0.130 ± 0.026	0.107	0.014	0.079 ± 0.024	0.075	0.011	2.07 ± 11.924	1.48 ± 3.341
EDJ2009-172	03:28:56.650	+31:18:35.449	0.329 ± 0.028	0.224	0.010	0.277 ± 0.027	0.173	0.009	0.716 ± 0.293	1.07 ± 0.077
SVS13A2	03:29:03.386	+31:16:01.622	0.336 ± 0.027	0.317	0.014	0.270 ± 0.023	0.263	0.013	0.905 ± 0.239	0.78 ± 0.076
IRAS4B'	03:29:12.842	+31:13:06.893	1.556 ± 0.060	0.536	0.013	0.813 ± 0.044	0.319	0.011	2.697 ± 0.077	2.15 ± 0.030
BD +30 547	03:28:57.222	+31:14:18.991	0.075 ± 0.027	0.064	0.014	0.103 ± 0.029	0.073	0.012	-1.328 ± 3.539	-0.56 ± 1.283
RAC1999-VLA20	03:29:04.255	+31:16:09.138	0.161 ± 0.039	0.100	0.014	0.168 ± 0.037	0.109	0.013	-0.171 ± 1.874	-0.35 ± 0.592
EDJ2009-233	03:29:17.675	+31:22:44.922	0.454 ± 0.027	0.348	0.012	0.375 ± 0.027	0.281	0.012	0.785 ± 0.148	0.89 ± 0.052
EDJ2009-235	03:29:18.259	+31:23:19.758	0.040 ± 0.012	0.069	0.012	0.080 ± 0.030	0.061	0.012	-2.820 ± 3.906	0.52 ± 1.218
SVS3	03:29:10.420	+31:21:59.072	0.210 ± 0.029	0.177	0.014	0.270 ± 0.041	0.130	0.012	-1.047 ± 0.725	1.27 ± 0.257
EDJ2009-173	03:28:56.964	+31:16:22.199	0.232 ± 0.018	0.254	0.014	0.176 ± 0.009	0.176	0.012	1.147 ± 0.153	1.53 ± 0.132
RAC97-VLA1	03:28:57.657	+31:15:31.450	0.122 ± 0.031	0.098	0.014	0.155 ± 0.020	0.158	0.012	-1.011 ± 1.425	-1.98 ± 0.438

Table 3. Class 0 Multiple Systems

Source	Separation (″)	Separation (AU)	Flux Difference (Log [F_1/F_2])	Type
Per-emb-2	0.080 ± 0.006	18.4 ± 1.3	0.17 ± 0.15	Class 0
Per-emb-18	0.085 ± 0.004	19.6 ± 0.9	-0.02 ± 0.12	Class 0
Per-emb-5	0.097 ± 0.006	22.3 ± 1.4	0.26 ± 0.07	Class 0
L1448NW	0.251 ± 0.004	57.7 ± 1.0	0.17 ± 0.03	Class 0
Per-emb-17	0.278 ± 0.014	63.9 ± 3.1	0.75 ± 0.08	Class 0
Per-emb-44	0.300 ± 0.003	69.0 ± 0.7	0.48 ± 0.02	Class 0
Per-emb-27	0.620 ± 0.003	142.6 ± 0.7	0.75 ± 0.03	Class 0
Per-emb-22	0.751 ± 0.004	172.8 ± 1.0	0.51 ± 0.05	Class 0
Per-emb-33	0.795 ± 0.004	182.8 ± 1.0	0.33 ± 0.04	Class 0
Per-emb-33	0.974 ± 0.006	224.1 ± 1.3	0.25 ± 0.04	Class 0
Per-emb-12	1.830 ± 0.002	420.8 ± 0.4	1.04 ± 0.02	Class 0
Per-emb-11	2.951 ± 0.008	678.8 ± 1.7	0.93 ± 0.08	Class 0
Per-emb-44+SVS13A2	5.314 ± 0.004	1222.2 ± 0.9	1.78 ± 0.03	Class 0/I
Per-emb-32	6.066 ± 0.022	1395.3 ± 5.0	-0.16 ± 0.27	Class 0/I
Per-emb-33+L1448IRS3A	7.317 ± 0.004	1683.0 ± 0.9	-0.24 ± 0.02	Class 0-Class I
Per-emb-26+Per-emb-42	8.104 ± 0.005	1864.0 ± 1.2	1.97 ± 0.03	Class 0-Class I
Per-emb-11	9.469 ± 0.025	2177.8 ± 5.8	0.76 ± 0.13	Class 0
Per-emb-8+Per-emb-55	9.557 ± 0.013	2198.2 ± 2.9	2.38 ± 0.10	Class 0-Class I
Per-emb-37+EDJ2009+235	10.556 ± 0.009	2427.8 ± 2.2	1.53 ± 0.11	Class 0-Class II
Per-emb-13+IRAS4B'	10.654 ± 0.005	2450.4 ± 1.2	0.81 ± 0.02	Class 0-Class 0
Per-emb-21+Per-emb-18	13.252 ± 0.004	3048.0 ± 1.0	-0.44 ± 0.02	Class 0-Class 0
B1-bS+Per-emb-41	13.957 ± 0.014	3210.1 ± 3.2	2.08 ± 0.09	Class 0-Class 0/I
Per-emb-44+SVS13B	14.932 ± 0.002	3434.4 ± 0.5	0.40 ± 0.01	Class 0/I-Class 0
Per-emb-16+Per-emb-28	16.063 ± 0.037	3694.5 ± 8.5	-0.05 ± 0.17	Class 0-Class 0
B1-bN+B1-bS	17.395 ± 0.009	4000.8 ± 2.0	0.31 ± 0.03	Class 0-Class 0
Per-emb-33+L1448NW	21.503 ± 0.004	4945.6 ± 1.0	-0.23 ± 0.02	Class 0-Class 0
Per-emb-18+Per-emb-49	27.474 ± 0.007	6319.1 ± 1.5	0.33 ± 0.03	Class 0-Class I
Per-emb-12+Per-emb-13	29.739 ± 0.002	6840.0 ± 0.5	1.04 ± 0.01	Class 0-Class 0
Per-emb-36+Per-emb-27	31.420 ± 0.001	7226.6 ± 0.3	0.15 ± 0.01	Class 0-Class I
Per-emb-6+Per-emb-10	31.947 ± 0.005	7347.9 ± 1.2	-0.28 ± 0.03	Class 0-Class 0
Per-emb-37+EDJ2009+233	33.704 ± 0.006	7752.0 ± 1.3	-0.62 ± 0.04	Class 0-Class II
Per-emb-44+SVS13C	34.528 ± 0.001	7941.5 ± 0.3	-0.21 ± 0.01	Class 0/I-Class 0
Per-emb-32+EDJ2009+366	36.605 ± 0.010	8419.2 ± 2.4	-1.31 ± 0.11	Class 0/I-Class II

Note. — This table includes Class 0 + Class 0, Class 0 + Class I, and Class 0 + Class II multiple systems. The flux difference is calculated in the 9 mm band.

Table 4. Class I Multiple Systems

Source	Separation (″)	Separation (AU)	Flux Differencepe (Log [F_1/F_2])
Per-emb-36	0.311 ± 0.005	71.6 ± 1.2	0.80 ± 0.02
Per-emb-49	0.313 ± 0.009	71.9 ± 2.0	0.46 ± 0.11
Per-emb-48	0.346 ± 0.019	79.5 ± 4.4	0.06 ± 0.17
Per-emb-40	0.391 ± 0.022	90.0 ± 5.1	0.94 ± 0.19
Per-emb-55	0.618 ± 0.009	142.1 ± 2.0	0.14 ± 0.07
EDJ2009-183	1.025 ± 0.028	235.8 ± 6.4	0.45 ± 0.13
L1448IRS1	1.424 ± 0.015	327.4 ± 3.5	1.02 ± 0.09
Per-emb-35	1.908 ± 0.003	438.8 ± 0.7	0.23 ± 0.04
EDJ2009-156	3.107 ± 0.011	714.6 ± 2.5	0.17 ± 0.13
Per-emb-58+Per-emb-65	28.878 ± 0.023	6641.9 ± 5.3	-0.44 ± 0.13

Note. — This table includes only Class I + Class I multiple systems. The flux difference is calculated in the 9 mm band.

Table 5. Class II Multiple Systems

Source	Separation (″)	Separation (AU)	Flux Difference (Log [F_1/F_2])
EDJ2009-269	0.524 ± 0.007	120.6 ± 1.6	0.12 ± 0.08
EDJ2009-156	3.107 ± 0.011	714.6 ± 2.5	0.17 ± 0.13

Note. — This table includes only Class II + Class II multiple systems. The flux difference is calculated in the 9 mm band.

Table 6. Multiplicity and Companion Star Fractions

Sample/Sub-sample	Separation Range	S:B:T:Q:5:6	MF	CSF
Full Sample	15 - 10000 AU	37:15:5:2:2:1	0.40 ± 0.06	0.71 ± 0.06
Class 0	15 - 10000 AU	13:7:5:2:2:1	0.57 ± 0.09	1.2 ± 0.20
Class I	15 - 10000 AU	20:6:0:0:0:0	0.23 ± 0.08	0.23 ± 0.08
Class II	15 - 10000 AU	4:2:0:0:0:0	0.33 ± 0.19	0.33 ± 0.19
Full Sample	15 - 5000 AU	42:19:5:1:1:1	0.39 ± 0.06	0.59 ± 0.06
Class 0	15 - 5000 AU	15:10:5:1:1:1	0.55 ± 0.09	0.97 ± 0.03
Class I	15 - 5000 AU	22:7:0:0:0:0	0.24 ± 0.08	0.24 ± 0.08
Class II	15 - 5000 AU	5:2:0:0:0:0	0.29 ± 0.17	0.29 ± 0.17
Full Sample	50 - 5000 AU	45:16:5:1:1:1	0.35 ± 0.06	0.55 ± 0.06
Class 0	50 - 5000 AU	18:7:5:1:1:1	0.45 ± 0.09	0.88 ± 0.06
Class I	50 - 5000 AU	22:7:0:0:0:0	0.24 ± 0.08	0.24 ± 0.08
Class II	50 - 5000 AU	5:2:0:0:0:0	0.29 ± 0.17	0.29 ± 0.17
Full Sample	15 - 2000 AU	51:21:1:1:0:0	0.31 ± 0.05	0.35 ± 0.06
Class 0	15 - 2000 AU	24:11:1:1:0:0	0.35 ± 0.08	0.43 ± 0.08
Class I	15 - 2000 AU	21:8:0:0:0:0	0.28 ± 0.08	0.28 ± 0.08
Class II	15 - 2000 AU	6:2:0:0:0:0	0.25 ± 0.15	0.25 ± 0.15
Full Sample	50 - 2000 AU	54:18:1:1:0:0	0.27 ± 0.05	0.31 ± 0.05
Class 0	50 - 2000 AU	27:8:1:1:0:0	0.27 ± 0.07	0.35 ± 0.08
Class I	50 - 2000 AU	21:8:0:0:0:0	0.28 ± 0.08	0.28 ± 0.08
Class II	50 - 2000 AU	6:2:0:0:0:0	0.25 ± 0.15	0.25 ± 0.15
Full Sample	15 - 1000 AU	57:20:1:0:0:0	0.27 ± 0.05	0.28 ± 0.05
Class 0	15 - 1000 AU	29:10:1:0:0:0	0.28 ± 0.07	0.30 ± 0.07
Class I	15 - 1000 AU	22:8:0:0:0:0	0.27 ± 0.08	0.27 ± 0.08
Class II	15 - 1000 AU	6:2:0:0:0:0	0.25 ± 0.15	0.25 ± 0.15
Full Sample	50 - 1000 AU	60:17:1:0:0:0	0.23 ± 0.05	0.24 ± 0.05
Class 0	50 - 1000 AU	32:7:1:0:0:0	0.20 ± 0.06	0.22 ± 0.07
Class I	50 - 1000 AU	22:8:0:0:0:0	0.27 ± 0.08	0.27 ± 0.08
Class II	50 - 1000 AU	6:2:0:0:0:0	0.25 ± 0.15	0.25 ± 0.15
Full Sample	100 - 1000 AU	67:12:0:0:0:0	0.15 ± 0.04	0.15 ± 0.04
Class 0	100 - 1000 AU	36:5:0:0:0:0	0.12 ± 0.05	0.12 ± 0.05
Class I	100 - 1000 AU	25:5:0:0:0:0	0.17 ± 0.07	0.17 ± 0.07
Class II	100 - 1000 AU	6:2:0:0:0:0	0.25 ± 0.15	0.25 ± 0.15

Note. — Note that the uncertainties throughout the text are caculated assuming binomial statistics, $\sigma_{CSF} = (N_{comp}(1\text{-}N_{comp}/N_{sys})^{-0.5} \times 1/N_{sys}$ where N_{comp} is the number of companions and N_{sys} is the number of systems. σ_{MF} is calculated similarly, but by substituting N_{mult} (number of multiple systems) for N_{comp}. Poisson statistics are not used because the criteria of $N_{comp} >> N_{sys}$ is not met. However, we note that the variance calculated assuming binomial statistics is only slightly smaller than that of Poisson statistics.

For the case of CSF > 1.0, σ_{CSF} is not a real number and we revert to Poisson statistics in this case.

Table 7. Position Angles of Outflows and Close Multiples

Source	Outflow PA (°)	Companion PA (°)	Relative PA (°)	References
Per2	127	302.8	4.2	1
Per33	285	292.1	7.1	2, 3
Per27	24	187.6	16.4	4
Per36	24	352.2	31.8	4
Per44	130	266.1	43.9	4
Per5	125	256.1	48.9	5
Per35	290	59.7	50.3	5
Per22	318	262.1	55.9	3
Per107	308	10.5	62.5	3, 5
Per12	200	309.9	70.1	4
Per17	250	148.2	78.2	5
Per40	280	20.2	79.8	5
Per18	345	82.3	82.7	6

Note. — Only sources with known outflows and separations less than 500 AU are included. Outflow position angles (PA) taken from (1) Schnee et al. (2012), (2) Kwon et al. (2006), (3) Tobin et al. (2015b), (4) Plunkett et al. (2013), (5) Lee et al. (2015), (6) Davis et al. (2008). The relative PA column, is the absolute value of the companion position angle relative to the outflow position angle; as defined this angle will not be larger than 90°.